DESIGN OF ACTIVE FLOW CONTROL DEVICE INTEGRATION

INTO A COMPOSITE FLAP STRUCTURE

A Thesis
Presented to
The Academic Faculty

by

Jason Li

In Partial Fulfillment
of the Requirements for the Degree
Master of Science in the
School of Mechanical Engineering

Georgia Institute of Technology
August 2016

DESIGN OF ACTIVE FLOW CONTROL DEVICE INTEGRATION

INTO A COMPOSITE FLAP STRUCTURE

Approved by:

Dr. Jonathan Colton, Advisor
School of Mechanical Engineering
Georgia Institute of Technology

Dr. Ari Glezer
School of Mechanical Engineering
Georgia Institute of Technology

Dr. Kyriaki Kalaitzidou
School of Mechanical Engineering
Georgia Institute of Technology

Date Approved: April 29, 2016

ACKNOWLEDGMENTS

I would like to gratefully acknowledge those who have helped me throughout this project, without whom this project would not have been possible, in no particular order.

First, I would like to thank the GT-Boeing Strategic University Partnership Program for funding this project. Next, I would like to thank the immense amount of support received from individuals from Georgia Institute of Technology (Georgia Tech) and from The Boeing Company (Boeing). Prof. Jonathan Colton (Georgia Tech) first gave me the opportunity to assist in this research project and has been instrumental in guiding the direction of this project ever since. Additionally, he has helped me cultivate a stronger manufacturing and design engineer mindset. Pete George (Boeing) and Dr. Abe Gissen (Boeing) are to thank as well for their valuable feedback regarding experiments and design solutions.

I thank Prof. Ari Glezer, Dr. Bojan Vukasonovic and Dr. Michael DeSalvo from Georgia Tech for continued support throughout the project with regards to the fluidic oscillator design and testing. In particular, many thanks to Dr. DeSalvo for dedicating time to perform all fluidic oscillator testing and data collection and for remaining available at a moment's notice to discuss results and other fluidic oscillator related topics. Members from my research group, including Dr. Chris Yang, Ahmed Aly, Viyat Jhaveri, Jimmy Peterson III, and Sara Ha, are to thank for getting this project off the ground, for fluidic insert manufacturing, and for aiding in design decision discussions.

Next, I would like to thank members of the Georgia Tech machine shop, Steven Sheffield, Louis Boulanger, Nathan Mauldin, Brandon Royal, and Ben Coffman for

accurately manufacturing critical test pieces. Thanks to Chris White (Georgia Tech), I was able to access equipment to characterize the manufactured inserts. Additionally, many thanks to Rick Booth from Advanced Laser Materials and Brian Mueller and Dave Roedersheimer from RTP Company for their input regarding material properties.

Finally, I would like to thank all family members and friends who made this journey possible and bearable. Words of advice and encouragement were extremely helpful during this time. Above all, I thank my Father for His steadfast love and guidance.

TABLE OF CONTENTS

LIST OF TABLES

LIST OF FIGURES

LIST OF SYMBOLS

a_c	Critical half-crack length
A_p	Projected part area
AR	Aspect Ratio
[A]	Design Matrix relating FR and DP
B	Nozzle orifice width
b_{snap}	Beam width of snap-fit
[B]	Design Matrix relating DP and PV
$C_{ind,asm}$	Indirect costs for assembly
$C_{ind,mold\ mfg}$	Indirect costs for mold manufacturing
$C_{ind,part\ mfg}$	Indirect costs for part manufacturing
C_{asm}	Assembly cost
C_{base}	Mold base cost
C_{IM}	Cost to injection mold
C_{Lift}	Coefficient of lift
C_{SLS}	Cost to SLS
D	Part Depth
d	Bolt size/ diameter
D_b	Bolt Circle Diameter
E	Nozzle depth
E_{bend}	Flexural modulus
$E_{elastic}$	Elastic Modulus
E_{ma}	Efficiency Index
F_g	G-Force

F_L	Lift force
f_p	Parting surface factor
h_{max}	Maximum wall thickness
I_i	Information content
I_{snap}	Area moment of inertia
I_{sys}	Total Information Content of system
K_{IC}	Fracture Toughness
L	Part Length
L_1, L_2, L_3	Length on snap-fit
L_s	Maximum clamp stroke
M_e	Additional manufacturing hours for the ejector pins/system
M_{po}	Additional manufacturing hours due to the part size
M_s	Additional manufacturing hours for a non-flat parting surface
M_x	Additional manufacturing hours due to geometrical complexity of the part
N	Number of bolts
N_{isp}	Number of Inner Surface Patches
n_{items}	Number of items of a particular part
N_{min}	Theoretical Minimum Number of Parts
N_{osp}	Number of Outer Surface Patches
n_p	Number of parts per build for SLS
n_{pd}	Number of parts and additional components per design
n_{pm}	Number of parts manufactured for injection molding
P_i	Probability of satisfying FR
P_j	Injection power

T_x	Polymer ejection temperature
V_B	Volume of individual part
V_{bed}	SLS machine maximum build envelope
V_{ext}	Bounding box of individual part
V_s	Required shot size
v_{TAS}	True air speed
W	Part Width
W_{snap}	Mating force
X_i	Inner complexity of the part
X_o	Outer complexity of the part
Y_{snap}	Maximum deflection required
α	Angle at entrance side of snap-fit
$\alpha_{thermal}$	Thermal diffusivity coefficient
ϵ_0	Maximum allowable strain
$\theta_{jet\ difference}$	Jet spread half angle difference
$\theta_{jet\ left}$	Left jet spread half angle
$\theta_{jet\ right}$	Right jet spread half angle
μ	Coefficient of friction
ρ_{air}	Density of air
σ_w	Local normal stress in wall

LIST OF ABBREVIATIONS

AD	Axiomatic Design
AFC	Active Flow Control
AIBF	Advanced Internally Blown Flap
AR	Aspect Ratio
BDC	Best Design Concept
Boeing	The Boeing Company
C	Constraint
CA	Customer Attributes
CAD	Computer-Aided Design
CCW	Circulation Control Wing
CF	Carbon Fiber
CFRP	Carbon Fiber Reinforced Polymer
DFMA	Design for Manufacturing and Assembly
DP	Design Parameter
EBF	Externally Blown Flap
EPDM	Ethylene propylene diene monomer
FDM	Fused Deposition Molding
FEA	Finite Element Analysis
FMRL	Fluid Mechanics Research Laboratory
FOD	Foreign Object Debris
FR	Functional Requirement
FST	Fire, Smoke and Toxicity

Georgia Tech	Georgia Institute of Technology
IBF	Internally Blown Flap
IM	Injection Molding
LE	Leading Edge
MRL	Manufacturing Readiness Level
NOTAR	No Tail Rotar
NPE	Nozzle Profile Extension
PEEK	Polyetheretherketone
PEKK	Polyetherketoneketone
PFC	Passive Flow Control
PV	Process Variable
Resin	RenShape® SL
RTV	Room Temperature Vulcanized Silicone
SJA	Synthetic Jet Actuator
SLA	Stereolithography
SLS	Selective Laser Sintering
TE	Trailing Edge
TRL	Technology Readiness Level
UAV	Uninhabited Air Vehicle
USB	Upper Surface Blowing
UTS	Ultimate Tensile Strength
UV	Ultraviolet
V/STOL	Vertical and/or Short Take-Off and Landing

SUMMARY

Integration of active flow control technology into civil transport aircraft is a highly desired objective due to the potential part count, weight, and recurring manufacturing cost reductions. These benefits also have other ramifications, such as drag and emission reduction. However, the costs and the manufacturability of integrating active flow control devices, specifically fluidic oscillators, into a civil transport aircraft are not known. Additionally, the effects of different manufacturing techniques on fluidic oscillator performance are not known, specifically with regard to fused deposition molding (FDM) and selective laser sintering (SLS) manufacturing methods.

In this thesis, fluidic oscillators fabricated by FDM and SLS are compared to devices manufactured using injection molding, machining, and stereolithography. Manufactured devices are characterized through surface roughness and geometric dimensions (including the aspect ratio) and tolerances; oscillator performances are characterized by oscillation frequencies and velocity profiles. Analyzing velocity profile symmetry with respect to manufacturing characteristics, slight correlations are determined. Furthermore, the nozzle wall thickness and the air flow rate were determined to affect velocity profiles. However, all tested devices ultimately produced successful oscillation frequencies and a velocity profile with two local velocity peaks.

Following experimental tests, a best design concept (BDC) of a fluidic oscillator integrated into the leading edge of a trailing edge composite flap structure on a civil transport aircraft is attained through checking against design specifications, utilizing experimental results, applying design methodologies, and simulating expected loading conditions. Moreover, three BDC designs are visualized, each representing different manufacturing and assembly methods. Manufacturing and assembly procedures at the macro- and micro-scales are described. Finally, cost analyses of manufacturing,

assembly, material, and weight costs per part and per aircraft, are conducted for the three BDC designs to estimate the total costs of the integration solution, which ranges from about $4090 per aircraft for low production volumes to about $2600 per aircraft for high production volumes. As a result, the research conducted in this thesis provides a basis for the design of manufacturing and assembly techniques to integrate active flow control technology into civil transport aircraft.

CHAPTER 1

INTRODUCTION

A widely cited study was conducted by McLean et al. (1999) on the potential benefits of applying unsteady active flow control (AFC) to civil transport aircraft at multiple locations. They concluded that a high-lift wing system would have one of the greatest and most efficient impacts and be one of the most feasible locations for unsteady AFC devices. Using a Boeing 737-700 airplane as the reference, they determined that successful applications of unsteady active flow control (via compressed air or piezo-electrically actuated devices) in both leading edge (LE) devices (e.g., drooped LE) and trailing edge (TE) devices (e.g., Fowler flap) have potential reductions of roughly 2.6% in part count, 3.3% in empty weight, and 1.3% in recurring manufacturing cost. This can translate to potentially a 1.9% reduction in cruise drag (from the reduced weight) and the elimination of flap-track fairings that could further reduce cruise drag by 1.3%. Additionally, a 1.3% reduction in recurring manufacturing costs means that, for a $30 M aircraft, a simplified flap system could save approximately $400 K. The integration of unsteady AFC would not only help significantly increase the cost efficiencies of aircraft but would also help reduce aviation emission, improving the state of health and climate around the globe.

While worst-case cost estimates of the AFC system are made by McLean et al. (1999), these costs are excluded from the percentage reductions above due to large technical uncertainties in both the penalties and the potential benefits of such a system (McLean et al. 1999). Extensive research, including the most recent work on the Boeing 757 ecoDemonstrator (Lin et al. 2016) and the collaborations between The Boeing Company (Boeing) and Georgia Institute of Technology (Georgia Tech) (DeSalvo et al. 2011, DeSalvo et al. 2014, Kuchan 2012), have since quantified various aerodynamic

benefits of and examined the feasibility of AFC systems integrated into scaled and full

scale airfoils. Indeed, through joint efforts of multiple research groups, the technology

readiness level (TRL) (Figure 1.1.a) of unsteady fluidic oscillators used in aircraft is at

around a 5 or 6 (Lin et al. 2016). However, not much progress has been made with

regards to determining the manufacturability of or cost of a detailed integration solution,

evident in the estimated manufacturing readiness level (MRL) (Figure 1.1.b) of 4 or 5[1].

Therefore, to reduce the level of uncertainty in the penalties of a full-scale AFC system,

this project, as part of the Boeing Strategic University Partnership Program, sets forth

two objectives.

---

[1] Private Communications with Boeing

a)

b)

Figure 1.1. a) TRLs (Blank 2013) and b) MRLs (Alcorta 2014)

The primary objective of this work is to increase the MRL via a study on the design of integrating feedback-free fluidic oscillators into the nonstructural LE component of a composite TE flap structure on a civil transport aircraft. The best design concept (BDC) should account for design specifications, design methodologies, and expected loads such that the AFC system can transition from the testing phase to the production phase. To compare different designs, manufacturing and assembly process,

material, and weight costs should be analyzed, which will also contribute to defining a portion of the penalties associated with integrating a full-scale AFC system.

The secondary objective is to explore any effects different manufacturing processes might have on fluidic oscillators (a type of unsteady AFC device), which should inform decisions for the primary objective. Specifically, different manufacturing processes can result in different tolerances and surface roughness, which may impede or enhance the performance of the fluidic oscillator. Thus, the secondary objective is addressed before the primary objective in order to propagate beneficial and/or detrimental information through to the BDC. To achieve the secondary objective, an experiment is designed to quantify the manufacturing characteristics of differently manufactured fluidic oscillators and to compare the resulting air flow performances.

In this work, Chapter 2 discusses relevant background information regarding AFC devices in terms of what they are, how they have been integrated, and how they can be manufactured and assembled. Next, experimental design, methodology, and results and discussion are covered in Chapter 3 to examine manufacturing effect(s) on fluidic oscillators. Chapters 4 and 5 address the design methodologies used and explain the reasoning and tradeoffs for different design options that result in the final BDC. Additionally, Chapter 5 discusses BDC design variations, which are then used to delineate necessary manufacturing and assembly procedures and to provide the basis for determining manufacturing, assembly, material, and weight costs in Chapter 6. Required 3D model and cost model changes are discussed in the case an alternate actuator design is used. Finally, concluding remarks are presented in Chapter 7.

CHAPTER 2

ACTIVE FLOW CONTROL BACKGROUND

Active flow control (AFC) technology serves to postpone or control separation of a boundary layer from the bounding surface via energy expenditure. To understand the scope of the challenges in integrating AFC devices into an airfoil, AFC technology, integration advancement, and fluidic device production will be discussed. It is assumed that the reader has a basic grasp of aerodynamic concepts, such as lift and drag, and aircraft terminology, such as flap and leading edge.

2.1 Flow Control Technology Review

The field of flow control has a long history that began when Prandtl introduced the boundary layer theory in 1904 (Gad-el-Hak et al. 1998). During this time, he explained the physics of separation phenomena and described several experiments that controlled the boundary layer. Through many scientific advancements that followed, the field of flow control has made large strides towards characterizing fluid flow and how it can be altered. This field can be divided into two categories: AFC and passive flow control (PFC). Active flow control, as defined by Gad-el-Hak, is the manipulation of a fluid flow via energy expenditure to achieve "transition delay, separation postponement, lift increase, skin-friction and pressure drag reduction, turbulence augmentation, heat transfer enhancement, or noise suppression." Henceforth, the usage of the terms "AFC technology" or "AFC device" will refer to any apparatus that utilizes active flow control defined as manipulation of fluid flow via energy expenditure.

In contrast, PFC refers to the manipulation of a fluid flow *without* any energy expenditure, using devices such as fins, vanes, slats, flaps, riblets, or vortex generators. There are both advantages and disadvantages to using PFC. However, this review will

follow the path of advances made by AFC technology and its integration into civil transport aircraft.

With so many methods of achieving active flow control, there are multiple ways to classify them (Gad-el-Hak et al. 1998, Liddle and Crowther 2008, Cattafesta and Sheplak 2011, Wang et al. 2012, and Singh et al. 2014). One useful classification method is presented by Cattafesta and Sheplak, which organizes AFC devices by how they function (Figure 2.1).
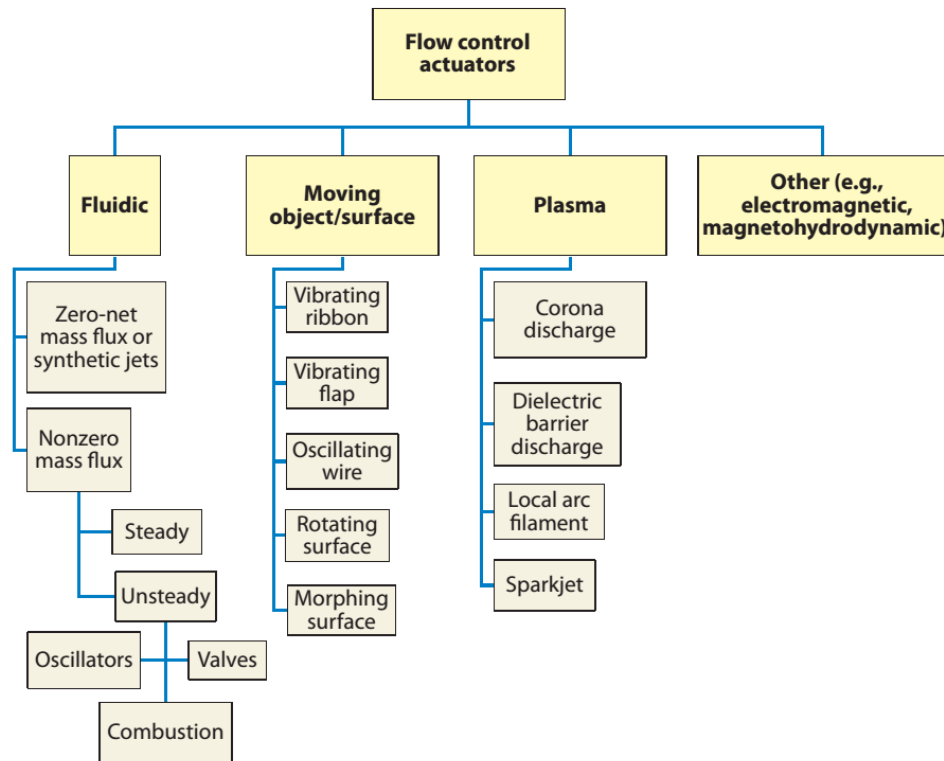
Figure 2.1. Classification scheme of AFC devices by function. (Cattafesta and Sheplak 2011)

The particular type of AFC device that this project utilizes falls under fluidic, nonzero mass flux, unsteady oscillation, which researchers refer to as fluidic oscillation. In this category, fluidic refers to the use of fluid injection or suction as opposed to a moving object/surface, plasma, or other type of mechanism to control fluid flow.

Furthermore, the nonzero mass flux term demonstrates the need for a fluid source or sink that injects steady or unsteady jet streams, as opposed to zero-net mass flux whereby linear momentum is transferred to the boundary layer (via injection and suction) such that there is zero-net mass flux, like the synthetic jet actuator (SJA). Next, the terms steady and unsteady describe the fluid flow that is expelled from the AFC device, the source of which can be constant or pulsed, respectively. The unsteady term has also been used to characterize zero-net mass flux fluidic devices (McLean et al. 1999). Finally, the "oscillators" branch refers to the natural design of the AFC device that allows the jet to self-oscillate; valves and combustion are other methods of producing the oscillations or pulses.

While examples for steady AFC devices are not discussed by Cattafesta and Sheplak (2011), there are powered, steady, high-lift fluidic systems called blown flaps, also referred to by terms such as "circulation control wing (CCW)," "upper surface blowing," "boundary layer control system," and "jet flaps" (Gologan 2010 and Mason 2012), that fall in the steady AFC device category. These systems have already been designed and integrated into aircraft where vertical and/or short take-off and landing (V/STOL) applications were desired, such as the Hunting H.126 (Figure 2.2) (Mason 2012). Gologan (2010) has broken down blown flaps into four categories: Upper Surface Blowing (USB), Externally Blown Flaps (EBF), Internally Blown Flaps (IBF), and Advanced Internally Blown Flaps (AIBF). USB and EBF typically utilize the engine exhaust to blow air over the upper surface or around the entire wing. On the other hand, IBF and AIBF describe systems that use pressurized gas to blow air out from the inside of the wing, which aligns with the primary research objective. While steady blowing is less efficient than unsteady blowing (Gologan 2010), there is design knowledge to be gained from IBF and AIBF integration into full-scale aircraft, which will be discussed in section 2.2.
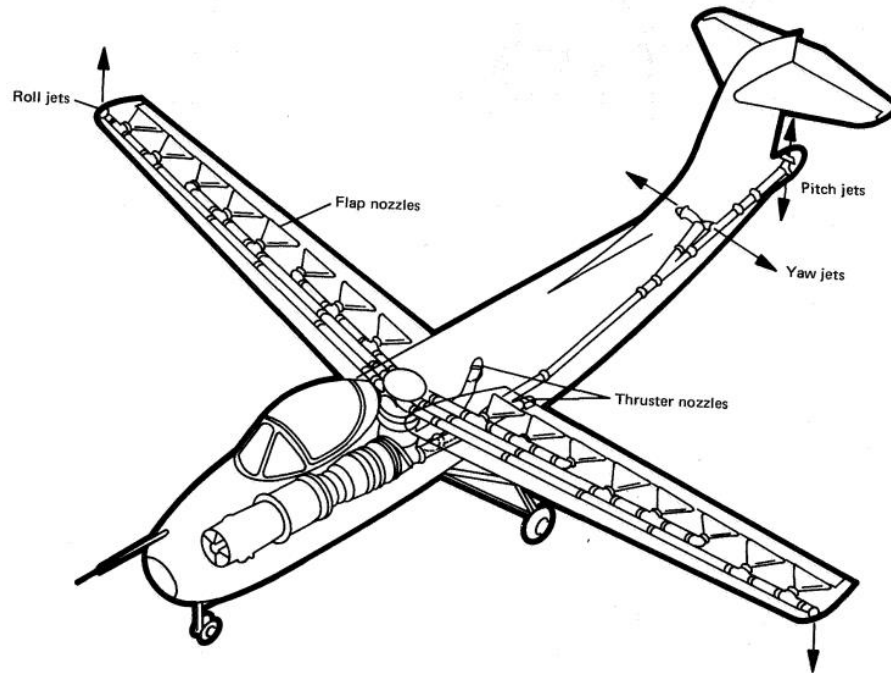
Figure 2.2. Schematic of full-scale Hunting H.126 blowing system (Aiken and Cook 1973)

Returning back to fluidic oscillators (also known as sweeping jet actuators, not to be confused with synthetic jet actuators), this class of AFC devices originated in the late 1950s and early 1960s in the Harry Diamond Laboratory based on patented designs by R. W. Warren, B. M. Horton, and R. E. Bowles for the express purpose of fluid amplification (Horton and Bowles 1965 and Warren 1962a). Those ideas sprouted into designs seen in other categories of flow control and also allowed the creation of a few other self-oscillating fluidic devices as reviewed by Raghu (2013) and Gregory and Tomac (2013). Gregory and Tomac (2013) have further classified fluidic oscillators into two categories based on how the oscillations are driven: wall-attachment and jet interaction. Wall-attachment fluidic oscillators incorporate a bi-stable attachment mechanism, which utilizes some type of control nozzle to force detachment and reattachment of the jet from one wall to the opposite wall. Complete attachment to a given wall is due to the Coanda effect, which has been studied and reviewed in the

8

context of fluidic oscillation by many authors including Warren (1962b) and Kadosch (1964). The control nozzle used typically comes in the form of a feedback tube, as seen in experiments accomplished by Spyropoulos (1964), Viets (1975), and Raman and Raghu (2004) (Figure 2.3.a). From there, Raghu (2001) was able to patent a fluidic oscillator design without the aid of physical feedback tubes (Figure 2.3.b), using a method that Gregory and Tomac (2013) label as jet interaction to oscillate the jet. This category encompasses any device where bi-stable wall attachment "is not a relevant mechanism" (Gregory and Tomac 2013). While a type of feedback interaction between internal jets occurs in the dome-shaped mixing chamber in Raghu's design, no physical feedback or control is present, cultivating the label "feedback-free fluidic oscillator" (Raghu 2001). Additionally, it is important to note that the characterization and categorization of these devices are relatively recent developments and may still require minor adjustments as evidenced by differing categorizations by Cattafesta and Sheplak (2011) and Wang et al. (2012) and the acknowledgment that the internal flow details of feedback-free fluidic oscillators are not fully known (Gregory and Tomac 2013).
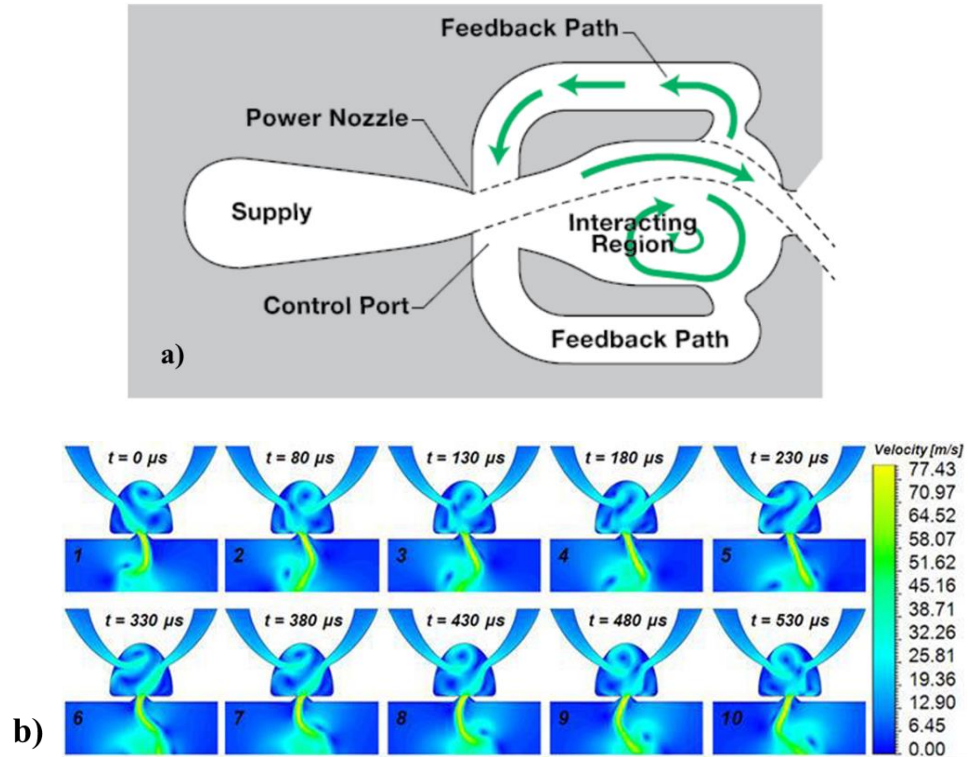
Figure 2.3. 2-D Fluidic oscillator design and flow depiction using a) feedback design (Raman and Raghu 2004 and Lin et al. 2016) and b) feedback-free design (Tomac and Gregory 2013)

One of the largest advantages of self-oscillating fluidic oscillators is the lack of moving parts, which increases the reliability and ease of assembly compared to other fluidic devices with multiple moving components. Additionally, it will be relatively simple to manufacture with only an extruded design with one material, as opposed to a design composed of multiple materials. Other advantages of self-oscillating oscillators include capabilities of producing larger disturbances and a larger range of frequency and the potential independent control of frequency and velocity (Cattafesta and Sheplak 2011). Some disadvantages include the requirement of external flow source and unsuitability for feedback control (i.e., difficultly of flow adjustment once the design has been manufactured) (Cattafesta and Sheplak 2011).

For more information regarding the history of flow control, refer to the text by Gad-el-Hak et al. (1998). Comprehensive reviews of active flow control include papers by Singh et al. (2014), Cattafesta and Sheplak (2011), and Wang et al. (2012). Issues that can occur during testing of active flow control are discussed by Collis et al. (2004). Finally, comprehensive reviews of, specifically, feedback and feedback-free fluidic oscillators are covered by Raghu (2013) and Gregory and Tomac (2013).

Regarding references to active flow control devices, the specific oscillator utilized in this thesis is a modified version of the feedback-free fluidic oscillator (DeSalvo et al. 2011). Henceforth, the usage of the terms "oscillator," "fluidic oscillator," or "actuator" will refer to the application of a feedback-free fluidic oscillator design unless otherwise noted. While any other unsteady AFC device could be considered for integration purposes, an executive decision was made to use the fluidic oscillator[2].

2.2 Advancements in AFC Technology Integration

As previously mentioned, AFC technology relevant to this project only includes devices that are integrated into the internal structure of an airfoil shape. Currently, "no civil aircraft uses AFC technology" (Bauer et al. 2014). Instead, there are multiple instances of integration of flow control into scaled models and full-scale models of airfoil shapes for research purposes and V/STOL applications. The discussion in this section will first focus on a group of papers that specifically address integrating AFC technology onto a full-scale, civil transport aircraft. Next, AFC technology integration into full-scale models and relevant research accomplished with scaled models will be covered as outlined in Figure 2.4. Under the full-scale model category, aircraft models and non-aircraft models integrating various categories of fluidic AFC technology will be

---

[2] Private Communications with Boeing

described. Regarding the scaled category, two research projects that capture previous work associated with the current project will be covered. While the purpose of most of these research cases was to ultimately determine if and how fluid flow was altered, the discussion here will highlight the designs used to integrate AFC technology into the internal structure of an airfoil. In contrast to a comprehensive review, only a few integration cases will be covered in this section.
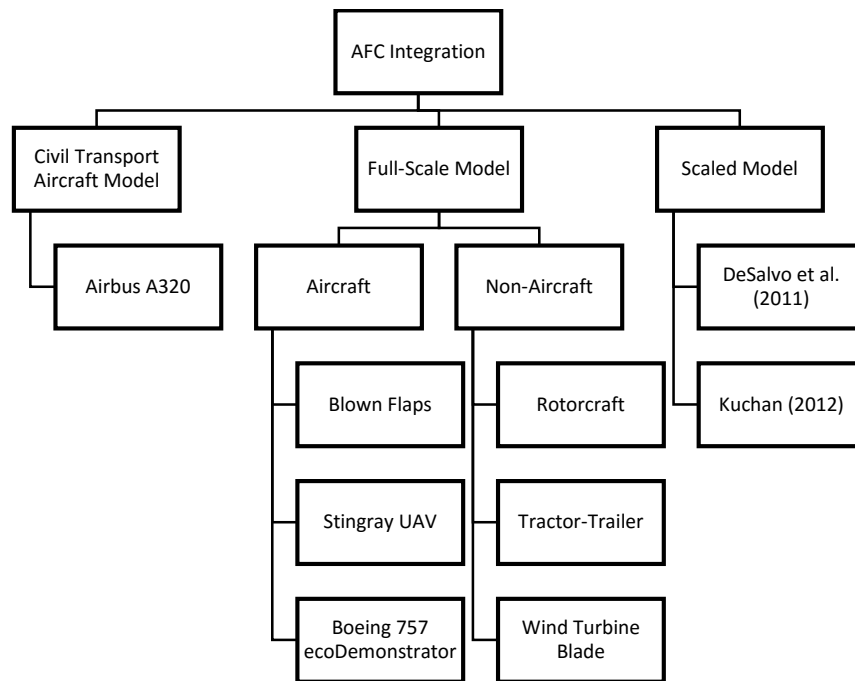
Figure 2.4. Diagram of discussed integration research

2.2.1 Civil Transport Aircraft Integration

The entire group of researchers discussed in this section have examined the application of AFC technology on an Airbus A320 aircraft. Liddle and Crowther (2008) begin by outlining systems and certification issues surrounding AFC application, including dispatch reliability (i.e., functional with redundancies), flight control systems, environmental protection (i.e., ice, water, and insects), indications to operators, and noise. Crowther and Gomes (2008) develop a mathematical method of modeling the mass and

12

power scaling of a SJA. Using that model, Jabbal et al. (2010) compare different power distribution systems (electric, hydraulic, and pneumatic) as well as different types of actuators. Among other things, they conclude that there is a tradeoff that exists between "system power efficiency and the system hardware mass required to achieve this efficiency" (Jabbal et al. 2010). As validation, they found that an electric power system with higher power efficiency has relatively heavier weight than a pneumatic power system (Jabbal et al. 2010). Further progress is made by Jabbal et al. (2014); one of their major findings was that, for a power transmission greater than 20 kW but less than 60 kW, pneumatic power distribution is more mass efficient than electrical power distribution.

Finally, Meyer et al. (2014) create a full-scale layout air duct system connecting compressed air, (representing engine bleed air) to an array of unsteady, feedback fluidic oscillators (Figure 2.5) while accounting for CS-25 safety requirements like the possibility of leakage, blocked actuators, or one engine failure. They found that four ribs (two at the ends and two in the middle) were sufficient to maintain the appropriate stiffness for an array of 16 actuators and associated plenum over the span of a A320 flap (Meyer et al. 2014). Additionally, investigating the trade-off between a larger plenum but weaker rib versus a smaller plenum but stronger rib, they found that at least a 30 mm diameter plenum at 40% span length allowed for "sufficient homogeneity of the jet outlet velocity," given one-sided pressurization (Meyer et al. 2014). While the scope of this project does not include designing the air-supply system, research involving certification issues, safety requirements, and estimated number of actuators per flap will support integration design decisions.
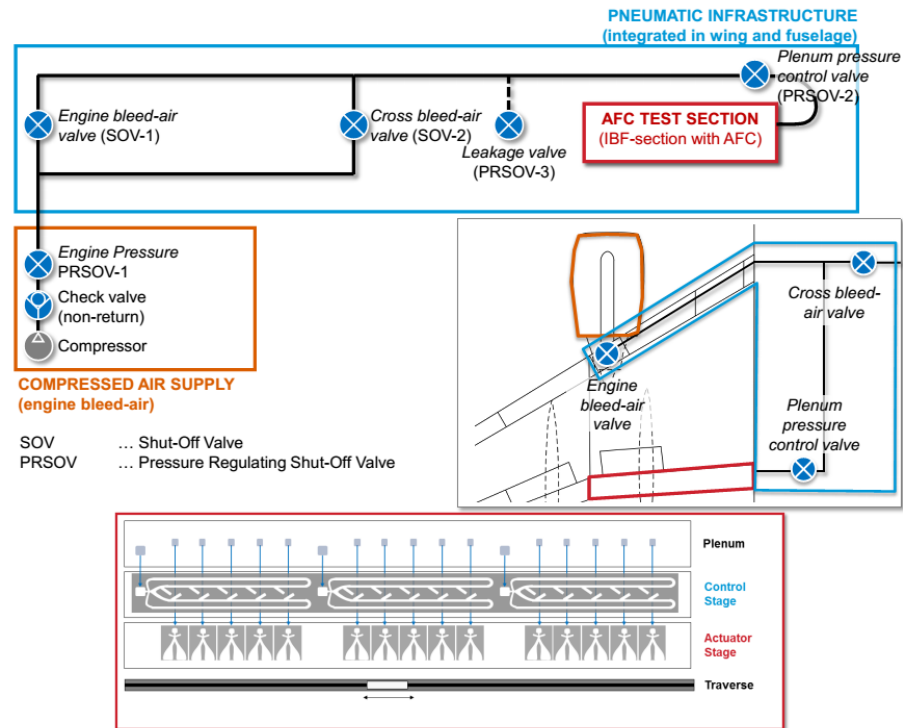
Figure 2.5. Diagram of laboratory equivalent of pneumatic AFC system on A320 (Meyer et al. 2014)

2.2.2 Full-scale Integration

The first AFC devices to be integrated into full-scale airplanes were internally blown flaps, which showed up on research planes, such as the Hunting H.126, Balls-Bartoe Jetwing (Mason 2012), and C-8A De Havilland Buffalo (Gologan 2010), and V/STOL applications, such as the ShinMaywa US-1A and the Lockheed F-104 "Starfighter" (Meyer et al. 2014). Since the air does not oscillate, the systems required only straight slots that could be a long slit as in the Ball-Bartoe Jetwing (Solies 1992) or an array of slits as in the Hunting H.126 (Aiken and Cook 1973). Of the systems examined, the slots have been integrated into a metal airfoil, connected by a series of ducts to a compressed air source (Figure 2.6) (Hunting. 1963, Aiken and Cook 1973, Solies 1992, Chambers 2005, Wright 2003, Sobelman n.d.). While the details of the integration are not revealed, the nozzle interface at the skin seems to have a sort of

14

"knife-edge" sharpness to help the fluid flow tangentially to the skin. Despite being considered the "most efficient form of powered lift for fixed-wing aircraft," IBFs suffered the disadvantage of the weight, cost, complexity, and maintenance associated with the required internal air ducting in addition to reduced volume for other systems (Chambers 2005).
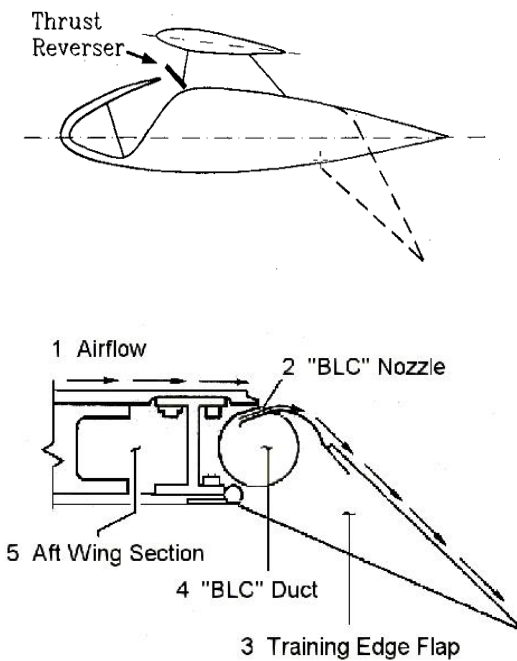
Figure 2.6. Cross-sectional view of Ball-Bartoe Jetwing wing (Solies 1992) (top) and Lockheed F-104 (Sobelman n.d.) (bottom)

With greater benefits seen from unsteady AFC devices, one full-scale application of an SJA was on an Uninhabited Air Vehicle (UAV) nicknamed the "Stingray." Here, an array of actuators was integrated into a composite skin at the airfoil LE (Figure 2.7). Due to the orientation of the SJA perpendicular to the freestream, a straight slit could be created at the LE, allowing the array of SJAs to extend out to the freestream (Kondor et al. 2005). Additionally, with the relatively small size of the Stingray, the SJAs were

15

simply supported by packing in the space at the LE and fastened onto support structures in the custom-made skin.
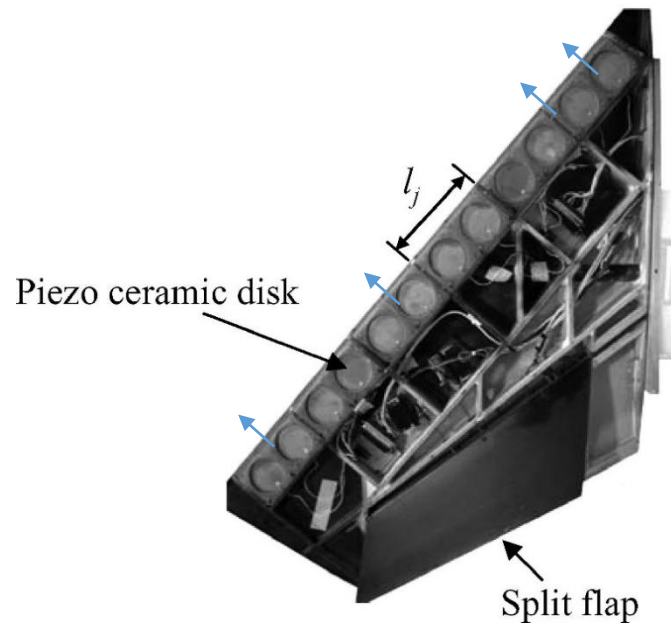
Figure 2.7. Top view of SJAs integrated into wing structure of the Stingray UAV with blue arrows marking SJA pulse direction (modified from Amitay et al. 2004)

On the Boeing 757 ecoDeomonstrator, The Boeing Company (Boeing) has demonstrated the integration of unsteady, feedback, fluidic oscillators into the vertical tail. Due to the simple design of the oscillator, which contains no moving part, metal pieces are sandwiched together with multiple fasteners to create an array of fluidic oscillators (Figure 2.8) (Lin et al. 2016).
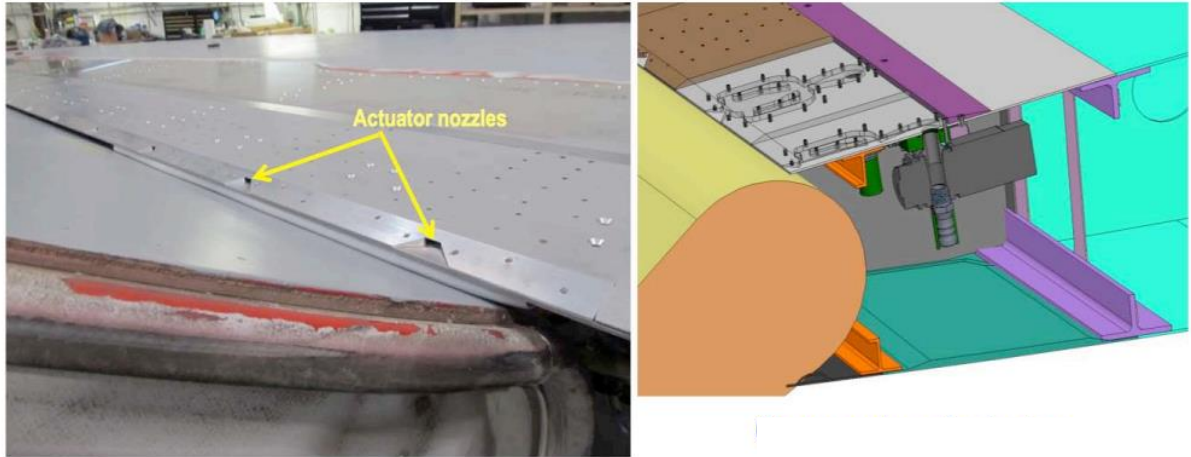
Figure 2.8. Oscillator fastened together on the vertical tail (Lin et al. 2016)

The feedback fluidic oscillators are then covered by the outer skin with nozzle cutouts aligning with the oscillator jet nozzle (Figure 2.9) (Lin et al. 2016). The oscillating nature of the jet along with the desire for near tangential flow forces the nozzle cutout to take a trapezoidal shape as opposed to a square slit as in the previous cases.
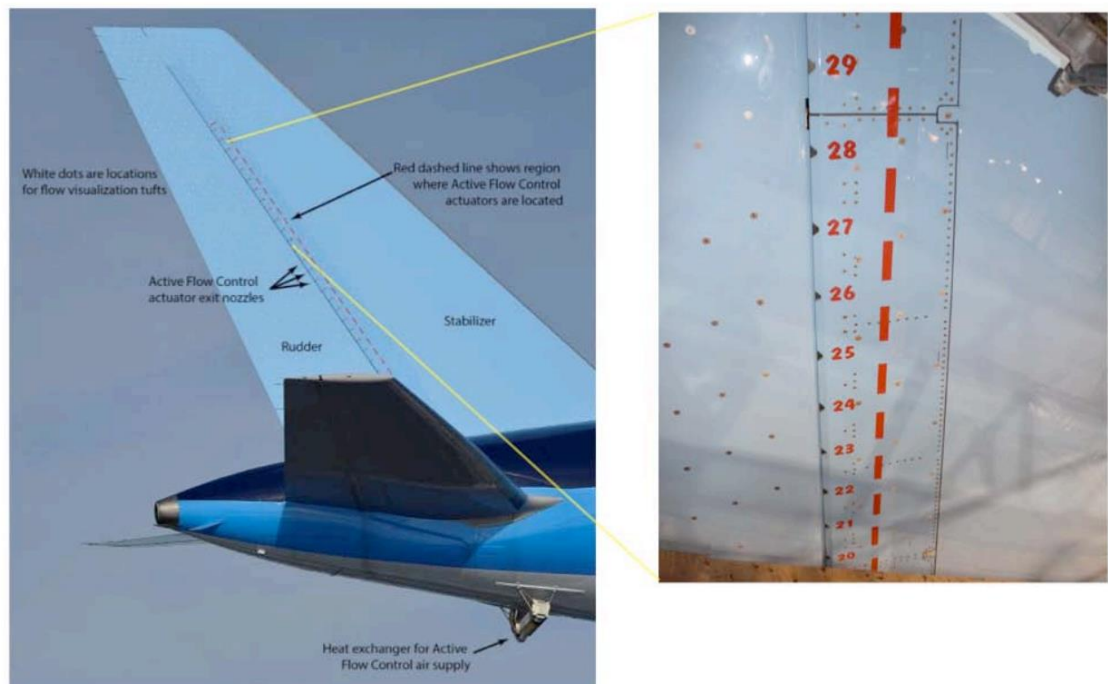
Figure 2.9. Oscillators covered by skin with nozzle cutouts (Lin et al. 2016)

Moving onto other non-aircraft AFC technology integration, there has been some discussion on integrating AFC devices onto the blades of a rotorcraft (Few 1987, Le Pape et al. 2013). However, for full-scale integration, steady AFC (referred to specifically as Circulation Control) has been integrated into the tail boom of a helicopter, which has been labeled as a No Tail Rotor (NOTAR) system, starting in 1990 with the MD520N (Stephens 2012). Today, MD Helicopters still incorporate the NOTAR anti-torque system to facilitate a safer and quieter ride than a helicopter with a tail rotor (Stephens 2012). The AFC system interface with the composite tail boom is composed of two slots running the length of the tail boom (Figure 2.10), which can produce "up to 60% of the anti-torque required in a hover" (MD Helicoptors 2014).

Figure 2.10. MD600 that utilizes the NOTAR system on the tail boom (left) and cross sectional view of the tail boom (right) (Stephens 2012)

Another full-scale vehicle that is able to employ steady AFC (Robert Englar of Georgia Tech Research Institute) and unsteady AFC (Avi Seifert of Tel Aviv University) is the tractor trailer (ATDynamics 2011). Without a need for a complex oscillating design, the steady AFC system's interface with the outer skin consists of a long slot, allowing for the air to flow tangential to the skin (Figure 2.11) (ATDynamics 2011). On the other hand, the unsteady system consists of a long slot filled by an array of separately manufactured AFC devices fastened directly on the airfoil (Figure 2.12) (ATDynamics

2011). As can be seen from the figure, the devices are not tangential to the free stream and, instead, are constricted to a certain angle due to the straightness of the devices in contrast to the curve of the airfoil.

Figure 2.11. Steady AFC system integrated into back of trailer (ATDynamics 2011)
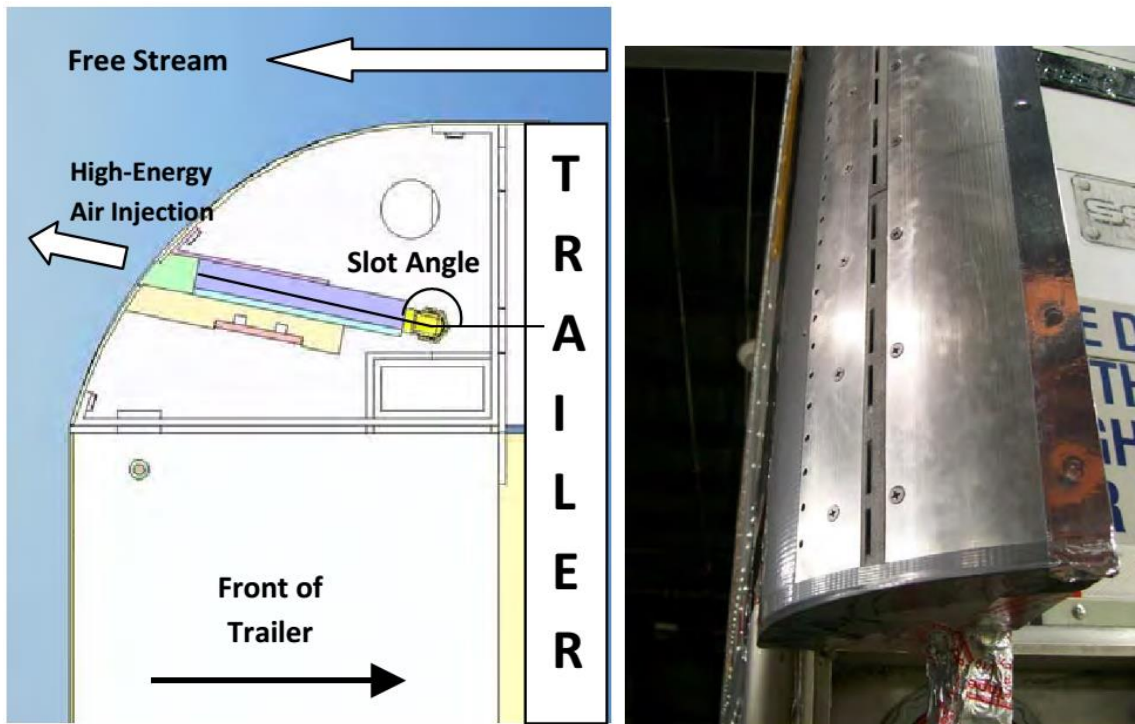
Figure 2.12. Unsteady AFC system integrated into back of trailer (ATDynamics 2011)

Finally, using the same unsteady AFC device as in Figure 2.12, Seifert et al. (2015) perform the integration at the root of a full-scale wind turbine blade (Figure 2.13). As seen in the figure, an oblong shaped slot is cut out of the skin with the separately manufactured AFC device sticking through the cutout. While the model has yet to be tested in the field, initial wind tunnel tests have validated a functioning integration design with favorable results (Seifert et al. 2015).

Figure 2.13. Unsteady AFC device integrated into root of wind turbine blade (Seifert et al. 2015)

Comprehensive designs of the integration of AFC devices are not readily available, most likely due to the proprietary nature of AFC application to specific structures. Nonetheless, in the cases examined in this section, it is clear that steady AFC systems only require a simple slot that acts as the nozzle in the airfoil skin to achieve flow control. Similarly, for unsteady AFC systems, a simple slot is created in the skin. However, due to their more complicated design, unsteady AFC devices are manufactured

separately and then inserted through the slot such that the nozzle protrudes out to meet the surface of the skin and the remaining slot space is filled to maintain the shape of the airfoil (Figures 2.12 and 2.13). Moreover, as in the case of the 757 ecoDemonstrator, there are complex nozzle-shaped cutouts on the skin that align with the unsteady AFC device nozzles. Thus, these two designs, a simple slot cutout and a more complex slot cutout, will be considered in this research project as potential solutions for unsteady AFC device integration.

2.2.3 Scaled Integration

Regarding the design of AFC integration, DeSalvo et al. (2011) compared a "stepped" configuration to a "recessed" configuration integration of a feedback-free fluidic oscillator. Both configurations allow for air to flow tangentially to the bounding surface. However, the recessed configuration attempts to reduce the loss in lift caused by the backwards facing step in the stepped configuration, at the cost of a larger hole for the nozzle. Working in conjunction with Boeing, they determined that the recessed configuration, similar to the design seen in Figure 2.13, enhanced the "interaction of the jets with the cross flow," thus increasing the lift for a given momentum coefficient (DeSalvo et al. 2011). From the series of experiments and papers produced by DeSalvo, Whalen, and Glezer emerged the objective, as detailed in chapter 1, of a larger AFC device integration design project of which this research is one part.

Kuchan (2012) tackles this project by evaluating a wide range of designs for embedding an array of feedback free fluidic oscillators that share a single plenum. The designs were broken down into four external configurations, which support the AFC device from outside of the flap while maintaining the airfoil shape, and three internal configurations, which support the AFC device from inside the flap. After modeling the designs, manufacturing carbon fiber flaps, and discussing advantages and disadvantages, Kuchan determines the best configuration as an internal "vertically inserted" design and

the second best configuration as an internal "side inserted" design. Additionally, she rapid prototypes the oscillators with stereolithography (SLA) to note preliminary issues such as warping, fractured pieces, and the need for rounded corners and edges.

One area that lacks consideration, however, is the method of attachment, of which only two are mentioned: pins and studs (Kuchan 2012). Moreover, only SLA is considered as the manufacturing method, which does not take into consideration the potential production volume or material of the full-scale actuators. Finally, a scaled model of a flap is utilized, resulting in designs such as a foam core support structure, which becomes problematic if other designs are more efficient at manufacturing and assembling at a larger scale. Therefore, by designing AFC device integration into a civil transport aircraft, full-scale cost, weight, and manufacturing and assembly processes can be taken into consideration before choosing a final design. Using information gained from the two papers in this section, it will be possible to design a more robust integration solution.

2.3 Fluidic Device Production

The integration solution includes manufacturing and assembling the fluidic device itself. Thus, in this section, design in light of manufacturing procedures is considered first. Next, the manufacture of the parts will be discussed; the manufacture of microfluidic devices, characterized as miniature versions of fluidic devices, is included as part of this discussion. Although microfluidic devices do not necessarily oscillate fluids, a common interest they share with fluidic oscillators is the requirement of manufacturing channels through which fluid flow. Following that, a set of reviews that cover the manufacture of macro-scaled fluidic devices will build on the list of available manufacturing processes to select from. Finally, current assembly methods for polymer microfluidic devices will be covered.

Thermoplastic manufacturing and assembling processes will primarily be discussed in this section to limit the scope. A few other fluidic manufacturing processes, such as those for thermoset and ceramic materials, will be mentioned as applicable.

2.3.1 Fluidic Device Design

The hollow design of a polymer, fluidic device typically requires the device to be made with a minimum of two parts and then sealed. The first part contains the fluidic channels, while the second part can simply cover the top surface of the first part (Figure 2.14.a) or encase the entire first part (Figure 2.14.b) (Schultz et al. 2008). A design of a device that requires a minimum of one part and a sealing procedure was introduced by Bauer (1981), where a living hinge is incorporated into the design such that the two aforementioned parts are joined together (Figure 2.15). While the manufacturing process will be more complex, the design allows for a simpler alignment process and a reduction of a manufacturing process for a separate part. As additive manufacturing methods have become more prevalent in recent years, fluidic devices are beginning to be manufactured as one finished product without the need for sealing, especially for research purposes (ATDynamics 2011, DeSalvo et al. 2011, and Kuchan 2012). This is particularly advantageous in that an assembly step is eliminated and thus the probability of part defect is lowered.
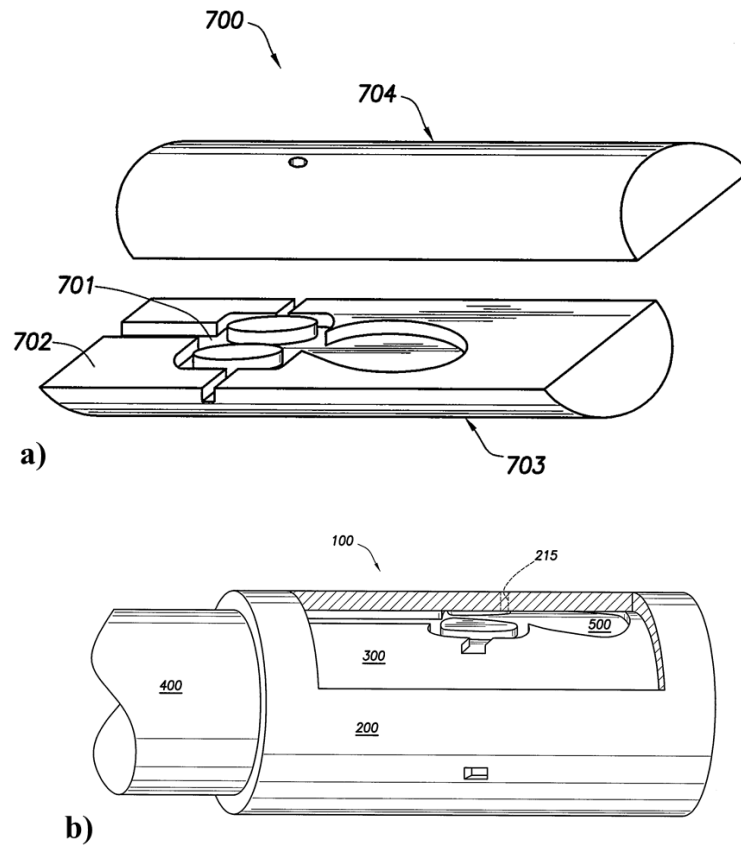
Figure 2.14. Engraved part and a) top cover or b) sleeve (Schultz et al. 2008)
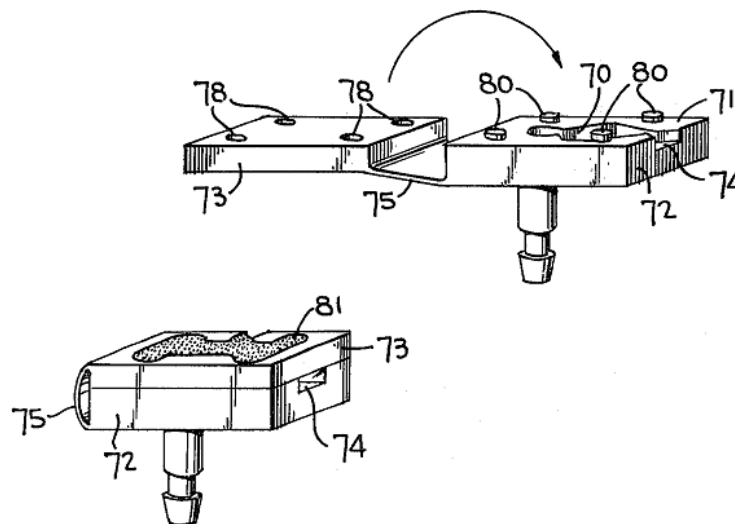
Figure 2.15. One actuator with living hinge that can be sealed shut (Bauer 1981)

<u>2.3.2 Fluidic Device Manufacturing</u>

Becker and Gärtner (2008) provide a thorough review on polymer fabrication techniques for microfluidic systems, in which precision machining, laser ablation, thermoforming, injection molding, hot embossing, injection compression molding, and precision machining are standard methods for use on thermoplastic material due to the large process window between the glass transition temperature, T_g, and the decomposition temperature, T_D. While laser ablation is limited by small depths of cuts (on the order of 1 micron), precision machining, thermoforming, injection molding, hot embossing, and injection compression molding (a combination of "basic principles of injection molding and hot embossing" (Becker and Gärtner 2008)) are also viable manufacturing techniques for macro-scale manufacturing. Precision machining requires long processing times and thus is recommended only for prototyping (Becker and Gärtner 2008). With thermoforming and hot embossing, a thin sheet of material is placed in a system, heated up, pressurized or pressed, respectively, to fit a master mold, and finally cooled. Both methods are suitable for low to medium production rates. Hot embossing, in particular, maintains cycle times on the order of "4 – 15 minutes for a 4 in. wafer" (Becker and Gärtner 2008). Injection molding and injection compression molding are better suited for larger production rates with short cycle times on the order of 30 seconds to 5 minutes for the former and 5 to 10 seconds for the latter (Becker and Gärtner 2008). Although injection compression molding has a quicker cycle time than injection molding, injecting the melt and compressing the mold require additional complexity to the equipment and process (Becker and Gärtner 2008).

Regarding macro-scale fluidic device manufacturing, Figure 2.16 shows estimates of economically viable manufacturing methods for certain production rates of fluidic devices (Humphrey and Tarumoto 1965). Although casting, transfer molding, and jet molding can utilize thermoplastic material, they typically utilize thermoset material and are more efficient at doing so; photoetching can only be applied to photopolymer

materials. The remaining methods include sawing and drilling (machining),

thermoforming, injection molding, and injection compression molding, which validate

the processes used for microfluidic devices. Figure 2.17 demonstrates general economic

batch sizes for some of these processes. Were the material constraint removed, other

processes are available for creating thermoset, ceramic, and metal fluidic oscillators. One

method to note is electroforming, which can form a metal fluidic device as one part.

Weathers (1972) acknowledges these techniques; furthermore, Weathers mentions a

ceramic molding process that can also create the device in one piece.
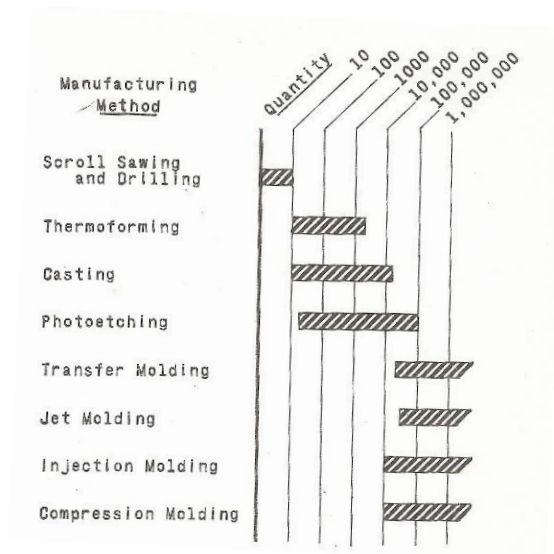
Figure 2.16. Specific comparison of economic batch sizes for fluidic devices from a survey of manufacturing companies (Humphrey and Tarumoto 1965)
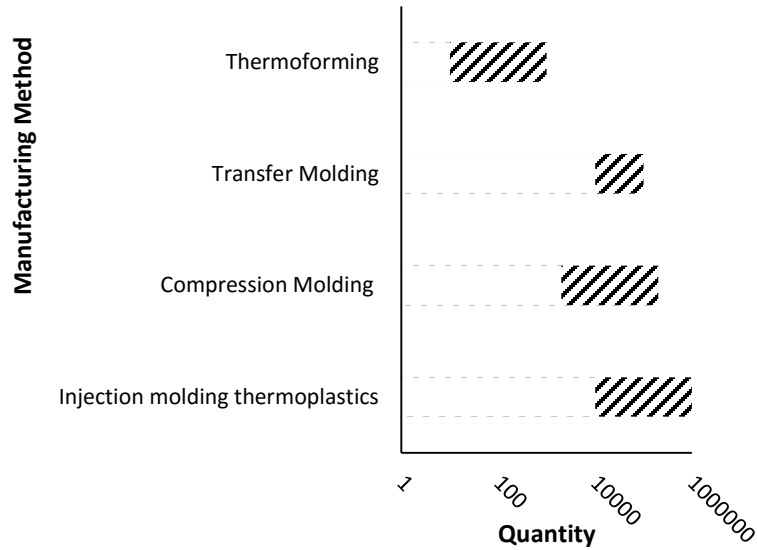
Figure 2.17. General comparison of economic batch sizes for plastic parts (CES EduPack 2015)

Finally, with the expansion of rapid prototyping research, the economics of 3D printing have become more viable. Currently, in research settings (DeSalvo 2011, Kuchan 2012, Melton 2014), SLA has been an effective manufacturing method for producing thermoset fluidic oscillators (both feedback and feedback-free) in one piece. SLA works by curing a photopolymer resin with UV light in specific locations. Other manufacturing methods, such as fused deposition molding (FDM) and selective laser sintering (SLS), suitable for creating thermoplastic fluidic devices in one piece have not been discussed in fluidic literature yet. Thus, it is a research area of significant importance for this project.

2.3.3 Fluidic Device Assembly

Once the oscillator pieces are manufactured, post processing steps for thermoplastics include removing waste material, such as the remaining sheet material from hot embossing or the sprue from injection molding, and encapsulating the fluidic channels if there are two or more parts per oscillator (Becker and Gärtner 2008). Encapsulation require fastening and sealing both parts together, which can be

accomplished in one procedure. With thermoplastic devices, there are two categories of encapsulating: indirect bonding and direct bonding (Tsao and DeVoe 2009). Indirect bonding refers to another material, namely adhesive, that acts as the bonding agent, which can result in "channel sidewalls with different chemical, optical, and mechanical properties than the bulk polymer" (Tsao and DeVoe 2009). On the other hand, direct bonding involves utilizing the part itself to act as the bonding agent, which retains the desirable properties of the part material.

Direct bonding is further divided into four categories: thermal fusion bonding, solvent bonding, localized welding, and surface treatment and modification. Thermal fusion bonding involves heating the part(s) and applying pressure for a certain amount of time. Solvent bonding involves solvating the part(s) with a liquid or vapor chemical solvent and mating the parts under pressure. Localized welding utilizes energy, such as ultrasonic, microwave, or infrared wavelength energies, to induce heating and softening of the material for localized sealing. Finally, other treatments (e.g., surface grafting, acid, vacuum and atmospheric plasmas, and ultraviolet light) that increase the surface energy between mating surfaces are categorized under surface treatment and modification. Advantages and disadvantages associated with different bonding methods within each category are presented in a comprehensive review and Table A.1 by Tsao and DeVoe (2009). Finally, Humphrey and Tarumoto (1965), Weathers (1972), and Becker and Gärtner (2007) acknowledge that either indirect (e.g., dry-film adhesive) or direct bonding (e.g., ultrasonic welding) are suitable methods for larger fluidic devices.

2.4 Chapter Summary

Following an examination of the categories and requirements of AFC devices, observations were made of how certain categories of AFC systems have been or are currently being integrated into scaled and full-scale airfoil shapes, which will support integration design decisions regarding features such as the nozzle hole shape on the

airfoil or the fluidic oscillator interface with the skin. Further examination of fluidic device designs, manufacturing processes, and assembly processes has created a platform of potential options to select from, in addition to the identification of an unexplored area of fluidic manufacturing using FDM and SLS. Thus, the following chapter continues to explore the differences in fluidic manufacturing methods through experimentation.

CHAPTER 3

FLUIDIC OSCILLATOR EXPERIMENTAL TESTING

As mentioned in chapter 1, the secondary objective of this work, which involves examining the effect(s) different manufacturing processes have on fluidic performance, is able to support design decisions made for the primary objective, which involves designing the integration of a feedback-free fluidic oscillator into a flap structure. To fulfill the secondary objective, an experiment was constructed to test the effect(s) that surface roughness and geometric dimension(s) and tolerance, resulting from various manufacturing methods, had on the symmetry of oscillations.

3.1 Experimental Design

Given the research on manufacturing fluidic devices, it is understood that machining, thermoforming, injection molding, hot embossing, and injection compression molding are viable manufacturing methods for medium to large production rates of thermoplastic fluidic or microfluidic devices. All of these methods, with the exception of machining, require molds. Additionally, the surface roughness and tolerance of the internal fluidic channels are only as good as the qualities of the initial mold. Thus, injection molding was chosen as the manufacturing process to represent the molding process of a fluidic device due to its relative ease of accessibility. Moreover, injection molding shall represent an industrial standard of manufacturing. CNC machining and stereolithography (SLA) were selected as two baseline manufacturing methods due to high smoothness and precision during manufacturing and their standard usage in AFC research. Finally, fused deposition molding (FDM), a process that heats up and deposits thermoplastic material, and selective laser sintering (SLS), a process that laser sinters powder, were selected as the final two methods to compare due to their growing

prevalence and acceptance as large-scale manufacturing systems (Bak 2003), their capability of creating a fluidic device in one piece, and their potential contribution to the fluidic device manufacturing research field.

After discussion with Prof. Ari Glezer of Fluid Mechanics Research Laboratory (FMRL) at Georgia Institute of Technology (Georgia Tech), a model six times the unit size of their base fluidic oscillator model was determined to be an approximate representation of a full-scale fluidic oscillator application. Thus, the design for this experiment was created such that fluidic oscillator inserts of the "six times" variation (Figure 3.1) could be manufactured and inserted into a larger test module (Figure 3.2) without changing the entire test rig for each manufacturing method. Figure 3.1 is intentionally blurred to protect proprietary information.
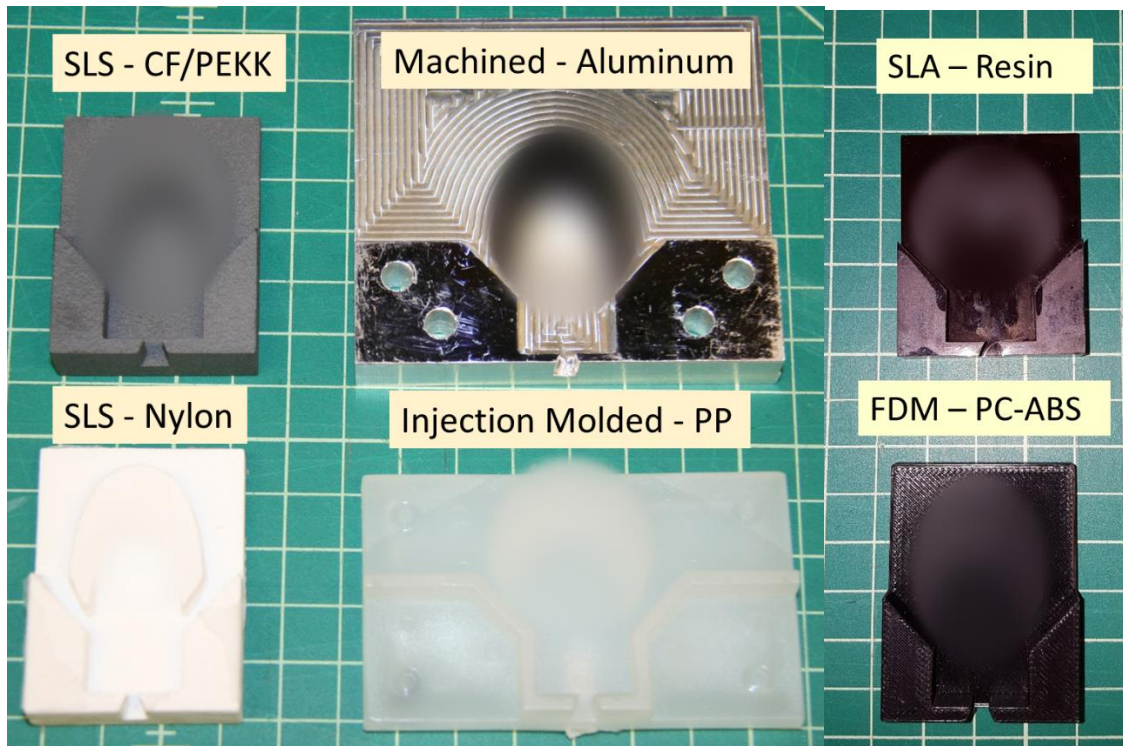
Figure 3.1. Manufacturing method and material labeled above respective inserts
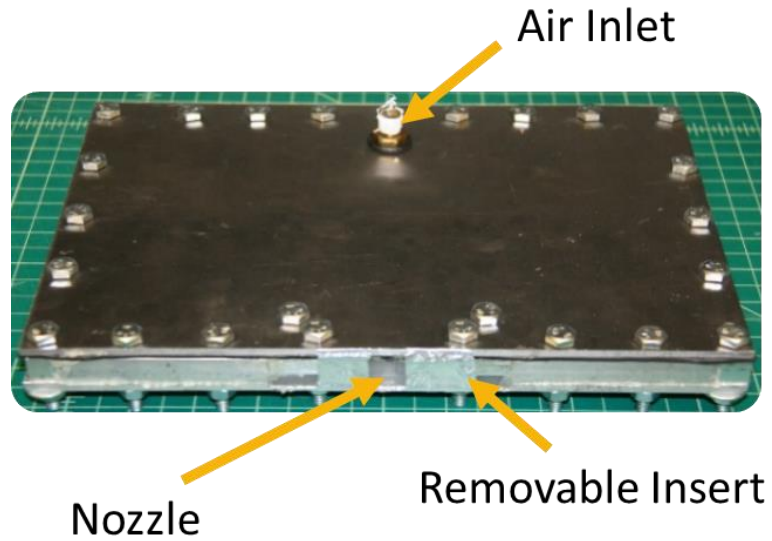
Figure 3.2. Reusable test module

Due to the inability of the machining and injection molding processes to create encapsulated parts as discussed in section 2.3, only the bottom part with the fluidic design was manufactured with each process. Thus, the inserts were created as a single bottom piece, with a nominal nozzle width-to-height ratio of 1:3, where the nozzle width is equivalent to the dimension B in Figure 3.3, and a nominal Aspect Ratio (AR) of 0.08, where

$$AR = \frac{B}{E} \tag{3.1}$$

and B and E are dimensions defined in Figure 3.3.
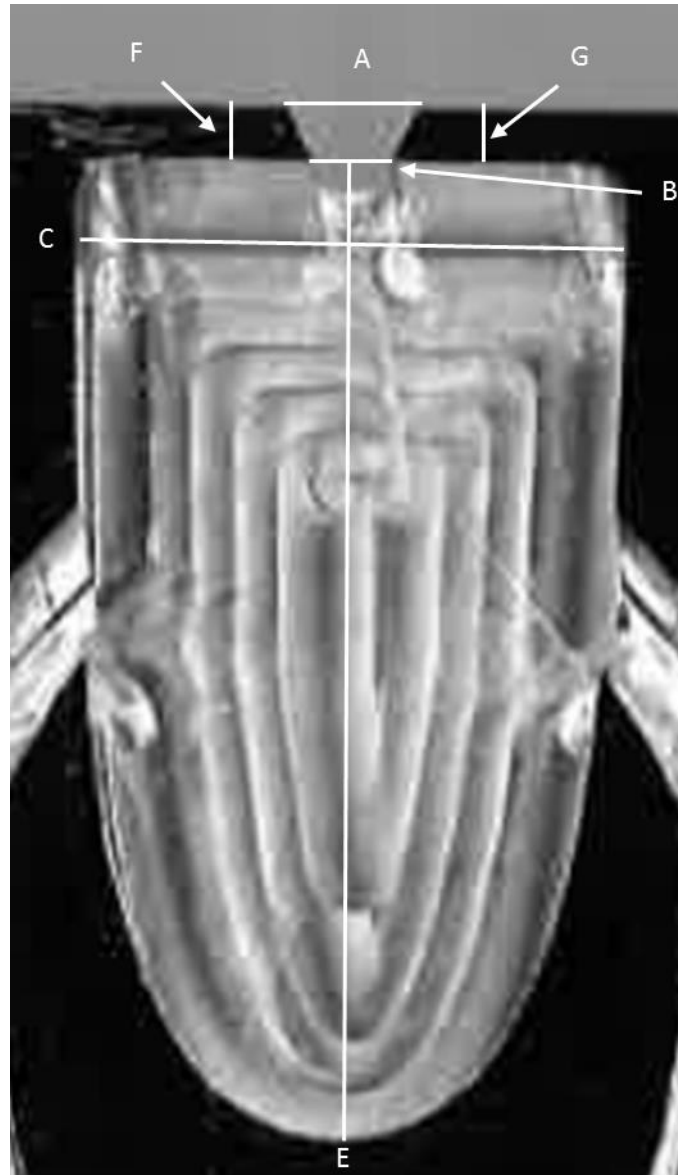
Figure 3.3. Dimension definitions

Different materials were utilized for each manufacturing procedure, as it was assumed that different material properties would not significantly affect the test results and that the manufacturing characteristics imparted to the inserts would not depend on material. Thus, readily accessible materials were utilized for each manufacturing method (Table 3.1).

Table 3.1. Tested manufacturing method with associated material

Manufacturing Method	Material	Design
Machined	Aluminum (Al)	1
Machined	Al	2
Machined	Al	3
Injection Molded	Polypropylene (PP)	2
Selective Laser Sintering (SLS)	Nylon	2
SLS	Carbon Fiber (CF) reinforced polyether-ketoneketone (PEKK)	2
Fused Deposition Molding (FDM)	Polycarbonate-Acrylonitrile butadiene styrene (PC-ABS)	2
Stereolithography (SLA)	RenShape® SL (Resin)	2

During manufacturing of the machined insert, dimensions F and G were serendipitously decreased by a machining error by about 0.05 inches (Design 1), which was discovered after an initial round of testing. Thus, machined inserts of nominally correct (six times unit) dimensions (Design 2) and of a thickness 0.05 inches greater than nominal (Design 3) were manufactured for testing to determine the effect of this geometric dimension. It is important to note that dimension A was necessarily decreased or increased as a result of the altered wall thickness and that the internal corners required a radius the size of the drill bit, ~1/16 inch diameter, due to the machining process. Machined aluminum designs 1, 2, and 3 will be referred to as Al 1, Al 2, and Al 3, respectively. Additionally, all other inserts will be referred to by their manufacturing method (e.g., Inj. Molded, SLS, FDM, SLA); the two SLS inserts will be differentiated by their material (e.g., SLS: Nylon or SLS: CF/PEKK).

Two test modules (Figure 3.2) were constructed out of a 1/8 inch and a ¼ inch thick aluminum sheet, ½ inch thick aluminum square bars, and a 1/16 inch thick rubber gasket sheet. A slot was milled 1/8 inch deep into the bottom, ¼ inch thick aluminum

sheet so that the inserts slid into position, and a ¼ inch diameter hole was drilled in the top aluminum sheet for the air inlet, sealed by an O-ring. Originally designed to test a fluidic oscillator design eight times the unit size, the module width was three times the oscillator width and two times the length, creating a large enough plenum to allow for even distribution of the air flow inside the module before exiting the nozzle. The aluminum six times insert (Figure 3.1) was smaller and thus able to use the same test module, albeit with extra supporting material such that the oscillator sat flush against the gasket. Remaining plastic inserts (Figure 3.1) are much smaller and required an additional fitting to match the shape of the aluminum insert.

From the gasketed joints equation (Budynas and Nisbett 2011),

$$3 \leq \frac{\pi D_b}{Nd} \leq 6 \tag{3.2}$$

where D_b is the bolt circle diameter, d is the bolt size/ diameter, and N is the number of bolts, 25, ¼-1.5 inch bolts were determined to be sufficient to maintain uniform pressure at a gasketed joint with a bolt circle diameter of 9.32 inches. The bolts were more or less evenly spaced apart and were used to clamp the entire test rig together. 3M spray-on adhesive was used to bond the gasket to the top cover, while room temperature vulcanized silicone (RTV) was used to ensure a tight seal at all other interfaces.

Finally, surface roughness and geometrical dimensions and tolerances in Figure 3.3 were measured to quantify the manufacturing characteristics. To quantify the fluidic oscillator performance, pressure, frequency, and velocity profile were measured at a given volumetric flow rate, Q.

3.2 Experimental Methodology

Once an insert is secured inside the module, calibrated hot wire anemometry is used to conduct oscillation frequency measurements of air in 50 L/min increments from $Q = 0$ L/min to $Q = 300$ L/min at a spanwise (along the z axis) point of maximum oscillation for a fixed streamwise (along the x axis) location of x = 3 mm (Figure 3.4). At

the same time, the gauge pressure in the line is measured ~100 mm upstream of the air inlet for each of the flow rates.
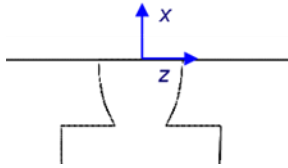
Figure 3.4. 2D diagram of fluidic oscillator nozzle and coordinate system

Next, hot wire anemometry is used to measure the velocity profile, defined as a spanwise profile of streamwise velocity, in increments of 0.635 mm for a total range of $\Delta z = 50$ mm at $x = 3, 8, 15,$ and 25 mm and at $Q = 50, 150,$ and 300 L/min. The x distances are chosen such that features in the velocity profiles are clearly seen. Each measurement is time-averaged over ½ second results; the raw data gathered from the hot wire are processed through a LabVIEW algorithm to obtain the frequency and velocity data. The entire test configuration is depicted in Figure 3.5.
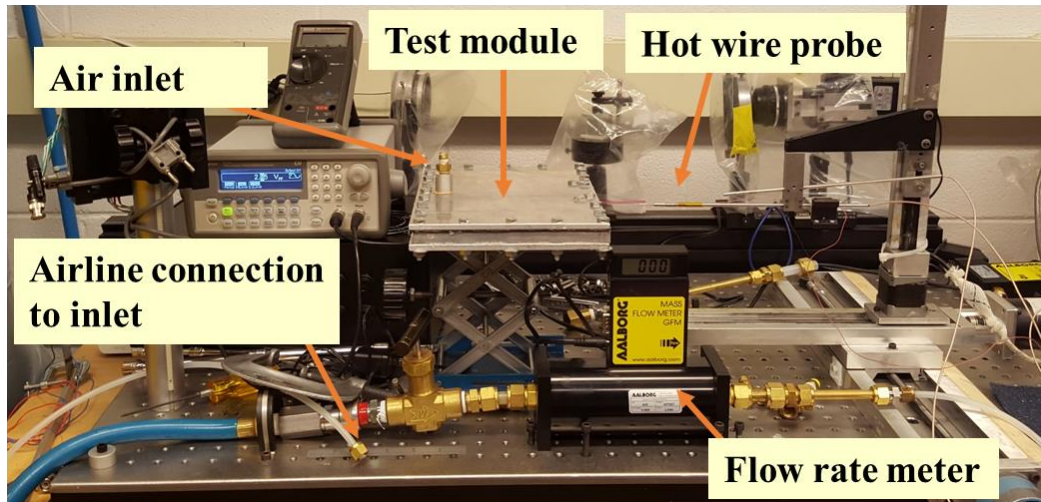
Figure 3.5. Side view of frequency, pressure, and velocity profile test configuration in the FMRL at Georgia Tech

Finally, surface roughness and geometric dimensions are characterized with a Zeta 3D Optical Profiler with a 5x lens. Arithmetic average of absolute roughness profile values, R_a, are measured on the x-z plane (Figure 3.4) through five cross sectional 1600 micron lines, spaced 20 microns apart with Zeta Instruments' associated software (Figure 3.6). Geometric dimensions are gathered through the same software by measuring lengths defined by the user. The differences between the measured dimensions and their respective nominal dimensions are calculated; the maximum differences are defined as the manufactured tolerances for the respective inserts. Additionally, these dimensional changes may, in turn, affect the oscillating jet in some capacity. Thus, a critical dimension to examine is the AR that resulted for each insert, since the AR was proven to affect the oscillation frequency of feedback-free fluidic oscillators (Tomac and Gregory 2012). In the end, surface roughness, measured tolerance, and AR will be compared against the performance of each insert to determine associated trends, if any.
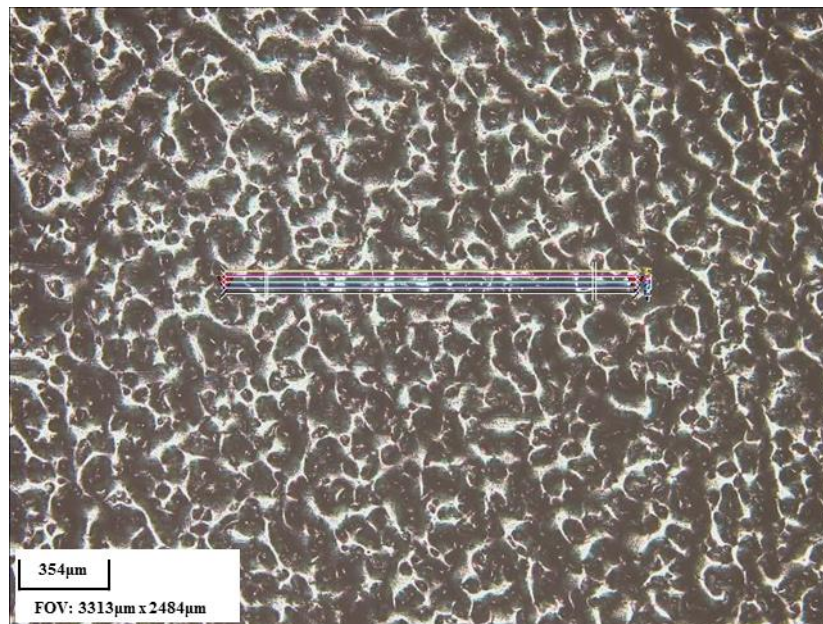
Figure 3.6. Surface of injection molded insert at 5x magnification with measurement lines

3.3 Experimental Results and Discussion

3.3.1 Frequency

Most oscillation frequencies were within 14% of the average frequency at each flow rate, excluding the frequencies for Al 1 and Al 3 due to their different designs (Figure 3.7). Only the FDM insert saw a 24% greater than average frequency at 50 L/min. This demonstrates that, at least for all parts with Design 2 nominal dimensions, the range of frequencies between the different manufacturing methods is almost constant as the flow rate increases. Additionally, the frequencies for Al 1 is within 11% of the average frequencies as defined above, whereas Al 3 is at least 30% greater than those frequencies. Thus, there may be unknown factors affecting the increased frequency for Al 3. Nonetheless, from discussions with Dr. Michael DeSalvo of Georgia Tech's FMRL, the frequencies of Design 2 are desirable given the Design 2 dimensions. Based on previous tested conducted by researchers from the FMRL, fluidic oscillators of Design 2 at 300 L/min ought to have produced oscillation frequencies in the range of 850 – 900 Hz. Due to the similarity of the frequencies, these values were not compared against manufacturing characteristics.
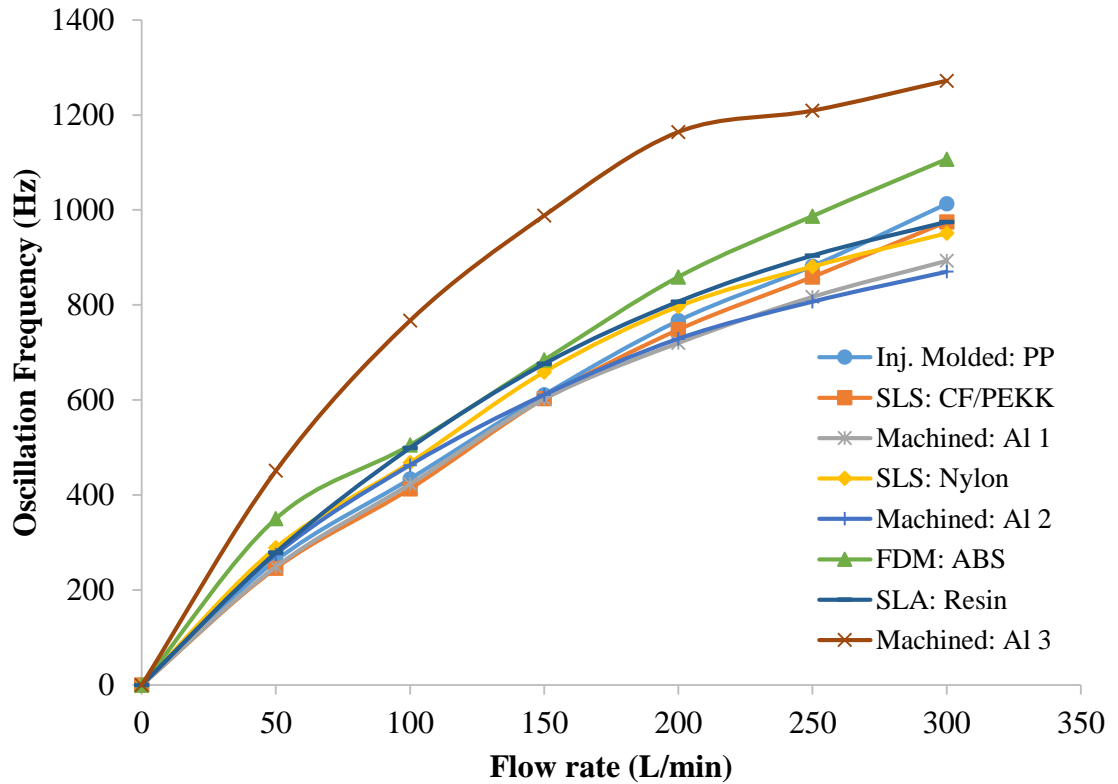
Figure 3.7. Oscillation frequency (Hz) for different inserts

3.3.2 Pressure

Since pressure values were measured upstream of the air inlet, the data should not be affected by the different inserts. Nonetheless, an interesting observation is made. Theoretically, the pressures ought to have remained similar to one another, due to the nominally same cavity design and nozzle width. However, in Figure 3.8, it is clear that Al 2 and Al 3 experienced up to 1.5 times higher pressure than the rest of the inserts. Thus, there may be unknown factors in the experiment.
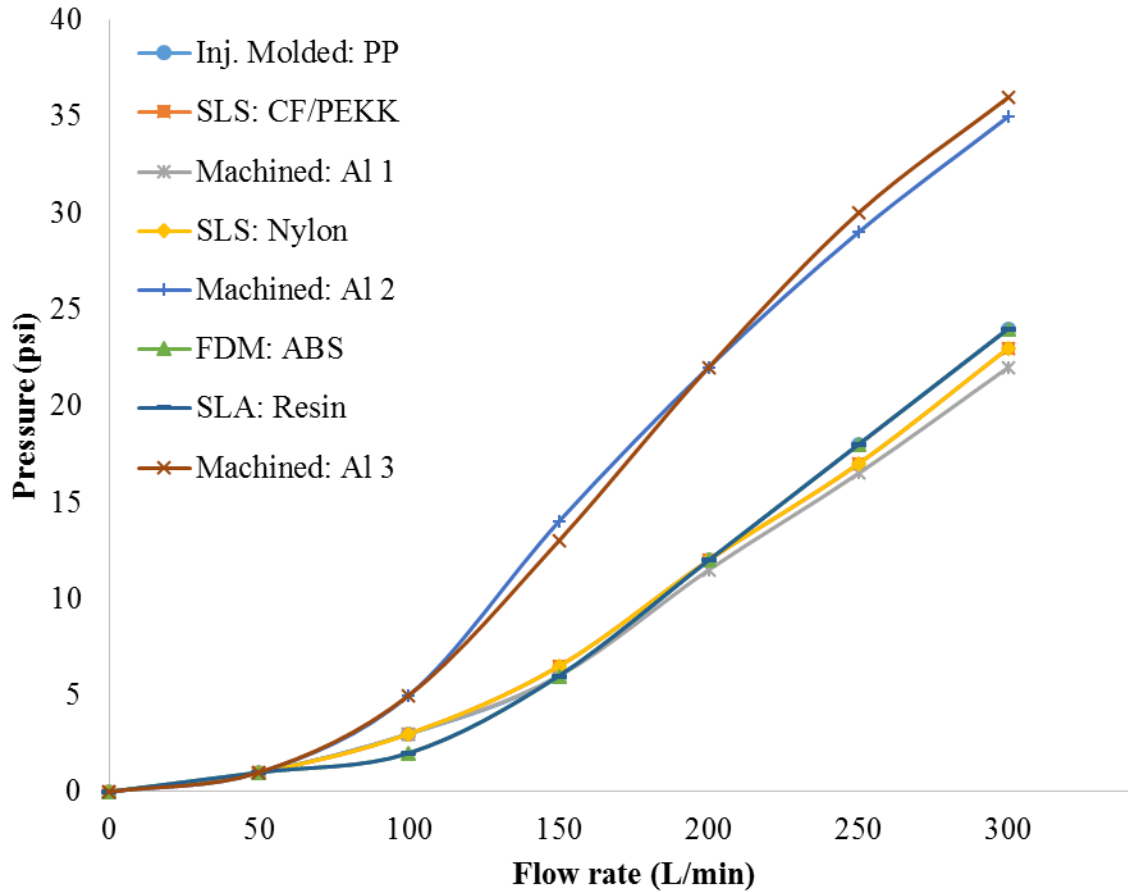
Figure 3.8. Pressure (psi) for different inserts

Both Al 2 and Al 3 were tested with a different test module on different days, with less than 3% difference from nominal dimensions for all dimensions measured. One potential explanation is that blockage within the device increased the pressure. Case in point, the gasket sealing the cover started to pinch inwards towards the open cavity for Al 3, even when the gasket was sealed against the top cover with an adhesive (Figure 3.9). Al 2 also showed a slight pinch, although it was significantly less pronounced than the pinch in Al 3 (Figure 3.9). Other explanations may be due to pressure line losses in the other tests or simply due to the aluminum material used (although Al 1 did not experience higher pressures).
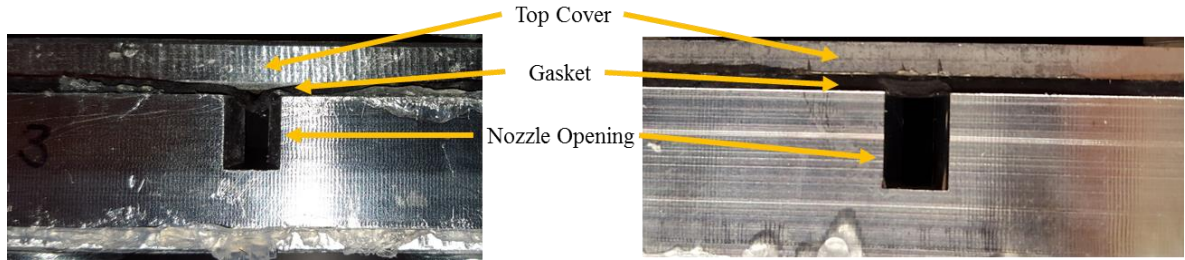
Figure 3.9. Front view of nozzle opening for Al 3 (Left) and Al 2 (Right)

3.3.3 Velocity Profiles for 150 L/min

First, velocity profiles at Q = 150 L/min are examined due to clear features presented by the data for Design 2 (Figure 3.10) and Al 1 and Al 3 (Figure 3.11). From Figure 3.10, the oscillation of the jets of air manifest as two peaks in the velocity profile, as expected. These peaks can be described as symmetrical or asymmetrical about the z = 0 mm axis. Symmetrical peaks demonstrate uniform jet oscillation (e.g., Inj. Molded and SLS: CF/PEKK), whereas asymmetrical peaks demonstrate the jet lingering or favoring one side more than the other, such as for SLS: Nylon or for FDM. Examining these two inserts more closely, SLS: Nylon had visible nicks and residual powder in certain places and overall greater dimensional differences from nominal dimensions. No significant defects were noticed on any of the other inserts. Thus, when correlating manufacturing characteristics with symmetrical performance, the SLS: Nylon insert is assumed to be an outlier. As the hot wire probe measures the velocities further away from the nozzle at x = 8, 15, and 25 mm, the maximum velocities gradually decrease and spread over a wider range.
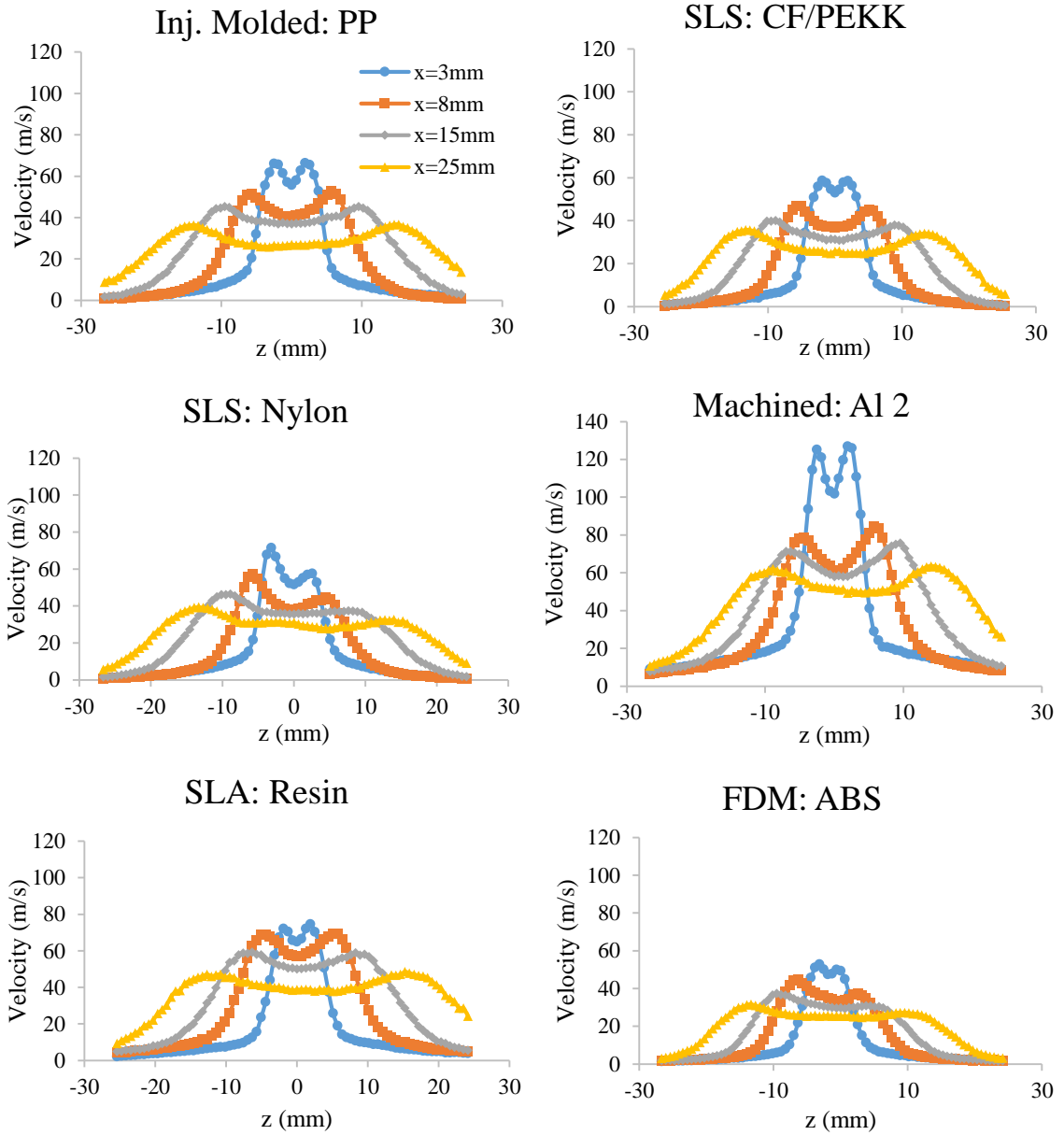
Figure 3.10. Velocity Profiles for Design 2 at 150 L/min

From Figure 3.11, the Al 1 and Al 3 velocity profiles seem to show only a single peak, which would seem to indicate no oscillation. However, jet oscillation with reduced magnitudes of oscillation could explain this phenomena, especially considering that

measured oscillation frequencies validate jet oscillation for each insert[3]. Nonetheless, it is clear that the velocity profiles of Al 2 have two peaks compared to the single velocity profile peaks of Al 1 and Al 3. This demonstrates that the magnitude of oscillation depends on the nozzle wall thickness dimension that was varied and that there may be a lower and upper limit for this dimension. Another feature to note is that, as a result of higher pressure for Al 2 and Al 3, the velocity profiles for Al 2 and Al 3 are also significantly higher than all other velocity profiles at the respective streamwise distances, which may stem from unknown factors mentioned in section 3.3.2.
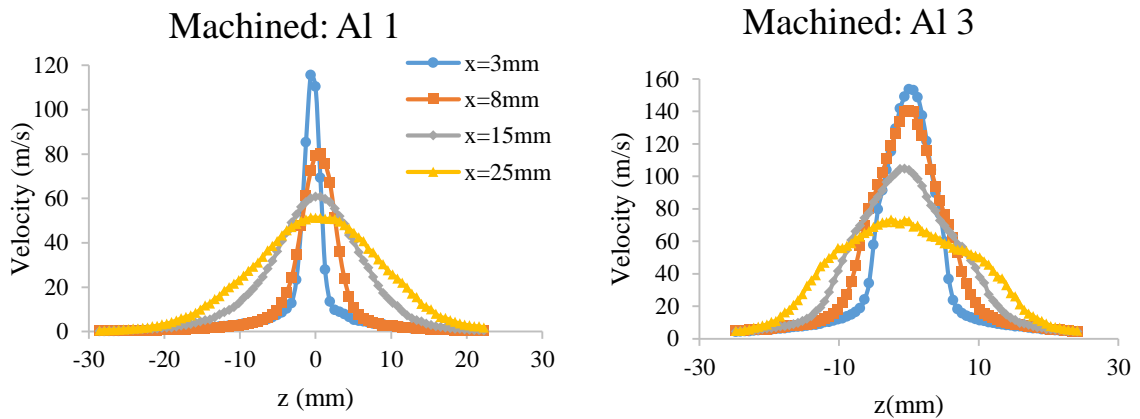
Figure 3.11. Velocity Profiles for Al 1 and Al 3 at 150 L/min

Examining the symmetry of the velocity profiles, there are two methods of characterizing symmetry: jet spread half angle difference, $\theta_{jet\ difference}$, and normalized peak difference. $\theta_{jet\ difference}$ is defined as the difference between the jet spread half angles about the z = 0 mm axis. It is possible to calculate jet spread half angles by plotting the x value against the distance of the peak away from z = 0 mm (Figure 3.12) and then determining the angle the linear regression lines create with the x = 0 axis. Thus,

---

[3] Private Communication with Dr. Michael DeSalvo of Georgia Tech's FMRL

jet spread half angles can be calculated for the left, $\theta_{jet\ left}$, (z < 0 mm) and right, $\theta_{jet\ right}$, (z > 0 mm) sides, shown in Table 3.2. From the values, almost all values are within 16% of the average jet spread half angle, with the injection molded insert maintaining a right jet spread half angle 21% greater than average. Nonetheless, all $\theta_{jet\ difference}$ values are less than a few degrees, demonstrating symmetrical angle of oscillation for almost all manufacturing methods, especially SLS and FDM. Due to the manual alignment of the velocity profiles at different streamwise distances for each insert, however, there may be errors in the calculated half angles.
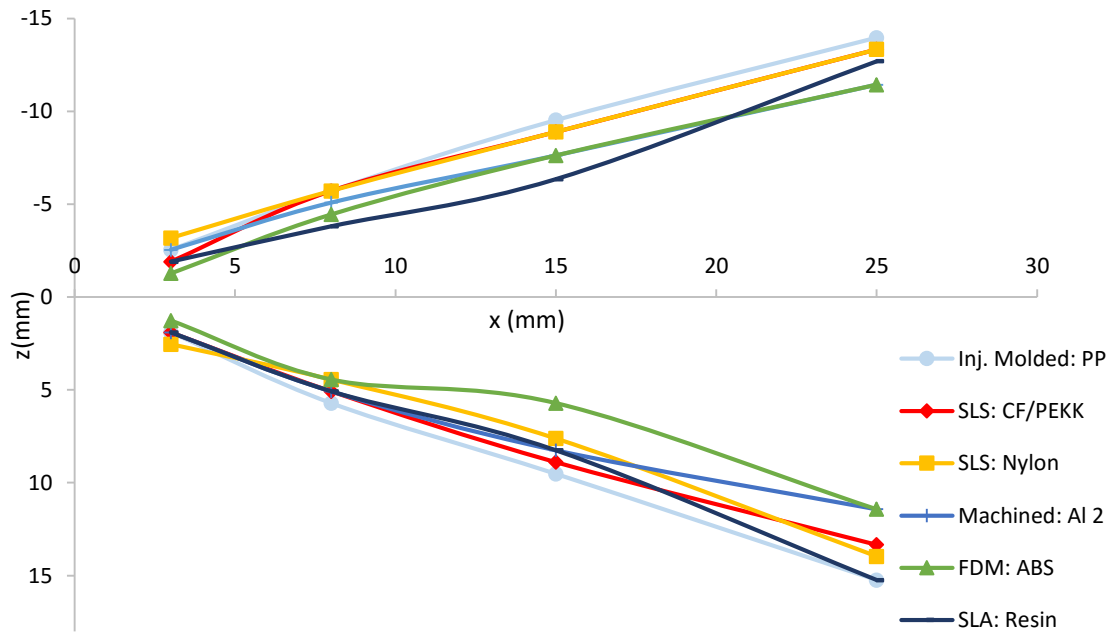
Figure 3.12. Plot of velocity peak locations for jet spread half angles

Table 3.2. Jet spread half angles

Units in Degrees	SLS: CF/PEKK	FDM: ABS	Machined: Al 2	SLA: Resin	SLS: Nylon	Inj. Molded: PP
$\theta_{jet\ left}$	26.8	24.4	21.7	26.0	24.7	27.3
$\theta_{jet\ right}$	27.3	23.6	23.0	23.6	27.6	30.8
$\theta_{jet\ difference}$	0.50	0.75	1.37	2.39	2.90	3.49

The second symmetrical characteristic, normalized peak difference, is calculated from velocity profiles at the distance that gives the highest resolution of oscillation peaks (x = 3 mm). The velocity profiles are divided by the maximum velocities of the respective profile to obtain normalized velocity profiles (Figure 3.13), and the difference between the two normalized peak values for each insert is calculated as the normalized peak difference (Table 3.3). As seen in Figure 3.13, normalized velocity profiles appear very similar, with the exception of SLS: Nylon, which is noted as an outlier earlier due to visible defects. Additionally, the normalized velocity profiles show strong similarities to prior normalized velocity profile data[4] that demonstrate two velocity peaks. Moreover, examination of the peak differences demonstrates that the SLS and injection molded inserts produced very symmetrical oscillation, assuming SLS: Nylon as an outlier, whereas the FDM insert produced a slightly more asymmetrical oscillation (Table 3.3).

---

[4] Private Communication with Dr. Bojan Vukasinovic of Georgia Tech's FMRL
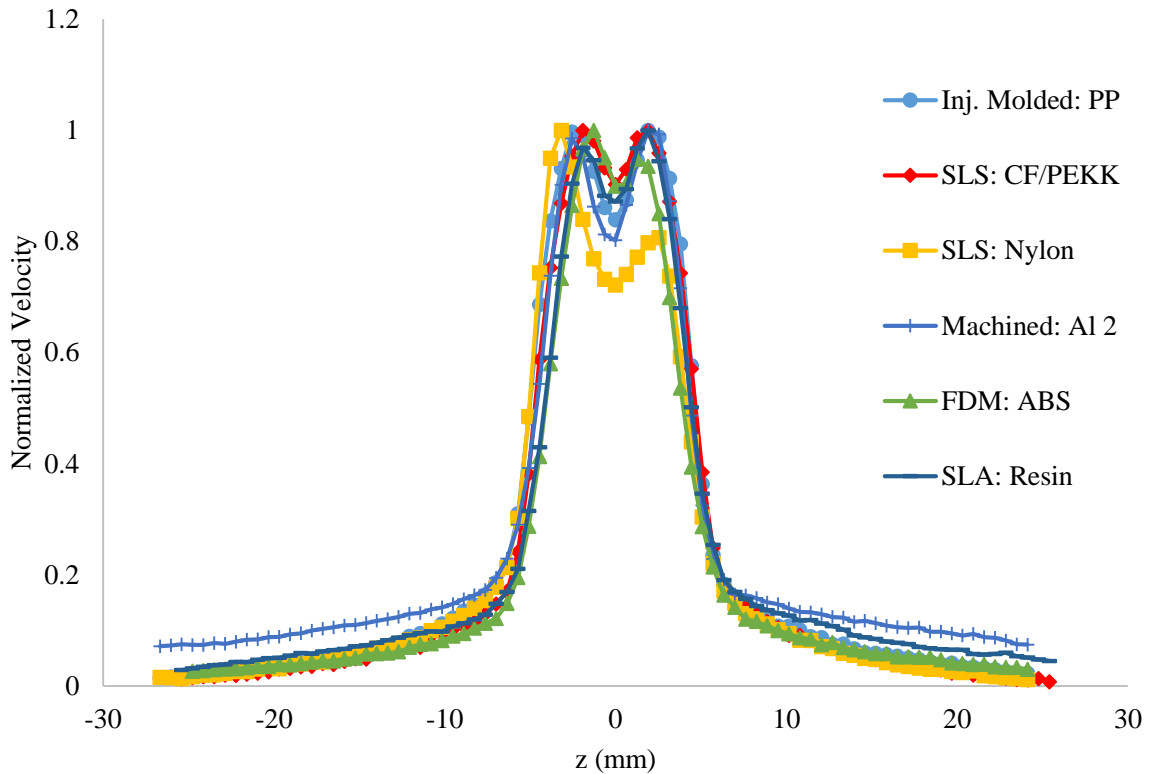
Figure 3.13. Normalized velocity profiles of Design 2 inserts at 150 L/min

Table 3.3. Normalized peak difference

	SLS: CF/PEKK	Inj. Molded: PP	Machined: Al 2	SLA: Resin	FDM: ABS	SLS: Nylon
Normalized Peak Difference	0.001	0.003	0.015	0.031	0.052	0.193

3.3.4 Manufacturing Characterization and Correlation

Symmetry of the insert itself, including dimensional differences between F and G and between H and I, were not correlated due to the differences being an order of magnitude lower than the measured tolerances in almost all cases. Additionally, the surface of the insert in the y direction was not characterized due to the necessary destruction of the insert to obtain surface roughness values and the continued use of the insert for additional testing.

46

Results of surface roughness, manufactured tolerances, and ARs are displayed in

Table 3.4 ordered from least to greatest. Regarding the surface roughness, as expected,

SLA and machined inserts had the lowest surface roughness, validating their use in AFC

research. The injection molded insert, noted as an industrial standard, produced an R_a

value of ~41 microns. In comparison, both SLS manufactured inserts maintain a surface

roughness in-between both standards, whereas the FDM insert has a surface roughness

value more than twice that of the injection molded insert. For the manufactured tolerance,

the SLS and FDM inserts maintain tighter tolerances than the injection molded inserts,

assuming SLS: Nylon as an outlier. Finally, there should not be significant differences in

the measured AR, since they are a result of dimensional changes from the different

manufacturing methods attempting to create the same nominal dimensions. Indeed, all

ARs are within ~17% of the average AR.

Table 3.4. Values of a) Surface Roughness, b) Manufactured Tolerance, and c) Aspect Ratio

a)	SLA: Resin	Machined: Al 1	Machined: Al 2	Machined: Al 3	SLS: CF/PEKK	SLS: Nylon	Inj. Molded: PP	FDM: ABS
R_a (microns)	4.50	7.77	7.85	9.93	12.1	16.8	40.7	95.2

b)	Machined: Al 3	Machined: Al 1	Machined: Al 2	SLA: Resin	SLS: CF/PEKK	FDM: ABS	Inj. Mold: PP	SLS: Nylon
Manufactured Tolerance (+/- in.)	0.003	0.004	0.012	0.015	0.036	0.037	0.038	0.05

c)	SLS: Nylon	AL 1	AL 2	AL 3	SLA: Resin	Injection Molded: PP	FDM: ABS	SLS: CF/PEKK
Aspect Ratio	0.0760	0.0810	0.0813	0.0830	0.0863	0.0888	0.102	0.104

$\theta_{jet\ difference}$ (Figure 3.14) values are plotted against the manufacturing

characteristics for all Design 2 inserts. The corresponding insert for each data point can

be found on the respective charts in Table 3.4. Examining the figures, there is extremely low correlation between surface roughness and $\theta_{jet\ difference}$ (Figure 3.14.a), between manufactured tolerance and $\theta_{jet\ difference}$ (Figure 3.14.b), and between AR and $\theta_{jet\ difference}$ (Figure 3.14.c). As mentioned in section 3.3.3, SLS: Nylon was assumed an outlier for comparisons.
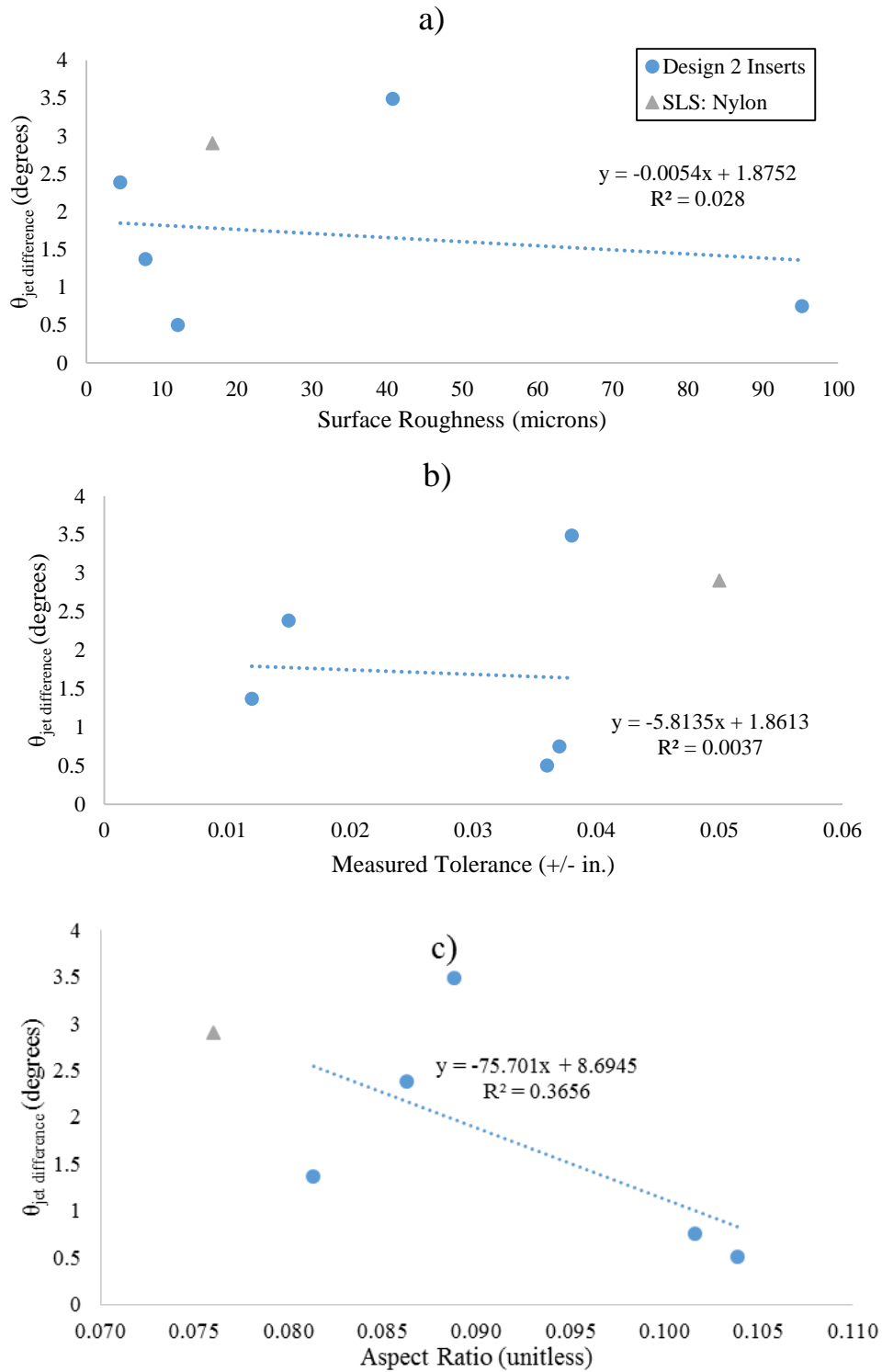
Figure 3.14. a) Surface Roughness, b) Manufactured Tolerance, and c) Aspect Ratio vs. $\theta_{jet\ difference}$

Plotting normalized peak difference against manufacturing characteristics (Figure 3.15), there appears to be little to no correlation between surface roughness and normalized peak difference (Figure 3.15.a) measured tolerance and normalized peak difference (Figure 3.15.b) and between AR and normalized peak difference (Figure 3.15.c). Finally, examining the relationship between $\theta_{jet\ difference}$ and normalized peak difference, there appears to be no dependence of one symmetric characteristic to the other and vice versa (Figure 3.16).
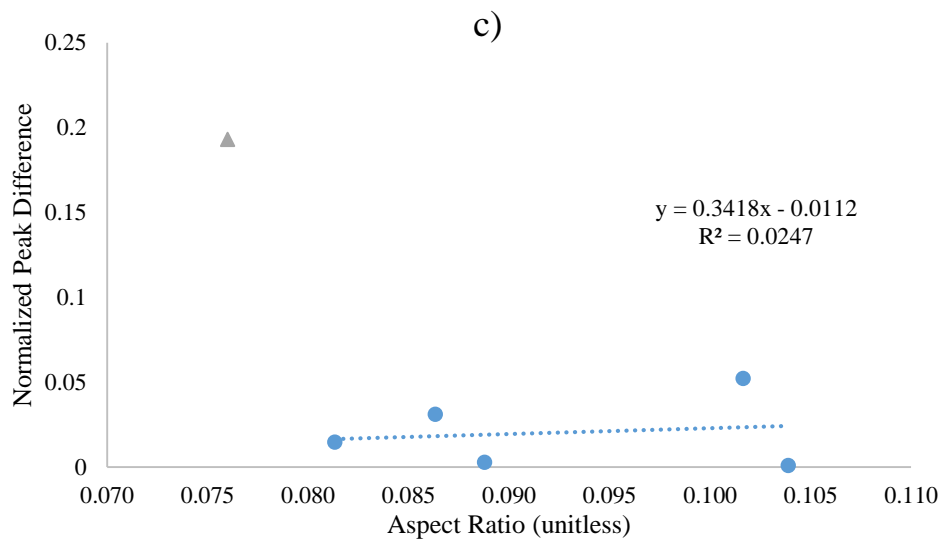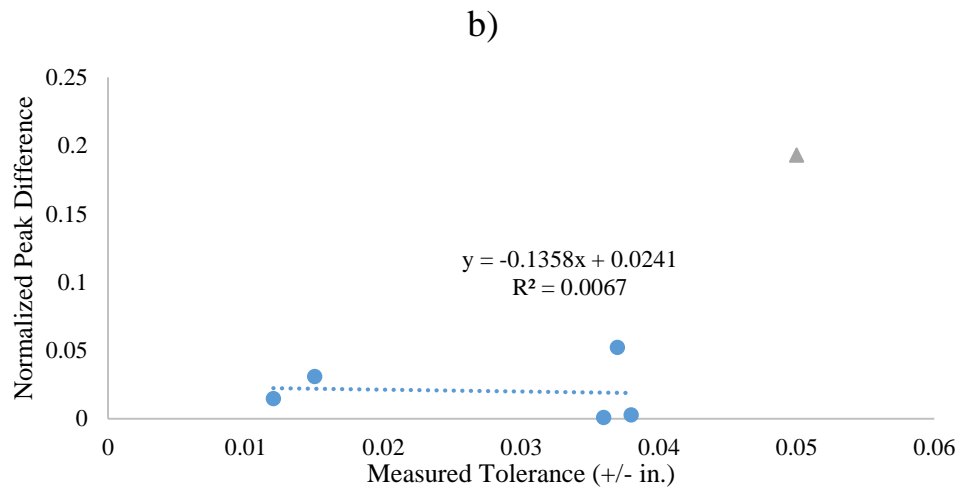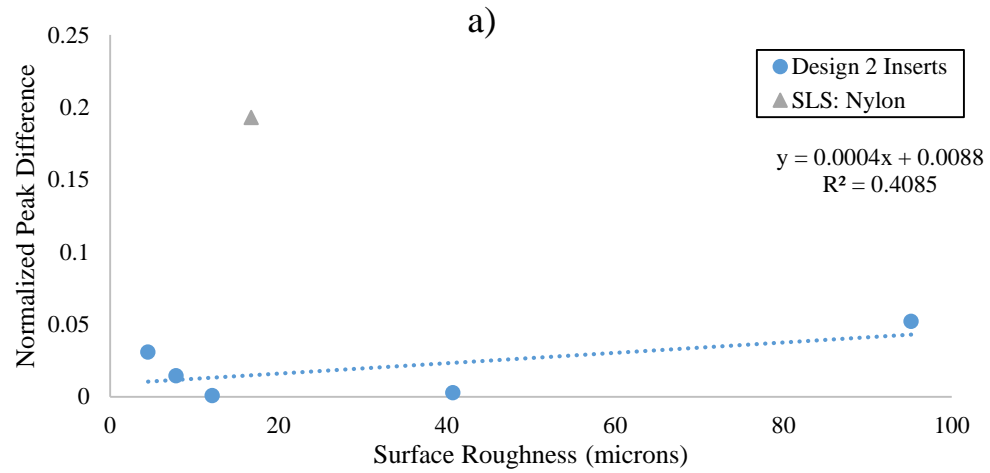
Figure 3.15. a) Surface Roughness, b) Manufactured Tolerance, and c) Aspect Ratio vs. Normalized Peak Difference
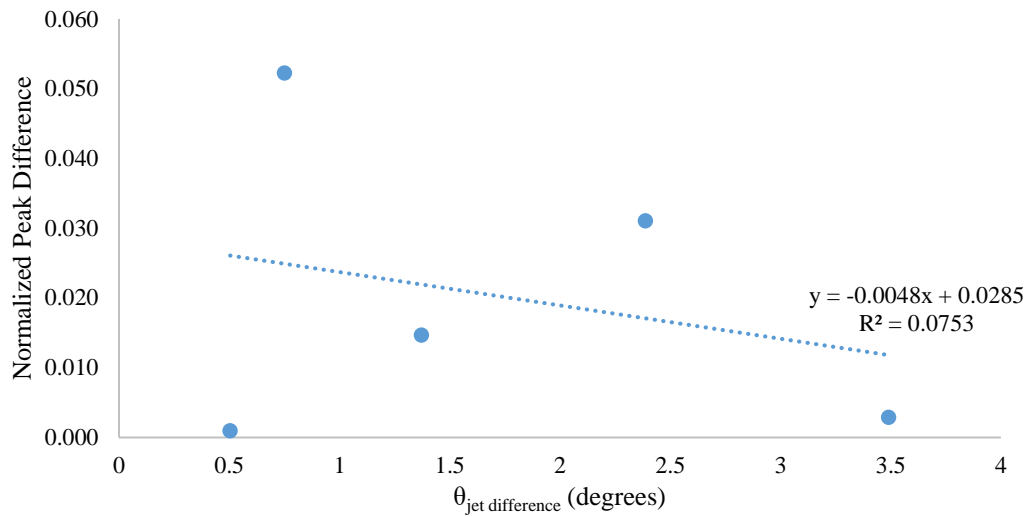
Figure 3.16. Relationship between symmetry characteristics

Without knowing the importance of symmetrical oscillation or the level of symmetry desired for fluidic oscillation and understanding that a small sample size of each insert was tested, these correlation results may not precisely describe manufacturing effects on air flow performance. Thus, further experimentation should be conducted that intentionally varies different features (e.g., sharpness of corners, AR, nozzle wall thickness, surface roughness), which can result in more accurately determining acceptable surface finishes and dimensional tolerances for each feature.

Nonetheless, from a firsthand examination, manufacturing characteristics of SLS and FDM inserts fell in-between both standards, with the exception of the FDM insert having a surface roughness of more than twice that of the injection molded insert. The AR, considered a result of dimensional changes from the manufacturing method, was higher for both SLS and FDM inserts. However, the AR or any other critical dimension should be easily constrained by tightening manufacturing tolerances. Moreover, despite the manufacturing and symmetric differences, when the performance of SLS and FDM inserts are compared to inserts produced by an industry standard (injection molding) and

research standards (machining and SLA), all inserts produced oscillations with two velocity peaks.

3.3.5 Velocity Profiles for 50 L/min and 300 L/min

Data at Q = 50 L/min and Q = 300 L/min are presented in Figures 3.17 and 3.18 for all Design 2 inserts and in Figure 3.19 for Al 1 and Al 2. Inj. Molded at 300 L/min, FDM at 50 L/min, and SLA at 50 L/min velocity profiles are characterized as "noisy" compared to the other smoother charts. The reason for the noise could be due to bi-stable (switching) behavior of oscillation frequencies[5]. This behavior was audible during testing of FDM and SLA inserts at lower flow rates and then disappeared at higher flow rates.

---

[5] Private communication with Dr. Michael DeSalvo of Georgia Tech's FMRL
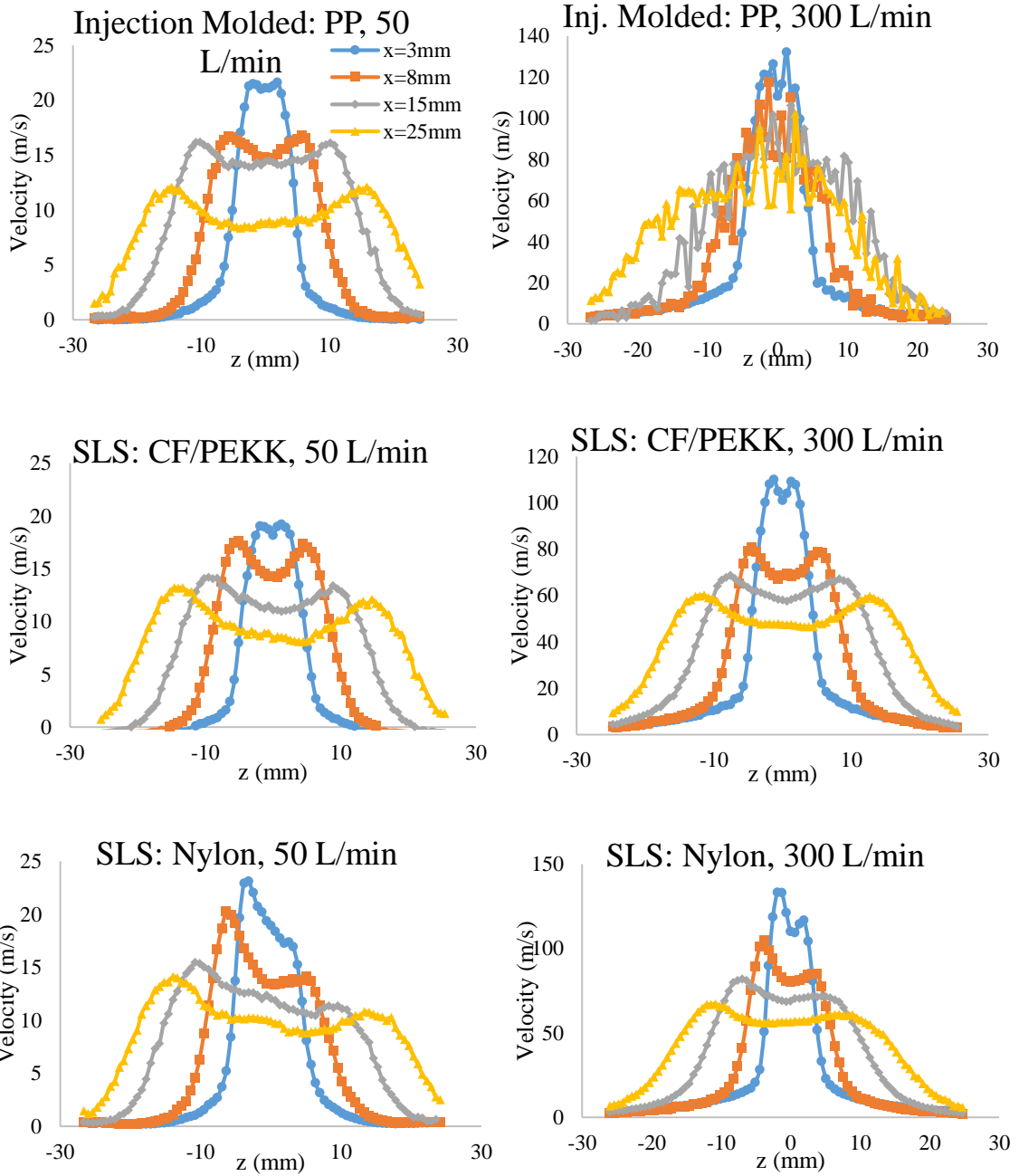
Figure 3.17. Inj. Molded: PP, SLS: CF/PEKK, and SLS: Nylon at 50 L/min and 300 L/min
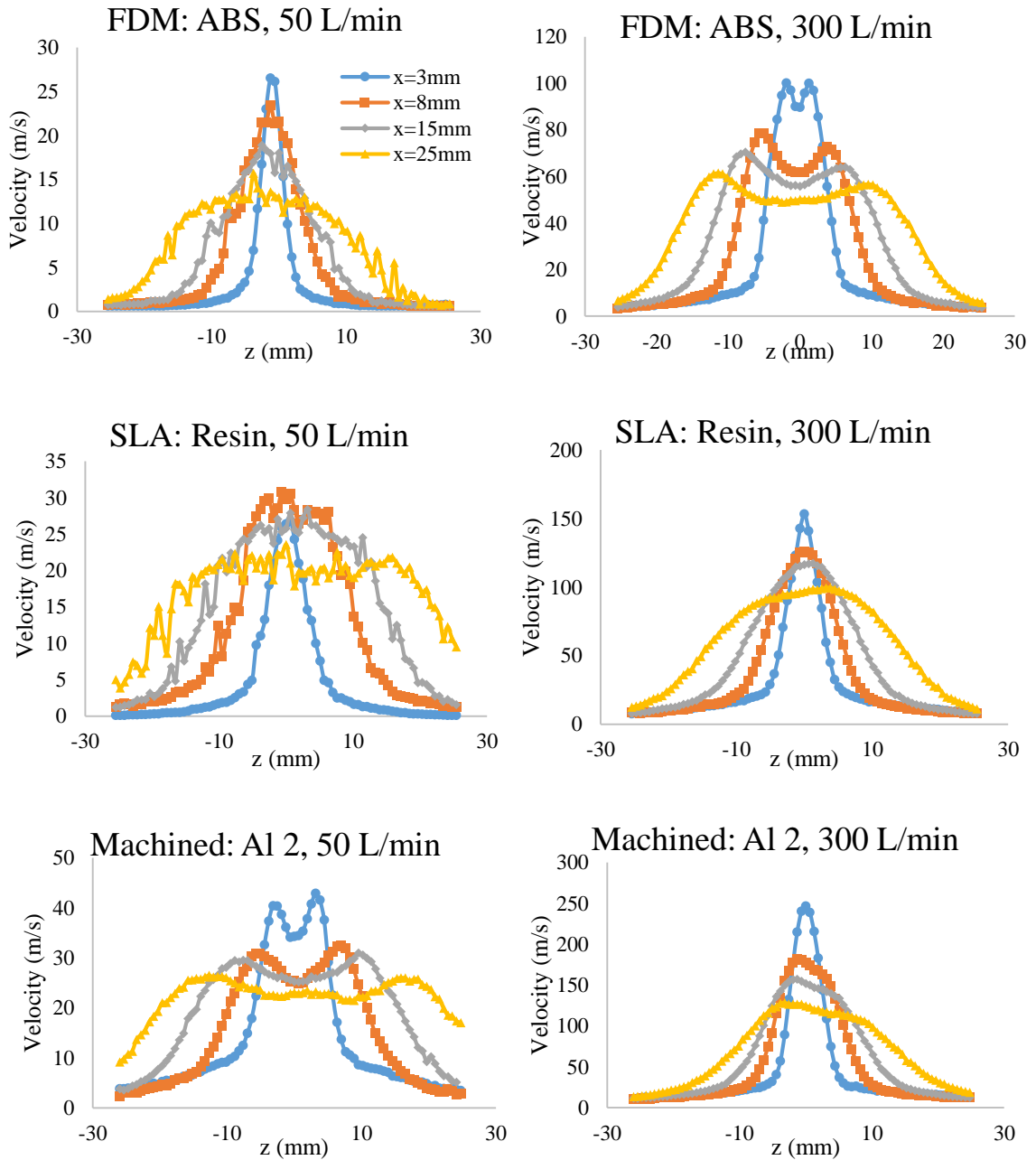
Figure 3.18. FDM: ABS, SLA: Resin, and Machined: Al 2 at 50 L/min and 300 L/min
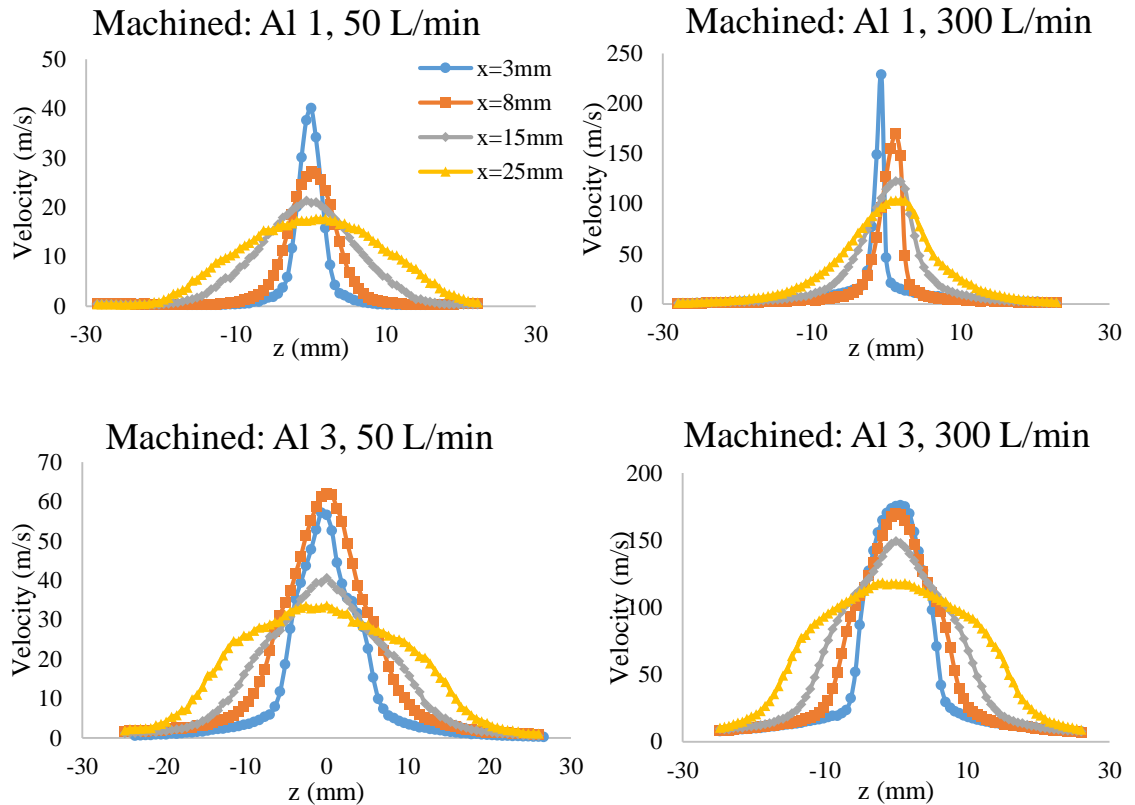
Figure 3.19. Al 1 and Al 2 at 50 L/min and 300 L/min

Another trend to note is that smooth velocity profiles with single peaks were seen at Q = 300 L/min for SLA and Al 2 (Figure 3.18), whereas they demonstrated double peaks at Q = 150 L/min (Figure 3.10). Additionally, it is known that higher flow rate will reduce the wall attachment effect[6]. This suggests that there are potential limits for the flow rate to produce certain oscillations. Finally, some odd characteristics to note include:

1. The jet for Al 1 at 300 L/min starts to lean towards the right.

2. The maximum velocity is higher at x = 8 mm than at x = 3 mm for Al 3 at 50 L/min.

---

[6] Private Communication with Dr. Michael DeSalvo of Georgia Tech's FMRL

The former seems to be a result of an unknown factor allowing the jet to favor the right side at a higher flow rate; the latter might be a result of the pinched gasket, as discussed in section 3.3.2, or other unknown factor altering the flow in 3D.

Smoothing the noisy data with the Savitzky-Golay method (Orfanidis 1996) at 2 degrees (Figure 3.20) seems to result in double peaks for the Inj. Molded at 300 L/min and single peaks for both FDM and SLA at 50 L/min. It is not known whether the low flow rate or other unknown factor(s) contribute to the single peaks seen in the smoothed results.
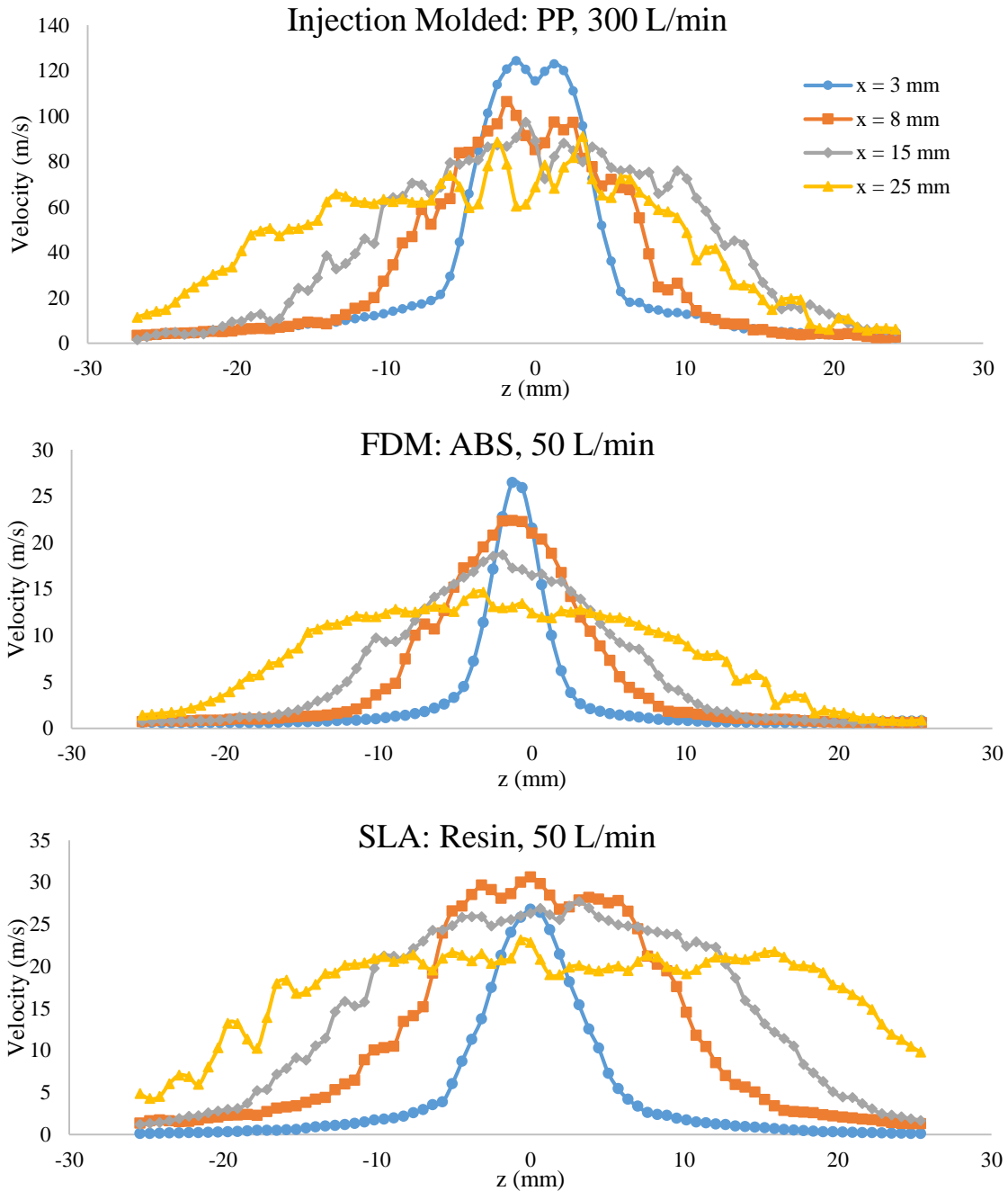
Figure 3.20. Smoothed velocity profiles for Inj. Molded, FDM, and SLA at respective flow rates

3.4 Chapter Summary

Experiments were conducted to compare performances of fluidic oscillators that were manufactured with different methods. These methods included previously untested

FDM and SLS, machining and SLA as research standards, and injection molding as an industry standard. Surface roughness, manufactured tolerance, and AR were measurements obtained from the inserts to characterize manufacturing method. To characterize air flow, pressure, oscillation frequency, and velocity profiles were measured. Examining the velocity profiles, two methods of characterizing symmetry were determined: jet spread half angle difference, $\theta_{jet\ difference}$, and normalized peak difference.

All oscillation frequencies measured were determined to be in the range of expected frequencies for nominal dimensions of Design 2[7]. Pressure measurements revealed that unknown factors may have affected the air flow of the experiments. Nonetheless, from normalized velocity profiles, all Design 2 inserts were determined to successfully oscillate with two velocity peaks at Q = 150 L/min, which validates the use of FDM and SLS as potential manufacturing methods for fluidic oscillators. Moreover, the normalized velocity profiles demonstrated strong similarities to prior normalized velocity profile data with two velocity peaks[8], validating the manufactured characteristics of SLS and FDM inserts.

Examining the manufactured characteristics further, surface roughness and geometric tolerance measurements of FDM and SLS inserts remained in-between the respective values of the industry standard and the research standards, with the exception of the FDM insert's surface roughness being more than twice that of the injection molded insert. On the other hand, both the SLS and FDM inserts' AR were greater than that of all other inserts. However, all ARs were deemed to be relatively similar to each other.

---

[7] Private Communication with Dr. Michael DeSalvo of Georgia Tech's FMRL
[8] Private Communication with Dr. Bojan Vukasinovic of Georgia Tech's FMRL

Correlating the three manufacturing characteristics against the two symmetric characterizations of the velocity profiles, very little to no correlation appear. In light of these results, the importance of symmetrical oscillation or the level of symmetry necessary for fluidic oscillation is not known. Thus, further experimentation should be conducted that intentionally varies different features, which can result in more accurately determining acceptable surface finishes and dimensional tolerances for each feature. Symmetry of the insert itself and characteristics of the insert in the y axis were not correlated, for reasons mentioned earlier, and may be regarded as additional factors to test for the symmetry of the jet oscillations.

Finally, examining velocity profiles at $Q = 50$ and 300 L/min, aberrations such as single peaks, noisy data, and higher than average pressures and velocities occurred for some inserts, demonstrating that flow rate may have upper and lower limits in producing jet oscillation with two velocity peaks. Similarly, the nozzle wall thickness, defined as dimensions F and G (Figure 3.3), may also have an upper and lower limit in ensuring jet oscillation with two velocity peaks at $Q = 150$ L/min.

CHAPTER 4

DESIGN OVERVIEW

In order to design a robust solution for the main objective, proper design procedures should be followed, accompanied with knowledge of the design space and relevant, supporting research. Thus, in this chapter, the selected design methodologies will be presented, followed by constraints that define the design space. Relevant topics regarding composite holes and joining techniques will be briefly reviewed to inform design options. Finally, initial results of the design methodologies will be presented for further expansion in the following chapter.

4.1 Design Methodologies

There is an engineering design adage that asserts "design decisions determine 70% or more of product costs" (Barton 2001). Whether or not this value is realized, surveys reveal that, with proper design methodology, not only is a reduction in part cost/count desired but also time-to-market improvements, quality and reliability improvements, and reduction in manufacturing cycle time and assembly time (Boothroyd et al. 2002). Thus, for this project, two main design methodologies will be utilized: Axiomatic Design (AD) and Design for Manufacturing and Assembly (DFMA). The former is chosen to logically define the requirements and resulting designs, whereas the latter is chosen to supplement the design decisions by taking manufacturing and assembly processes into account. Once viable conceptual designs have been generated, they will be evaluated with decision matrices based on the aforementioned categories of component cost, weight, manufacturing process, and assembly process. These evaluation categories are a result of discussions within this research group and with Boeing representatives. Thus, AD, DFMA, and the evaluation technique will be discussed in this section.

AD is unique in its framework in that it is based on "the abstraction of good design decisions and processes" (Suh 2001) compared to other algorithmic approaches. The framework consists of four domains, labeled the customer domain, functional domain, physical domain, and process domain. The customer domain represents the customer needs or attributes (CAs); the functional domain converts the needs into a set of functional requirements (FRs) and a set of constraints (Cs) that preside over the physical and process domains; the physical domain satisfies the FRs with design parameters (DPs); the process domain produces the product specified by each of the DPs through process variables (PVs) (Figure 4.1).
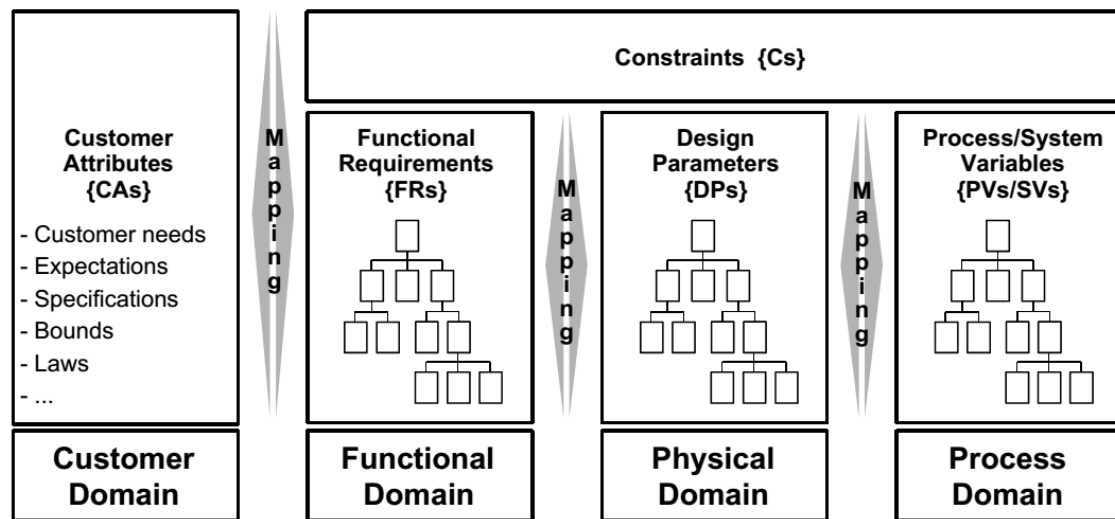
Figure 4.1. AD domains (Cochran et al. 2000)

The relationship between the customer and functional domains organizes desired attributes into a set of product requirements. Between the other domains are a series of back-and-forth, zigzag mappings that go from *what* needs to be accomplished to *how* it can be accomplished. The zigzag mapping technique is mandatory for relationships between the FRs and DPs and applicable for relationships between the DPs and PVs.

Furthermore, mapping is an iterative process that strives to meet two axioms (self-evident truths for which there are no exceptions): Independence Axiom and Information Axiom. The Independence Axiom states that independence of the FRs should be maintained. This can be achieved by examining the relationship between FRs and DPs in matrix form

$$\{FR\} = [A]\{DP\} \tag{4.1}$$

where [A] is the design matrix that characterizes the relationships between each DP to each FR.

$$[A] = \begin{bmatrix} A_{11} & A_{12} & A_{13} \\ A_{21} & A_{22} & A_{23} \\ A_{31} & A_{32} & A_{33} \end{bmatrix} \tag{4.2}$$

To fulfill the Independence Axiom, the design matrix should be a diagonal matrix (uncoupled) or an upper or lower triangular matrix (decoupled), showing no dependence in the former or limited dependence in the latter. The relationship between DPs and PVs can be shown in a similar manner where

$$\{DP\} = [B]\{PV\} \tag{4.3}$$

and

$$[B] = \begin{bmatrix} B_{11} & B_{12} & B_{13} \\ B_{21} & B_{22} & B_{23} \\ B_{31} & B_{32} & B_{33} \end{bmatrix} \tag{4.4}$$

The Information Axiom states that the information content should be minimized, and is useful in selecting the best design that satisfies the FRs among a group of acceptable designs. Information content, I_i, is defined in terms of the probability of satisfying FRs, P_i

$$I_i = \log_2 \frac{1}{P_i} \tag{4.5}$$

The total information content of the system, I_{sys}, is summed up differently for an uncoupled system, where all FRs are statistically independent

$$I_{sys} = \sum_{i=1}^{m} I_i = -\sum_{i=1}^{m} \log_2 P_i \tag{4.6}$$

than a decoupled system, where all FRs are not statistically independent

$$I_{sys} = -\sum_{i=1}^{m} \log_2 P_{i|\{j\}} \qquad\qquad \{j\} = \{1,2,\dots,i-1\} \qquad\qquad (4.7)$$

The probability of success can be defined through a natural or an inherent function of the problem, such as when fewer parts or larger tolerances decrease the complexity, thus increasing the probability of success. Alternatively, the probability of success can be defined by the intersection of the design range set by the designer that satisfies the FRs and the system ranges generated by each specific design, which is a more methodical but tedious process.

While there are many benefits to using AD, especially in helping designers objectively think about the solution, there are also some disadvantages, as found through multiple interviews with different companies by Alavizadeh and Jetley (2010). The results of the study showed that AD "is recommended to be used along with other methodologies," such as Robust Design (Alavizadeh and Jetley 2010). Indeed, Suh (2001) notes that by providing axioms, constraints are set up for further algorithmic approaches, such as design for assembly and design for manufacturability. Thus, in this project, instead of calculating the probability of success, DFMA will be implemented as a means to reduce the information content while guiding the design process itself as a PV.

4.1.2 Design for Manufacturing and Assembly

With DFMA, "to manufacture" is defined as "the manufacturing of the individual components parts of a product or assembly," and "to assemble" is defined as "the addition or joining of parts to form the completed product" (Boothroyd et al. 2002). A powerful tool for design teams in the industry, DFMA consists of a process of following general guidelines to achieve a "best design concept" (BDC) for production purposes (Figure 4.2). Although there are a few variations of DFMA used by various groups and companies, the characteristic guidelines set out by Boothroyd et al. (2002) will be observed.
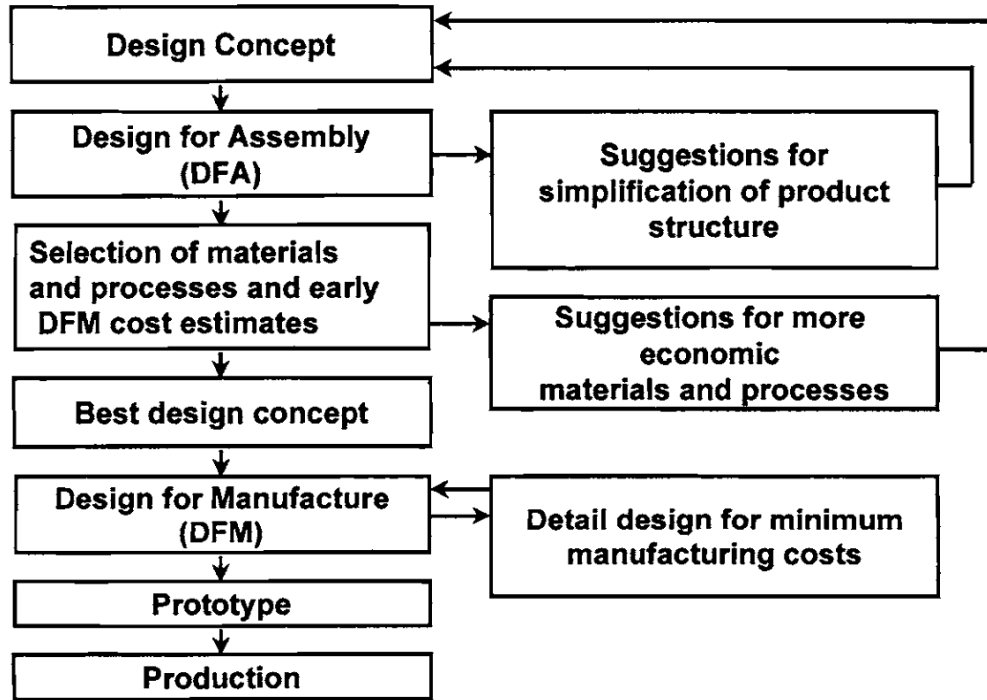
Figure 4.2. DFMA steps (Boothroyd et al. 2002)

At the beginning of Design for Assembly (DFA), it is important to select the type of assembly method, with non-mutually exclusive choices of manual, automatic, and robotic methods. One factor that aids in this decision is the production volume, where the cost of the method is proportional to the benefit gained from production. For low production volume (<1000 parts per year), manual assembly is recommended; for high production volume (> 1 million parts per year), high-speed automated assembly is recommended (Joneja 2010). In between these limits, there can be a combination of assembly methods that also incorporates robotic assembly (Joneja 2010). While there are certain guidelines associated with each method, guidelines set out for manual assembly will be covered first, since most of them can be applied to automatic and robotic assembly methods as well.

In general, there are two main factors that influence the manual assembly cost of a product: the number of parts and the ease of handling, insertion, and fastening of those parts. First, three criteria are applied to each part to reduce the part count:

1. During product operation, does the part move relative to all other parts?

2. Must the part be of a different material than or be isolated from all other parts?

3. Must the part be separate from all other parts because otherwise necessary assembly or disassembly of other parts would be impossible?

Additionally, design guidelines for the minimum part criteria (Figure 4.3) include the following:

1. Avoid connections

2. Design for unrestricted assembly access

3. Avoid adjustments

4. Utilize kinematic design principles
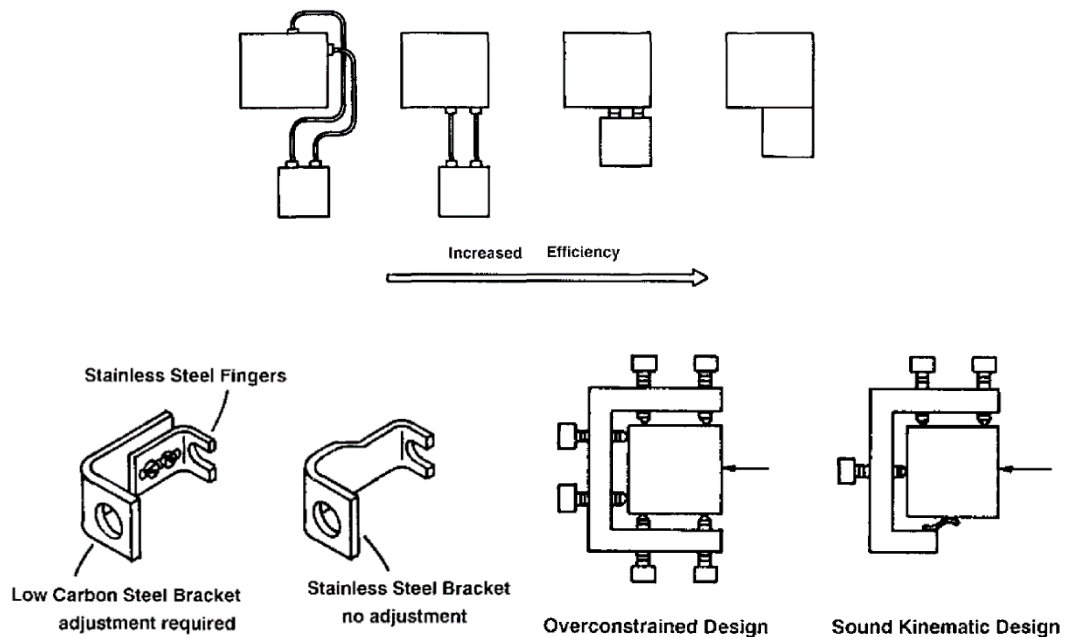
Figure 4.3. Geometric features critical to part count (Boothroyd et al. 2002)

Next, a list of guidelines that address the second source of cost are naturally divided into two areas – "handling (acquiring, orienting and moving the parts) and insertion and fastening (mating a part to another part or group of parts)" (Boothroyd et al. 2002). Specifically meant for manual assembly, as opposed to robotic and automatic assembly, these guidelines can also apply to the other forms of assembly. For part handling, parts ought to

1. Maximize symmetry or asymmetry

2. Avoid jamming or tangling features

3. Avoid parts that stick or are slippery, delicate, flexible, very small, very large, or hazardous (Figure 4.4).
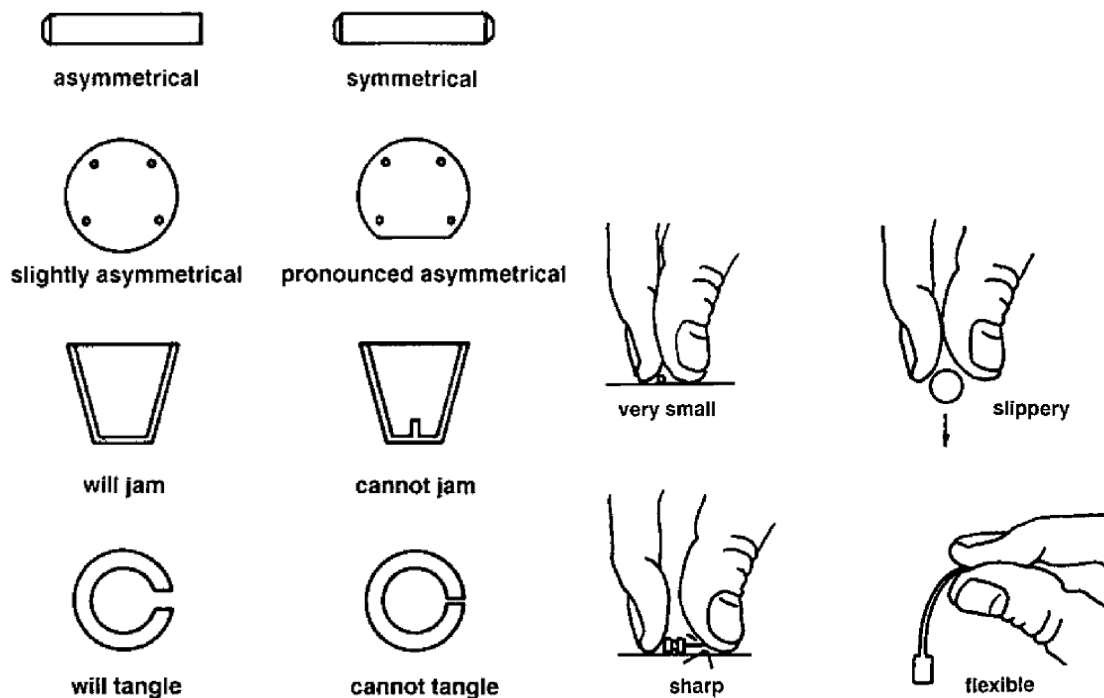
Figure 4.4. Geometrical features critical to part handling (Boothroyd et al. 2002)

For insertion and fastening, parts should

1. Maintain low resistance and proper guidance (e.g., use of radii and chamfers) to insertion while reducing the tendency to jam

67

2. Be standardized with common parts, processes, and methods

3. Utilize a pyramid assembly

4. Avoid a holding force during subassembly manipulation

5. Be located before release

6. Utilize a low fastener cost, ranked in Figure 4.5 least to greatest (snap fit, thermal staking, rivet, screw fastener)

7. Avoid repositioning
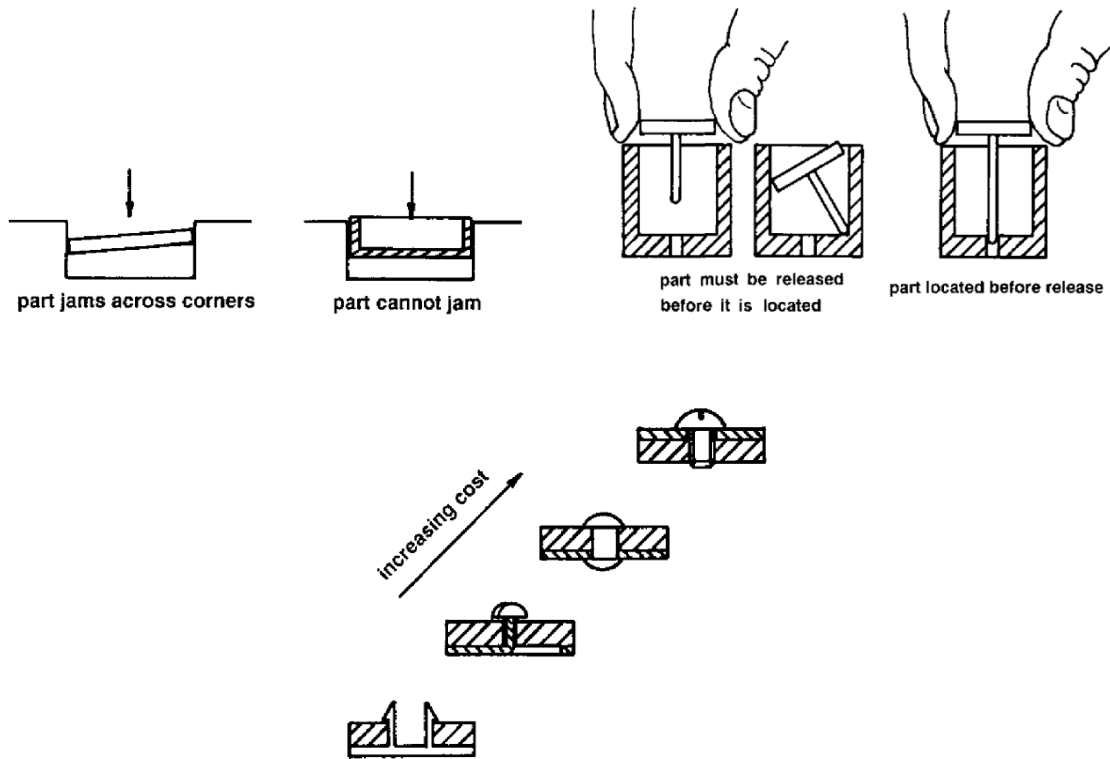
Figure 4.5. Geometrical features critical to insertion and fastening (Boothroyd et al. 2002)

With these design changes, the assembly efficiency of designs can be compared through the efficiency index, E_{ma}.

$$E_{ma} = \frac{N_{min} t_a}{t_{ma}}$$

(4.8)

where N_{min} is the theoretical minimum number of parts, t_a is the time to acquire a tool for one part, and t_{ma} is the estimated time to complete the assembly of the product. The time to acquire a tool for a part without handling, insertion, or fastening issues is about 3 seconds. Further discussion of the different factors affecting assembly time shall be conducted in Chapter 6 and Appendix B.

For robotic and high-speed automatic assembly, the only notable design guideline additions are made in light of high-speed feeding and orienting. This includes features that prevent overlapping, sticking, abrasion, or flight off a conveyer system, features that enable gripping in an easily detectable orientation, and potential designs for a "work carrier" to easily carry and assemble complex parts.

Returning to Figure 4.2, the next step is the selection of materials and manufacturing process. Depending on the general ranges of properties required, early material decision making can result in anywhere from a group of applicable materials to a specific material dimensionally ranked as the best with respect to specific properties. For the manufacturing process selection, there are three stages of processing: primary (main shape), primary/secondary (main shape, form or refine features), and tertiary (finishing processes). At each stage, there are multiple manufacturing processes, each of which has a range of producible capabilities. Required properties, such as shape features, tolerance, surface roughness, and material type, can help select an optimal process.

Once the above steps have been cycled through, it is imperative that the product be designed for the selected manufacturing process(es). Thus, variables such as material weight, tooling, and the product itself can be better optimized for the manufacturing procedure. With the new design, a prototype can finally be produced, tested, and redesigned, allowing for future cycles of DFMA.

<u>4.1.3 Evaluation Technique</u>

Once designs have been optimized, there still remains the process of comparing discrete designs to select a final design. To accomplish this, Boothroyd et al. have reduced the relations between product design, manufacturing operations, and assembly method to a single decision factor: cost (Joneja 2010). First order cost estimates will be conducted through material, manufacturing and assembly process, and weight costs. Material cost will include any additional component cost not manufactured "in-house." The selected manufacturing process cost will include the capital and recurring costs critical to the particular manufacturing process; the assembly cost, C_{asm}, will be calculated as follows:

$$C_{asm} = t_{ma} * C_{ind,asm} \left[\frac{USD}{part}\right] \tag{4.9}$$

where t_{ma} is equal to the estimated time to complete the assembly from Eq. (4.8) and $C_{ind,asm}$ is equal to the average indirect cost per hour. The weight cost will simply be the weight of the proposed design. Not included in this cost estimate are the capital costs required to purchase the manufacturing equipment.

4.2 Problem Definition

Through integrating fluidic oscillators into the trailing edge (TE) composite flap structure, constraints of the project that fall under the C category of AD mentioned in section 4.1.1 are set out here. These constraints can be divided into two categories: Flap Structure and Fluidic Oscillator. Additionally, constraints will be referenced throughout the remainder of the thesis by the section number followed by the constraint number (e.g., Constraint 4.2.2.8 represents the fluidic oscillator constraint of having a device located every 6 inches).

4.2.1 Flap Structure Constraints

On the TE flap, there are three areas of interest for AFC device integration. The location this project focuses on, as mentioned in chapter 1, is the composite bullnose at the leading edge (LE), deemed a secondary structure[9]. Three structures of importance at the LE of the flap are the fiberglass bullnose, carbon fiber reinforced polymer (CFRP) laminate C-channel spar, and fiberglass splice straps that hold the first two structures together. Further details include the following constraints:

1. Bullnose is ~0.12 in. thick fiberglass composite and does not provide structural support[9].

2. Front, carbon fiber composite spar location is ~5-6% chord and provides structural support[9].

3. Front spar shall support the AFC device[9].

4. Front spar has access holes with which to pass items/objects through[9].

5. The wing tip can experience anywhere from -1 to 9 g's[9].

6. Inboard ailerons withstand temperatures from -65 °F to 180°F (Mallick 1993)

4.2.2 Fluidic Oscillator Constraints

Regarding the fluidic oscillator, the desired attributes of the oscillator are listed in this section. It is important to note that even though the type of fluidic oscillator is set as a constraint, the oscillator can be replaced by almost any other AFC device, given the appropriate design attributes required to allow efficient operation.

1. Fluidic oscillator is 6 times[10] the size of the oscillator[9] used by DeSalvo et al. (2011).

---

[9] Private communication with Boeing
[10] Private communication with Prof. Ari Glezer of Fluid Mechanics Research Laboratory (FMRL) at Georgia Institute of Technology (Georgia Tech)

2. Material of the device shall be carbon fiber reinforced polyetherketoneketone (PEKK) due to specific properties that include high strength, high glass transition temperature, T_g, excellent fire, safety, and toxicity (FST) properties, excellent ultraviolet (UV) resistance, and compatibility with composite structures[9].

3. Device shall have a maximum angle of 30° with respect to the airfoil tangent[11].

4. Air supply pressure is 30 ± 5 psi[9].

5. Air supply temperature is 50 ± 30 °F for all flight conditions[9].

6. Air supply ducts shall have ¾ in.[2] cross-sectional area, any shape, for each actuator[9].

7. Plenum and horseshoe section shall be as flat as possible on a radius larger than 1000 in. [9].

8. Pitch of the device is every ~6 in. [9].

9. Device shall be removable in the case of maintenance, repair, and replacement[9].

4.3 Relevant Topics

From the design methodologies described and the constraints listed above, two topics of importance surface: composite hole creation and joining methods. The former arises due to the need for the oscillating air to pass from the actuator, through the composite bullnose skin, and out into freestream and due to the need for the actuator to be securely fastened onto the front composite spar. The latter arises due to, again, the need for the actuator to be securely fastened. In this section, issues and solutions regarding these topics will be discussed.

---

[11] Private Communication with Dr. Michael DeSalvo of Georgia Tech's FMRL

4.3.1 Composite Holes

      As with all manufacturing methods, defects occur when creating holes in composites after they have been fabricated, such as burrs, matrix burnout, fiber pullout, and delamination (Figure 4.6). Specifically, delamination is a critical type of defect to reduce or eliminate because it "drastically reduces assembly tolerance and strength against fatigue, thus degrading the long-term performance of composites" (Won and Dharan, 2002). In fact, in aircraft industries, the rejection of all composite parts made due to delamination defects during final assembly was as high as 60% (Stone and Krishnamurthy, 1996). Therefore, this section will examine methods to reduce defects, which will not only increase performance but also significantly improve manufacturing and assembly of composite parts.

a)   **b)**   **c)**
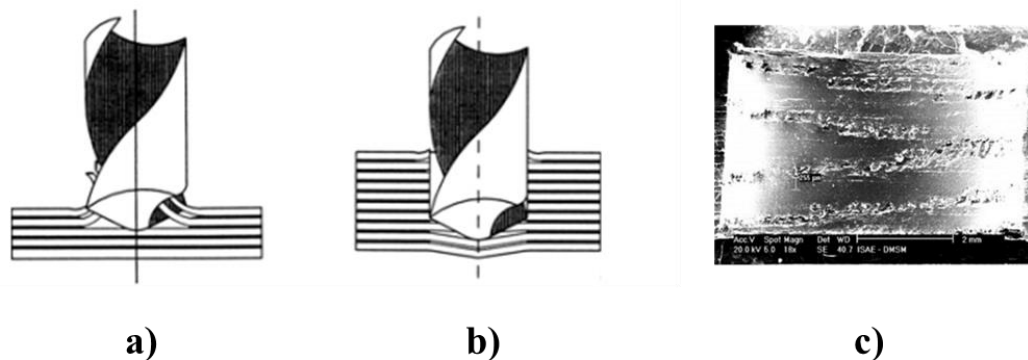
Figure 4.6. a) Peel-up delamination (Mazumdar 2002), b) push-out delamination (Mazumdar 2002), and c) drilling defects on hole wall. (Catche et al. 2015)

      From initial designs, to be discussed in the next chapter, the holes in the skin and spar may be of different shapes and sizes. While multiple operations exist that can create different shapes of holes such as abrasive waterjet, ultrasonic, laser, electrical discharge, and electrical chemical spark machining (Hocheng and Tsao 2005), only drilling methods

will be covered in this section due to their prevalence in the aerospace industry[12]. Much research has been accomplished to determine optimal parameters for conventional drilling that reduce hole defects such as burrs, matrix burnout, fiber pullout, or delamination (Figure 4.6) (Hocheng and Tsao 2005, Krishnaraj et al. 2012, Davim and Reis 2003). However, the only drilling method that appears to be both applicable for milling out different hole shapes and developed enough for industrial use is orbital drilling as defined by Brinksmeier et al. (2008).

Regarding orbital drilling, multiple parameters have been examined and optimized to reduce the chance and severity of defects (Sadek et al. 2012). In addition, robotic orbital drilling has been shown to produce consistent and reliable results, especially with aircraft manufacturing (Eguti and Trabasso 2014). An alternative method similar to orbital drilling is tilted planetary motion drilling (Figure 4.7), with some parameters examined and optimized by Tanaka et al. (2012) to reduce defects.

---

[12] Private communication with Boeing

(a) Orbital drilling

(b) Tilted planetary motion drilling
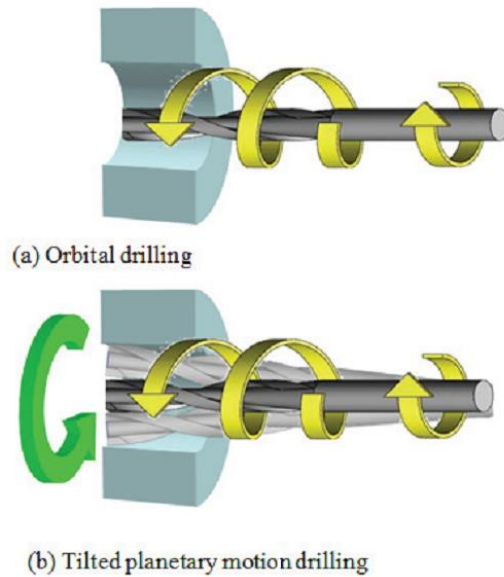
Figure 4.7. Schematic comparing two drilling methods (Tanaka et al. 2012)

From the literature examined, this project assumes the capabilities of consistently and reliably aligning holes in composites with reasonable tolerances using a milling operation similar to orbital drilling (Assumption 1). Post-processing procedures are assumed to include de-burring, cleaning, and sealing the fibers. Finally, understanding composite hole creation as a capital intensive process in terms of reducing defects and improving accuracy, guidelines are created to reduce the costs associated with composite hole drilling.

1. Reduce the amount of composite material removed, which will reduce the amount of doubler required to sufficiently reinforce the hole as well as reduce the possibility of defects and the time required to drill and apply post-processing techniques.

2. Reduce the tooling required, which will eliminate the time required to switch out equipment such as drill bits. This step is primarily mitigated with a milling operation.

3. Reduce the number of holes, which will reduce tolerancing issues associated with aligning multiple holes as well as reduce the time required to locate and drill multiple holes.

4.3.2 Joining Methods

Messler (2006) categorizes joining methods into joining by mechanical forces, chemical forces, physical forces, or some combination of the three forces (Table 4.1). Since chemical and physical joining methods are more permanent in nature, mechanical joining methods are selected to meet Constraint 4.2.2.9. Furthermore, per DFMA part reduction guidelines, manufacturing and assembly costs can be reduced by selecting integral mechanical attachment methods. Thus, this section will focus on some of the design options, further categorized in Table 4.2, that allow for integral mechanical attachment.

Table 4.1. Categorized joining methods (Messler 2006)

Using Mechanical Forces						Using Chemical Forces		Using Physical Forces*	
Primary Processes									
Integral Mechanical Attachment			Mechanical Fastening			Adhesive Joining		Welding	
Plastic Interlocks	Elastic Interlocks	Rigid Interlocks	Unthreaded Fasteners	Threaded Fasteners	Other Fasteners	Organic Adhesives	Inorganic Adhesives	Non-fusion Welding	Fusion Welding
Secondary Processes									
						Solvent Cementing	Cementing/ Mortaring		Brazing/ Soldering
Hybrid Processes									
			Rivet-Bonding				Weld-Bonding		Weld-Brazing
Variant Processes									
			Thermal Spraying						

* In the context of joining, "physical forces" refer to those forces arising from electromagnetic sources in atoms.

Table 4.2. Categorized integral mechanical attachments (Messler 2006)

Rigid Interlocks	Elastic Interlocks	Plastic Interlocks
Operate by remaining rigid; rarely employ residual stresses	Operate by deflecting elastically; sometimes employ residual stresses	Operate by being deformed plastically; rarely require residual stresses
Tongues-and-grooves	Integral spring tabs	Setting
Dovetails-and-grooves	Spring plugs	Staking
Rabbets or dados	Snap slides	Metal stitching
Mortise-and-tenons	Snap clips	Metal clinching
T-slots and Ts	Clamp fasteners	Indentation-type joints
Shaped rails and ways	Clamps	Beaded-assembly joints
Wedges and Morse tapers	Quick-release fasteners	Crimping
Shoulders and flanges	Integral snap-fit features	Hemming
Bosses, lands, and posts	Interference press fits	Thermal staking
Tabs and ears	Thermal shrink fits	Formed tabs
Integral keys and splines		
Integral threads		
Knurled surfaces		
Hinges		
Hasps		
Latches		
Hooks		
Turn-buckles		
Collars and sleeves		

Per DFMA assembly insertion and fastening guidelines (Figure 4.5), two of the fastener designs that can more efficiently reduce assembly error and costs are snap-fits and thermal staking. Since thermal staking requires additional equipment and tooling, an integral snap-fit design is selected as the ideal joining method.

Sub-classes of snap-fits include cantilever hooks, cantilevered holes or window snaps, annular and leaf-spring snaps, ball-and-socket or post-and-dome snaps, compression hooks, compression traps and beams, bayonet-and-finger snaps, and torsion snaps (Messler 2006). From these designs, cantilevered holes, window snaps, compressive traps, and bayonet-and-finger snaps are not feasible since it is difficult to cut out a complex hook shape into the composite spar. Annular, leaf-spring, ball-and-socket, and post-and-dome snaps are not ideal since they require the annulus in the composite spar to deform elastically while the hook is assumed to stay rigid. Compression beams are difficult to utilize due to the low strain limits of the thermoplastic material. While

77

torsion snap-fits are viable options (Figure 4.8), they require shear stresses to carry the loads, which may fail earlier than the flexural load bearing cantilever and compression hooks. Thus, cantilever hooks and compression hooks are deemed to be viable designs in regard to fastening onto a composite spar.
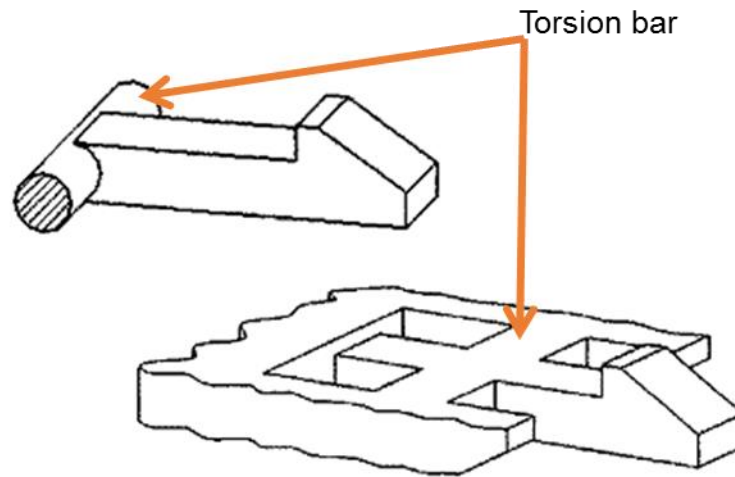
Figure 4.8. Torsion snap-fits (Messler 2006)

BASF Corporation (2007) combines cantilever hooks and compression hooks into one category of cantilever hooks (Figure 4.9). While all types of cantilever hooks are removable from the same side as it is inserted, the simple design (Figure 4.9.a) necessitates a lower separation force compared to the other cantilever designs due to a more rounded hook that should elastically deform when removed with enough force. Additionally, the U-shaped and L-shaped designs typically require a slot hole in the wall, whereas the simple cantilever hook design allows for a slot or a circular hole. The corresponding simple cantilever design for the slot hole is the simple beam in Figure 4.9.a, while the corresponding simple cantilever design for the circular hole is a discontinuous annular snap-fit (Figure 4.10).

a)   b)   c)
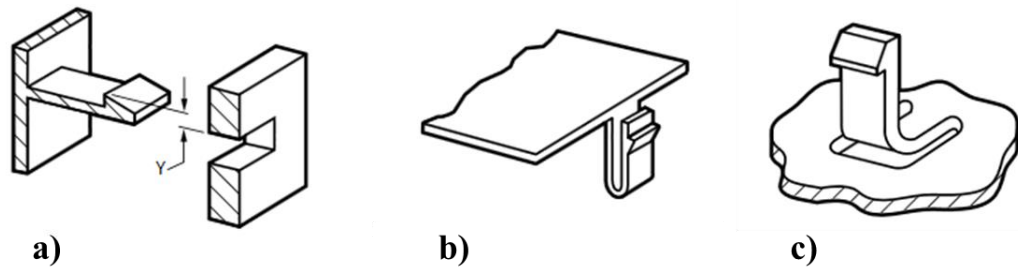
Figure 4.9. Cantilever hook designs a) simple, b) U-shaped, and c) L-shaped (BASF Corporation 2007)

Figure 4.10. Example of discontinuous annular snap-fit (BASF Corporation 2007)

For each design, certain dimensions can be optimized to produce a fastener that meets a required mating force or deflection distance, to be discussed in section 5.3.2. Here, three guidelines are presented to aid in snap-fit design (BASF Corporation 2007).

1. A fillet radius design should be incorporated at the interface of a cantilever beam and wall to reduce stress concentrations (Figure 4.11.a).

2. Beams should relax in tension to reduce creep and thus prevent significant reduction in holding force (Figure 4.11.b). Additionally, utilizing a large return angle and/or a longer land length can help retain the holding force once relaxation occurs (Figure 4.11.c).

3. Material of snap-fit should be chosen to minimize fatigue.
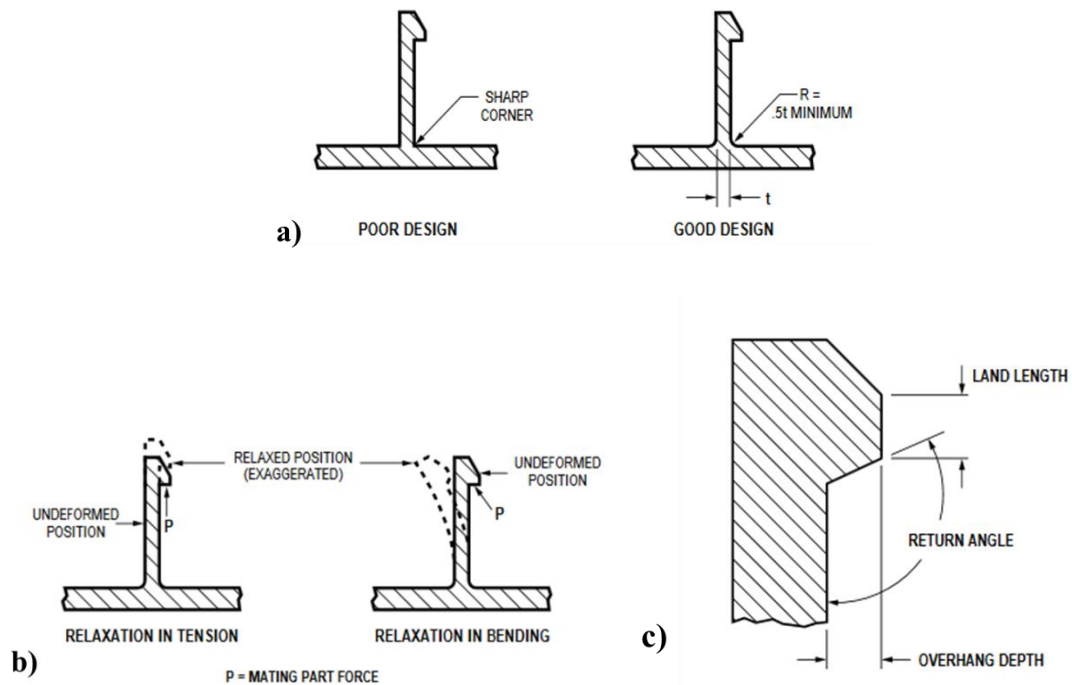
Figure 4.11. Design guidelines for 1 (a) and 2 (b) and (c)

4.4 Axiomatic Design Results

With the overview of the design methodologies and preliminary research completed, it is possible to construct the framework of the design utilizing AD. This section describes the construction of the framework in terms of FRs and DPs, along with the underlying assumptions and associated with each decision. Constraints listed out in section 4.2 will be referenced where appropriate as well.

4.4.1 First Level

From Constraints 4.2.1.1-3, three main parts of the integration solution can be constructed to form the main three FRs:

FR 1. (The actuator device that) oscillates a jet stream

FR 2. (A part that) interfaces the actuator with the wing skin

FR 3. (A part that) interfaces the actuator with the wing structure

The necessary DPs that fulfill the corresponding FRs are *DP 1.* Actuator Design, *DP 2.* Actuator-skin connection, and *DP 3.* Actuator-structure connection. With these DPs, it is possible to "zag" back to the FRs to expand the hierarchy of *what* needs to be done.

4.4.2 Second Level for FR 1 and DP 1

Under DP 1, the actuator design has two functions:

FR 1.1. Interface with the air supply mentioned in Constraints 4.2.2.5-6

FR 1.2. Withstand internal pressure set by Constraint 4.2.2.4

The corresponding DPs to vary as part of the actuator design include *DP 1.1.* Air-duct connection design and *DP 1.2.* Wall thickness.

4.4.3 Second and Third Level for FR 2 and DP 2

For DP 2, 3 functions exist, with first of those functions being:

FR 2.1. Continuously expel oscillating air from actuator to freestream

This function can be solved by designing a part that extends the actuator through the bullnose skin such that the oscillating jet can reach freestream and affect the control surface. This design will be defined as *DP 2.1.* Nozzle Profile Extension (NPE) design, which can be further decomposed into two attachment points:

FR 2.1.1. Connect NPE to skin

FR 2.1.2. Connect NPE to actuator

The resulting DPs are: *DP 2.1.1.* NPE-Skin attachment method and *DP 2.1.2.* NPE-Actuator attachment method. Following this, the second and third functions for DP 2 are as follows:

FR 2.2. Seal NPE-Skin connection point to reduce internal exposure to ice, rain, or foreign object debris (FOD)

FR 2.3. Disconnect NPE and/or actuator from wing skin as set by Constraint

4.2.2.9

Selected solutions are *DP 2.2.* Sealant system and *DP 2.3.* NPE and/or actuator detachment method from wing skin.

4.4.4 Second and Third Level for FR 3 and DP 3

Finally, under DP 3, two functions that mirror those set out in FR 2.1 and FR 2.3 are required. The first is:

FR 3.1. Transfer actuator loads to wing structure

To solve this requirement, a design is required to transfer the loads, which will be defined as *DP 3.1.* Support Mount (SM) design. Similar to FR 2.1.1 and FR 2.1.2, further requirements include:

FR 3.1.1. Connect SM to structure, which is the front spar mentioned in

Constraint 4.2.1.3

FR 3.1.2. Connect SM to actuator

Corresponding DPs are then *DP 3.1.1.* SM-Structure attachment method and *DP 3.1.2.* SM-Actuator attachment method. The final requirement for DP 3 is:

FR 3.2. Disconnect SM and/or actuator from wing structure as set by Constraint

4.2.2.9

The DP that follows is *DP 3.2.* SM and/or actuator detachment method from wing structure. All FRs and DPs are compiled into Table 4.1.

Table 4.3. List of Functional Requirements and Design Parameters

Functional Requirements	Design Parameters
1. Produce actuator with an oscillating jet stream	1. Actuator Design
1.1. Interface with air supply	1.1. Air-duct connection
1.1. Withstand internal pressure in AFC	1.2. Wall thickness
2. Interface actuator with wing skin	2. Actuator-skin connection
2.1. Continuously expel air from actuator to freestream	2.1. Nozzle Profile Extension (NPE) Design
2.1.1. Connect NPE to skin	2.1.1. NPE-Skin attachment method
2.1.2. Connect NPE to actuator	2.1.2. NPE-Actuator attachment method
2.2. Seal NPE-skin connection point	2.2. Sealant system
2.3. Disconnect NPE and/or actuator from wing skin	2.3. NPE and/or actuator detachment method from wing skin
3. Interface actuator with wing structure	3. Actuator-structure connection
3.1. Transfer actuator loads to wing structure	3.1. Support Mount (SM) Design
3.1.1. Connect SM to structure	3.1.1. SM-Structure attachment method
3.1.2. Connect SM to actuator	3.1.2. SM-Actuator attachment method
3.2. Disconnect SM and/or actuator from wing structure	3.2. SM and/or actuator detachment method from wing structure

4.4.5 Independence Axiom

To characterize the relationship between the FRs and DPs from Eq. (4.1), the matrix, $[A]$ from Eq. (4.2), is filled out and displayed in Figure 4.12. First, the diagonal of $[A]$ is marked due to necessary interaction of each DP with their corresponding FR.

			1	2	3	4	5	6	7	8	9	10	11	12	13	14		
FR 1.		1	x															DP 1.
FR 1.1.		2		x														DP 1.1.
FR 1.1.		3		x	x													DP 1.2.
FR 2.		4	x			x												DP 2.
FR 2.1.		5					x											DP 2.1.
FR 2.1.1.		6						x										DP 2.1.1.
FR 2.1.2.	=	7							x								*	DP 2.1.2.
FR 2.2.		8					x			x								DP 2.2.
FR 2.3.		9					x			x	x							DP 2.3.
FR 3.		10	x									x						DP 3.
FR 3.1.		11											x					DP 3.1.
FR 3.1.1.		12												x				DP 3.1.1.
FR 3.1.2.		13													x			DP 3.1.2.
FR 3.2.		14											x			x		DP 3.2.

Figure 4.12. Decoupled AD Matrix that solves Eq. (4.1)

Next, comparing the first level of FRs (FR 1-3), the actuator design will affect what the actuator-skin and actuator-structure connections look like. However, the actuator-skin connection should not interfere with the actuator-support connection, since they should be located at two separate locations on the actuator. Thus, $A_{4,1}$ and $A_{10,1}$ are marked as dependent.

Regarding the second levels of FRs, the design of the air-duct connection for FR 1.1 will affect the stresses surrounding that area, which will require a response in the wall thickness to withstand those stresses. Therefore, $A_{3,2}$ is marked as dependent. Under FR 2.1, the NPE design will affect both how the interface will be sealed and how the device is disconnected from the skin, and the chosen sealant system will also affect the disconnection. Similarly, under FR 3.1, the SM design will affect how the SM and/or actuator is disconnected from the structure. Thus, $A_{8,5}$, $A_{9,5}$, $A_{9,8}$, and $A_{14,11}$ are marked. Since there are no other interactions, the matrix can be categorized as decoupled, and the Independence Axiom can be sufficiently met. In the following chapter, this framework of FRs and DPs will structure the process for designing the solution.

4.5 Design for Manufacturing and Assembly Preliminary Results

DFMA will be used both in this section to select a set of manufacturing processes and the following chapter to design specific features for the solution. Here, two of the first steps for DFMA will be covered.

4.5.1 Design for Assembly

Referring back to Figure 4.2, once a design concept has been created, the next step is to follow DFA procedures and guidelines. The primary decision to be made for this step is to determine whether the assembly is manual, robotic, or automatic, which largely depends on the expected production volume. Assuming that 16 actuators are sufficient for one flap (Meyer et al. 2014), four flaps on a civil transport aircraft, there is

a total of 64 actuators in the flaps of a commercial aircraft (Assumption 3). With production rates of a single 747 aircraft per month (Boeing 2016) to forty-seven 737 aircrafts per month (Trimble 2015), the production volume of the actuators range from 768 to 36,096 per year. Thus, manual and robotic assembly design guidelines shall be prioritized.

4.5.2 Selection of Materials and Processes

The next step in Figure 4.2 involves the "selection of material and manufacturing processes and early DFM cost estimates." By discussing the available set of materials and manufacturing processes to select from early in the design process, features can be better designed to take advantage of or avoid disadvantages of certain manufacturing methods. The cost estimate, however, will be reviewed in chapter 6 once final designs are discussed.

From Constraint 4.2.2.2, the thermoplastic material has already been selected. Research in section 2.4 and experiments conducted in chapter 3 demonstrate that molding processes (thermoforming, hot embossing, injection molding, and injection compression molding), machining, FDM, and SLS are viable options for a thermoplastic material. However, following design guidelines for reducing the part count, the manufacturing method ought to be able to produce the actuator, NPE, and SM in as few pieces as possible. This is to not only ensure lower manufacturing cost and assembly time, but also to reduce errors during manufacturing and assembly and to reduce potential failure locations.

Since thermoforming and hot embossing require sheets to create parts, they require a minimum of three separate parts: an embossed bottom part of the actuator, a top cover, and the SM, assuming that the NPE can be integrated into the bottom part. Machining would require the same three parts, although it is possible to create the bottom part and the SM as one piece with a separate manufacturing process (e.g., injection

85

molding), machine out the design, and add the top cover as the second piece. Injection molding and injection compression molding would require a minimum of 2 parts (an embossed bottom actuator part with an integrated SM and a top cover). Finally, FDM and SLS are able to create the actuator, NPE, and SM all as one integrated part (FDM would require a dissolvable material to be utilized). From this quick analysis, it is possible to eliminate thermoforming and hot embossing from the available methods due to higher part count. Additionally, since injection compression molding is noted to be a more complex process (Becker and Gärtner 2008) than injection molding, the former will also be eliminated, leaving injection molding, machining, FDM, and SLS as the remaining manufacturing processes.

For further down-selection, machining will be eliminated due to the high cost in terms of manufacturing time of hours or even days required for each part (Becker and Gärtner 2008), and FDM will be eliminated due to high surface roughness, which may unnecessarily induce drag internally. Thus, all features of the integration solution will design for injection molding and SLS processes. However, if new information surfaces regarding greater benefits from machining, FDM, or even other molding processes, the selection of manufacturing processes ought to be revaluated.

Regarding further design procedures, it is important to note that the material properties will differ based on the different manufacturing methods. A laser sintered product is inherently weaker than an injection molded product of the same material due to sintering powder material for the former versus material that is fused and compressed together for the latter. On top of that, an SLS manufactured product is weaker in the z direction than either the x or y directions. Thus, for simplified modeling and simulations, isotropic, linear elastic behavior of the z direction, SLS manufactured properties are assumed (Assumption 3), which are listed in Table 4.4. If the simulations were to take injection molded properties into account, a key factor to acknowledge is that any

incorporated carbon or glass fibers will orient themselves parallel to the flow, which will result in orthotropic linear elastic behavior.

Table 4.4. Material Properties

	23% CF/PEKK[13]
Manufacturing method	SLS
Ultimate Tensile Strength (psi)	8702
Elastic Modulus (ksi)	900
Strain-to-failure (%)	1

4.6 Chapter Summary

First, two design methodologies are outlined to aid in design discussions in the following chapter. Next, constraints utilized in this project are listed to define the design space. Relevant topics of composite holes and joining methods are then discussed that narrow down design options and add to design guidelines for the integration solution. Finally, initial procedures of the design methodologies are followed for AD, summarized in Table 4.3, and for DFMA, which concluded that manual and robotic assembly guidelines should be prioritized and that the BDC should design for injection molding and SLS manufacturing methods. Remaining design processes will be expanded upon in chapter 5.

---

[13] Private Communication with Boeing and Advanced Laser Materials

CHAPTER 5

DESIGN RESULTS

This chapter follows the framework constructed in section 4.4. For each DP, a combination of DFMA guidelines, simulations, and research is used to select certain options and to identify tradeoffs between other options, all of which will be used to create the best design concept (BDC). At the end of each section, a morphological chart will summarize the design options. Finally, the BDC model creation will be discussed, followed by the presentation of the BDC as three separate designs in the last section, to be further evaluated in the following chapter.

5.1 DP 1. Actuator Design

In prior experiments involving fluidic oscillators of the unit size by DeSalvo et al. (2011), multiple fluidic oscillators were packaged together in an array, sharing a single plenum[14]. The width of a single unit (x direction) was seen as sufficient for those experiments. Thus, the unit width scaled by six (the same factor dictated by Constraint 4.2.2.1) was assumed to be the minimum, internal width required for the actuator to function, without the need for a plenum to extend around the sides. The internal height of the actuator is set at ~0.35 in. (9 mm), which is also six times the unit height. A model is created in Figure 5.1 that depicts the coordinate system used and the definitions of the features. The bottom of the actuator (below) is the face opposite the top (above); the back (behind) is opposite the front; the left side is opposite the right side (Figure 5.1). An internal horseshoe shape design partially joins the top and bottom actuator walls.

---

[14] Private Communication with Michael DeSalvo of Georgia Tech's FMRL
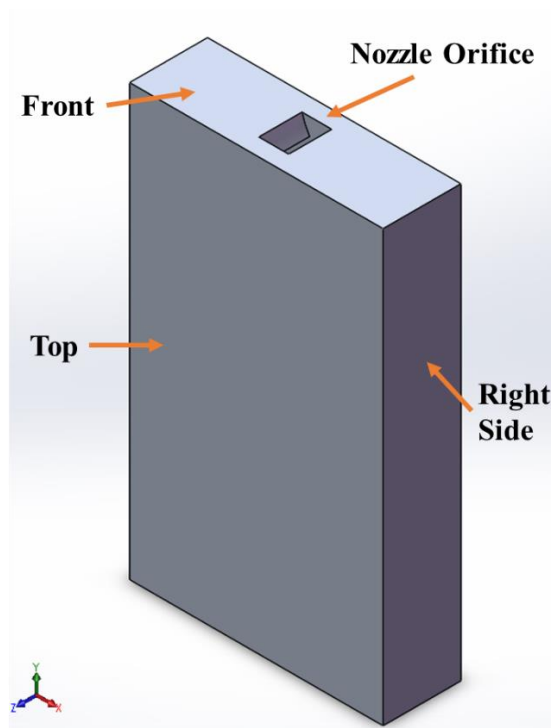
Figure 5.1. Isometric view of actuator and coordinate system

5.1.1 Air-Duct Connection

A circular shape (Figure 5.2) is assumed for the interface between the actuator and the air supply due to even stress distributions for a circular duct compared to any other shape with corners. However, it is important to note that the circular design can be switched to another design that is more adept at interfacing with a standard pipe or duct fitting. Designing for standards that are already in place will reduce the cost of buying or manufacturing a new fitting as well as eliminate the equipment and skill required for a new assembly method.
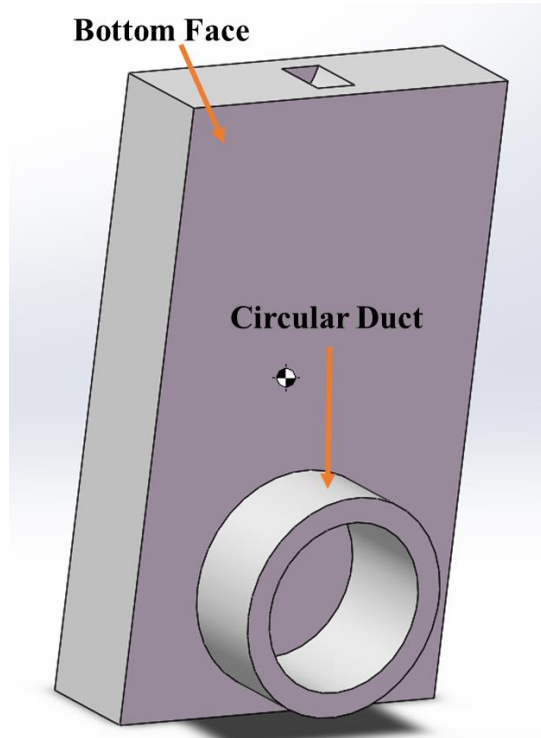
Figure 5.2. Circular duct feature

From Constraint 4.2.2.6, a ¾ in.^{2} cross-sectional duct opening corresponds to a

0.49 in. radius, assuming a circular shape. Thus, the actuator device requires a space that

is at least 1 in. x 1 in. This is important in determining the location of the interface.

Neither the left nor the right side of the actuator should support the interface, since the

internal air flow would not be able to evenly pass through the internal design. Examining

the remaining potential locations for the interface above, below, and behind the actuator,

a full scale model was constructed to visualize the volumetric constraints (Figure 5.3).

The bullnose and the front spar were modeled according to Constraints 4.2.1.1-2,

following the outline of a Fowler flap model provided by Boeing. The model was scaled

by a factor of 13.5 to achieve a chord length similar to that of the larger end of a 777

outboard flap. A design option for the NPE in DP 2 is modeled as a placeholder (Figure

5.3) to help visualize the remaining space for the actuator; both the NPE and actuator are

angled in accordance with Constraint 4.2.2.3 such that the airfoil tangent is located at the point where the actuator contacts the bullnose skin.
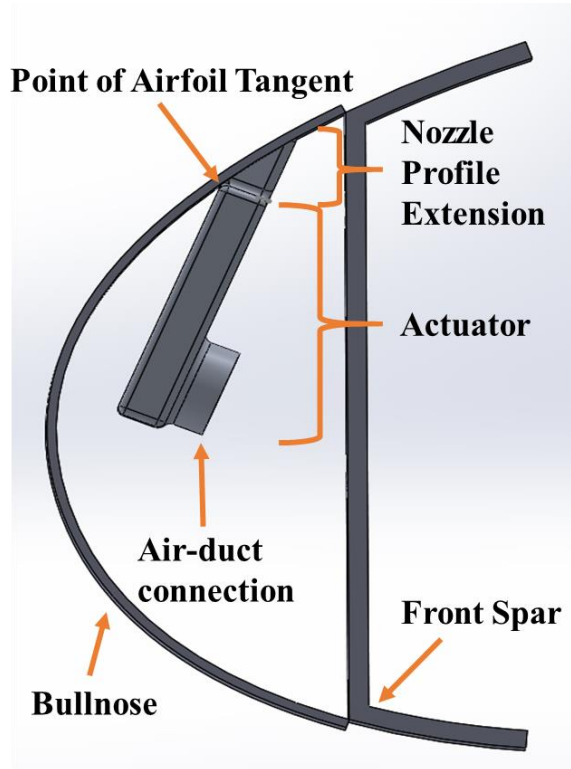
Figure 5.3. Right side view of integrated actuator at flap leading edge

From Figure 5.3 the space between the bullnose skin and the top face of the actuator is an ideal location for the air-duct connection feature in terms of easily locating the feature and attaching the pipe/duct fitting to it. However, the small volume would require a tight fit and multiple bends for the pipe/duct fitting. Thus, the remaining locations that have enough room for attaching the pipe/duct fitting to the interface are behind and below the actuator.

With the internal height of the actuator at ~0.35 in. (9 mm), there is not enough area on the back face of the actuator to model the interface, which leaves the bottom of the actuator as the final location for the circular air-duct connection (Figure 5.3). The designation of the connection feature, in turn, sets the minimum length of the actuator as

being long enough to contain the feature. Moreover, the placement of the feature at the

bottom will allow for a more injection moldable design, as opposed to placement of the

feature at the back, which would require at least another side-pull.

5.1.2 Wall Thickness

Using the actuator modeled in Figure 5.3, it is possible to conduct finite element

analysis (FEA) simulations to design for the 30 ± 5 psi from Constraint 4.2.2.4. From

design guidelines for injection molding (Boothroyd 2002), the wall thickness of the part

should be the same throughout to allow for even part cooling, which will minimize part

distortion. Therefore, the minimum wall thickness, located at the nozzle wall (0.1426 in.),

is set as the maximum wall thickness to design by and test. Since the thickness is close to

1/8 in., a simple minimum thickness, half of 1/8 in. (1/16 in.), is chosen. Another reason

to choose these thicknesses is that they are common ranges for injection molded parts.

Thus, using ANSYS Workbench R15.0, simulations with 70 psi (35 psi with a safety

factor of 2) acting in the normal direction on all internal actuator surfaces are conducted

on two models, each with a different wall thickness.

On each of these models, two tests with different support boundary conditions are

created: a maximum constraint and a minimum constraint. Maximum constraint assumes

that the entire bottom surface of the actuator is simply supported by a rigid SM design

(Figure 5.4.a). Minimum constraint assumes that only the air-duct connection is simply

supported solely by the pipe/duct fitting as a worst case scenario (Figure 5.4.b). Finally,

Assumption 3 is used for the material properties, resulting in the use of the material

properties in Table 4.4. Poisson's ratio was assumed to be 0.3.
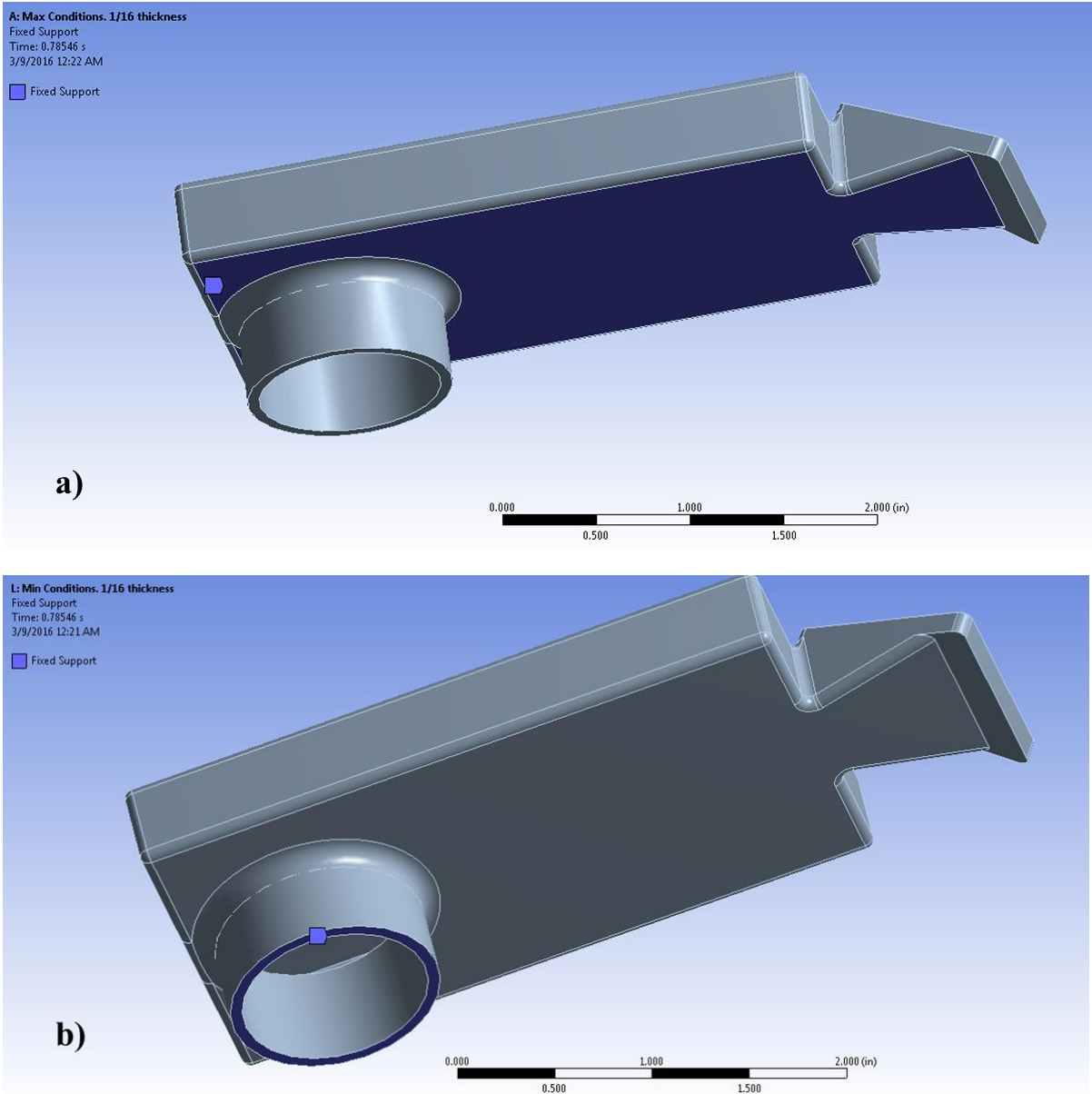
Figure 5.4. Simple support with 1/16" wall thickness under a) maximum constraint and b) minimum constraint shaded in

For the 1/16 in. wall thickness actuators, the stress and strain concentrations are depicted in Figure 5.5. Maximum stress and strain occur behind the internal horseshoe shape structure (Figure 5.5.a) on the top wall for the maximum constraints, and a slight bulge occurs further behind due to the unstrained plenum space. On the other hand,

maximum stress and stain are seen at the juncture between the actuator and the air-duct

connection for the minimum constraints.
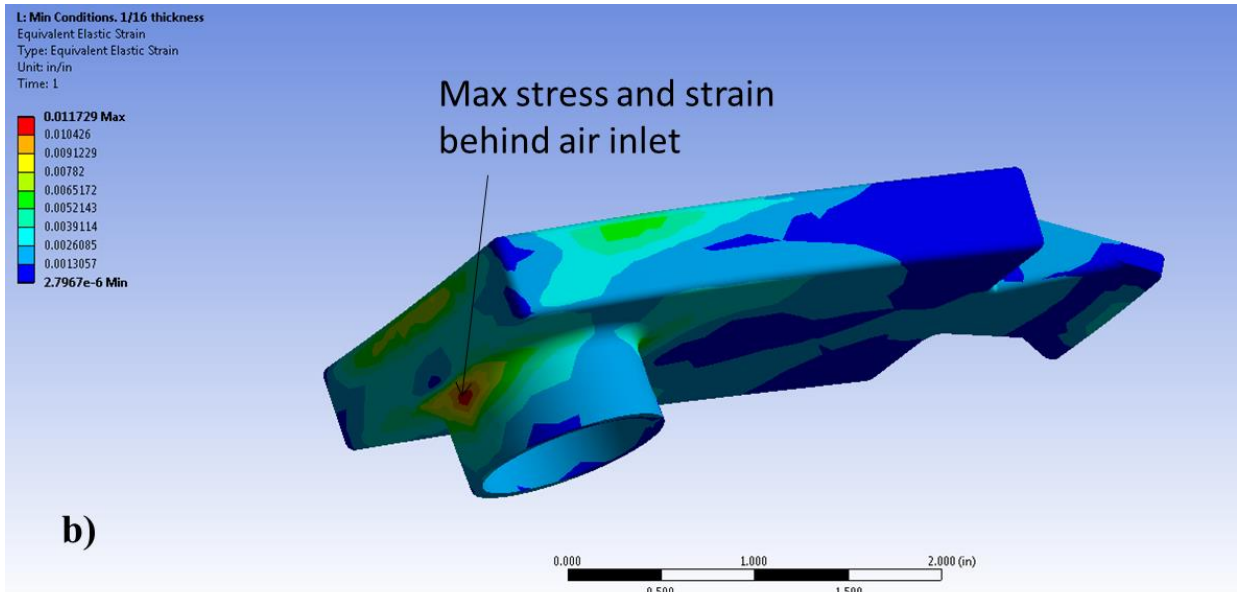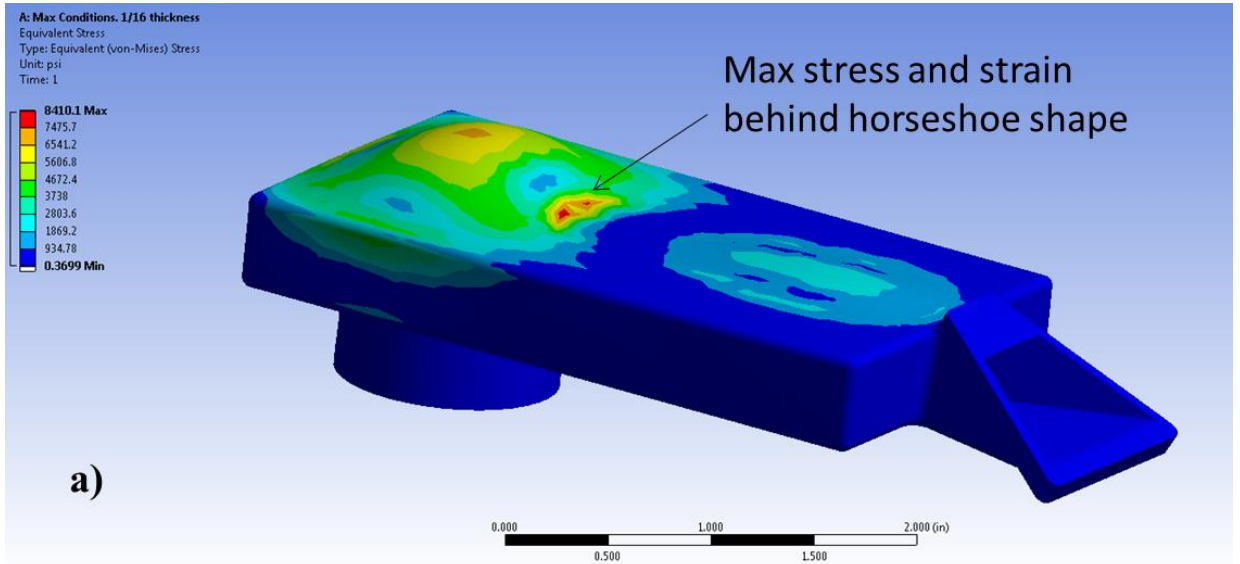
Figure 5.5. 1/16 in. wall thickness with a) maximum constraint and b) minimum constraint

Similarly, maximum stress and strain concentrations occur in the same areas on the actuators with 0.1426 in. wall thickness for the respective maximum and minimum constraints (Figure 5.6).
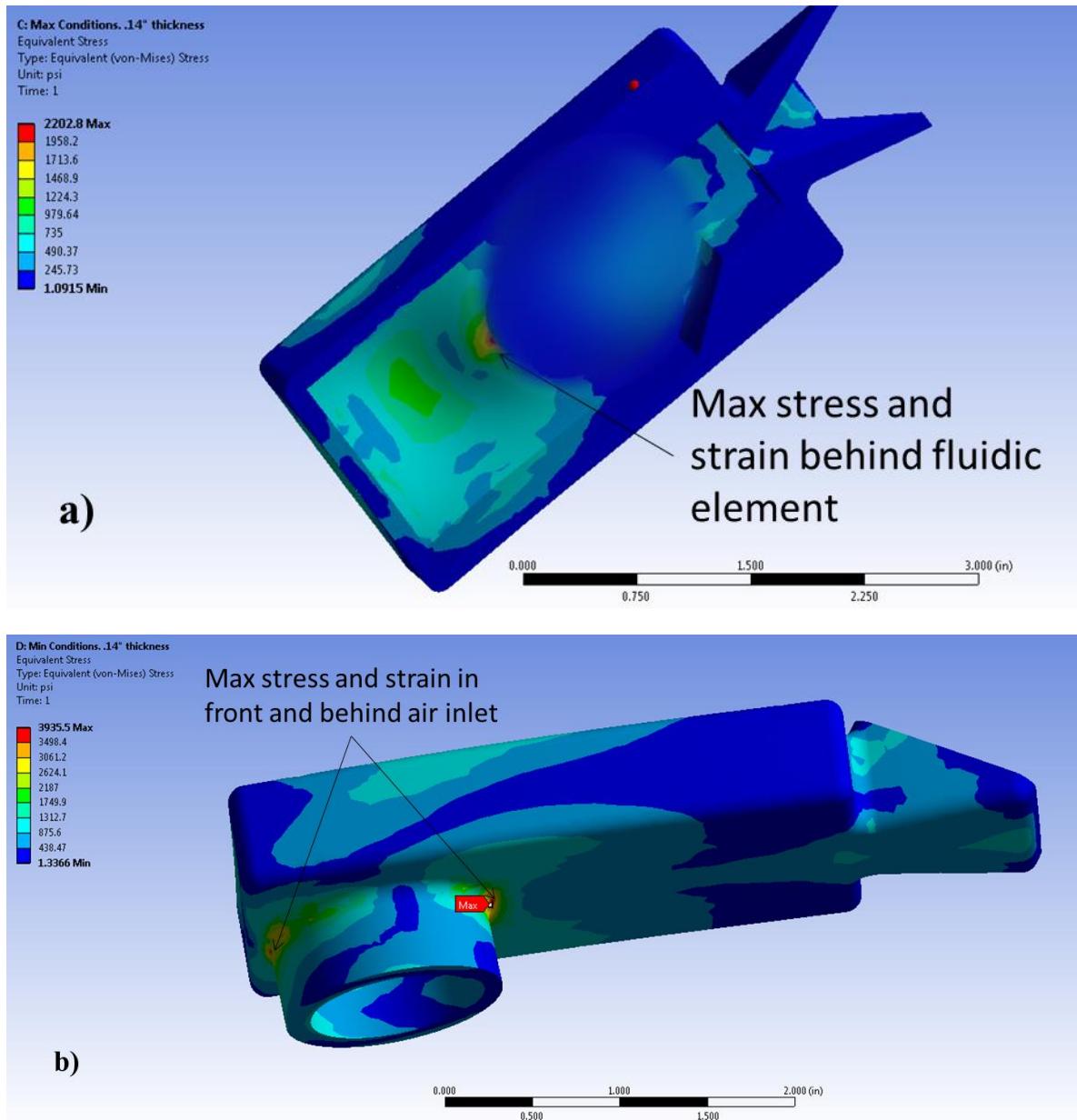
Figure 5.6. 0.1426 in. wall thickness with a) maximum constraint (cross sectional view from below) and b) minimum constraint

The stress, strain, and total deformation values are displayed in Table 5.1 and are compared with the maximum allowable values, assuming a yield stress equivalent to the ultimate tensile strength (UTS) and 1% strain-to-failure from Table 4.4. It is clear that the 1/16 in. wall thickness actuator reaches up to the maximum allowable strain under both maximum and minimum constraints. For the same thickness, under minimum constraint, the maximum allowable stress is exceeded, whereas under maximum constraint, the stress remains below the maximum value. For a 0.1426 in. wall thickness, all stress and strain values remain well below maximum allowable values. Therefore, it is possible to conclude that a wall thickness range of 1/16 – 0.1426 in. is reasonable.

Table 5.1. Maximum deformation, stress, and strain values from simulation

	1/16" Max	1/16" Min	0.14" Max	0.14" Min	Maximum allowable values
Maximum Total Deformation (in)	0.027	0.142	0.003	0.039	-
Maximum Equivalent Elastic Strain	0.010	0.012	0.003	0.004	0.01
Maximum Equivalent von Mises Stress (psi)	8410.1	10295	2202.8	3935.5	8702.3

Finally, in the case of foreign object debris (FOD) lodging into the nozzle opening, the air blowing out of the nozzle should be pressurized to dislodge debris or heated to melt any ice, which should be feasible if the air supply is bled from the engine (McLean et al. 1999). Of course, this scenario should be examined more closely to determine the effects of blowing faster or higher temperature air on jet oscillation. In the worst case scenario of FOD completely blocking the nozzle opening, a critical half-crack length (leak-before-break criterion) is calculated to determine the maximum wall thickness such that the actuator meets a fail-safe criterion. A wall thickness greater than the critical length would allow a crack to propagate and potentially burst, whereas a wall thickness less than the critical length would allow air to leak out from a stable crack

opening. With the assumption that the material experiences isotropic, linear elastic

behavior, linear elastic fracture mechanics is assumed to be valid, with the equation

$$K_{IC} = \sigma_w \sqrt{\pi a_c} \quad [MPa\sqrt{m}] \tag{5.1}$$

where K_{IC} is the fracture toughness of the material, σ_w is the local normal stress in the

pressurized wall, and a_c is the critical half-crack length.

Rearranging Eq. (5.1), it is possible to solve for the critical half-crack length:

$a_c = \frac{1}{\pi}\left(\frac{K_{IC}}{\sigma_w}\right)^2$. From discussion with engineers at RTP Company, it is known that PEEK

has similar high strength material properties as PEKK. Thus, assuming K_{IC} of carbon

fiber reinforced PEKK is equated with $K_{IC} = 3 \, MPa \, \sqrt{m}$ of PEEK at low strain rates

(Gensler et al. 1996) (Assumption 4) and determining the maximum normal stress

experienced from 0.1426 in. wall thickness simulations ($\sigma_w = 2556 \, psi$), $a_c = 0.363$ in.

Thus, a wall thickness that is 0.1426 in. is sufficient in meeting this leak-before-break

criterion with a safety factor of two. Table 5.2 displays the design options for this section

in a morphological chart.

Table 5.2. Morphological chart for DP 1

Function	Solutions		
Air-duct connection location	Back	Bottom	Top

5.2 DP 2. Actuator-Skin Connection

5.2.1 Nozzle Profile Extension Design

As mentioned in FR 2.1, the purpose the nozzle design serves is to interface the

actuator with the bullnose skin. With the selected manufacturing methods of injection

97

molding and SLS, it is possible and beneficial to integrate the NPE design into the actuator to reduce the part count, per DFMA part reduction guidelines. Additionally, an integrated part ensures that the NPE is securely supported by the actuator and not the skin, since the bullnose is unable to provide structural support from Constraint 4.2.1.1. Thus, only the NPE-Skin attachment method (DP 2.1.2) remains to be considered.

From the research discussed in section 2.2.3 (DeSalvo et al. 2011), the recessed design is utilized such that the air exiting the nozzle can flow as tangential as possible to the flap's outer control surface without a "step" in the airfoil shape. Next, drilling through the composite is a preferable solution[15] for creating the required hole in the bullnose skin, as opposed to building up the composite skin around a hole shape, which may only be a preferable method for reinforcing the hole with additional ply layers[155]. Through a milling operation, it is possible to cut out the desired, complex shape as discussed in section 4.3.1; thus, a milling operation will be assumed as the method used to drill all holes (Assumption 1), reducing the tooling required for production per the second composite hole guideline in section 4.3.1.

Designs that utilized the skin as part of the NPE or required cuts originating from the internal side of the skin were considered in order to reduce the amount of composite material removed (Figure 5.7). However, those designs would require "knife-edges" and thus weaker areas to be created in the skin, rendering them unfeasible[15].

---

[15] Private Communication with Boeing
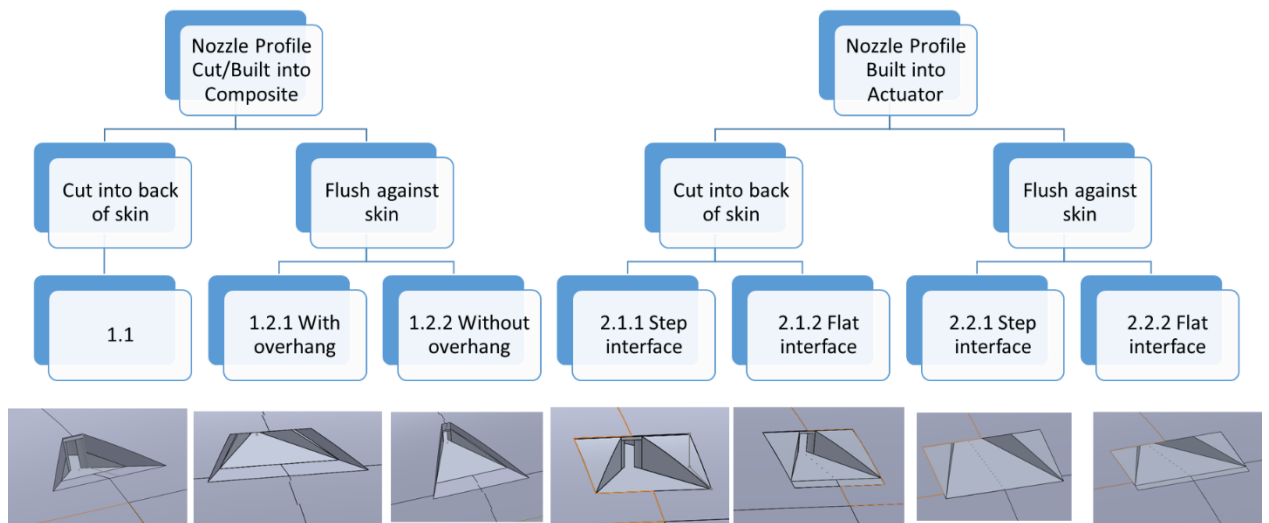
Figure 5.7. First iteration of NPE designs

Accordingly, a design based on a straight cut, drilled perpendicularly to the skin, was selected. This straight cut is displayed in the form of three different shapes (Figure 5.8), partially derived from discussions in section 2.2.2, that can be inserted into the corresponding hole shapes in the skin. The trapezoid shape takes the form of what would naturally occur if the nozzle were integrated into the skin, as seen in the 757 ecoDemonstrator (Figure 2.8); the oval shape is similar to the oblong slot shape seen in research on wind turbine blades (Figure 2.13). The rectangle shape is simply the middle option. For each of the shapes, the corners are rounded to reduce stress concentrations and thus crack propensity, while the wall thicknesses are designed to be similar to the wall thickness of the actuator (~.1426 in.). The differences between these shapes were examined via FEA simulations in ANSYS Workbench R15.0.
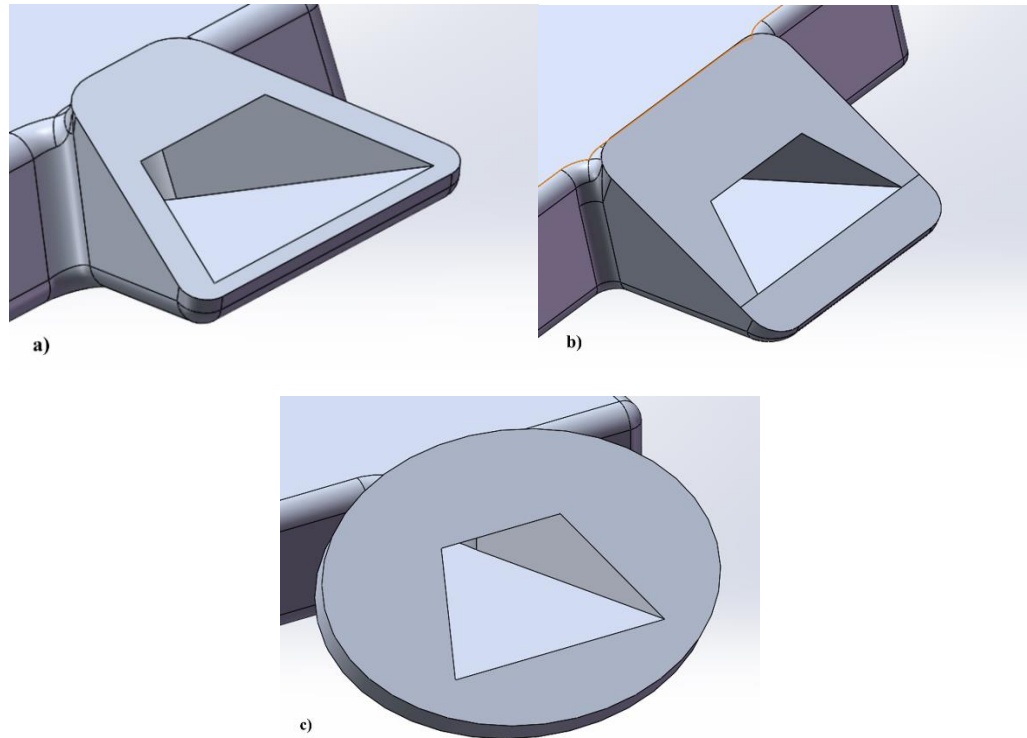
Figure 5.8. Straight cut NPE design with a) trapezoid, b) rectangle, and c) oval shapes

The three shapes were modeled as holes (Figure 5.10) in a 6 in. x 6 in. x 0.12 in. flat plate, representing a section of the bullnose skin according to Constraints 4.2.1.1 and 4.2.2.8. Skin material was assumed to be a unidirectional composite, quasi-isotropic laminate of epoxy and S-glass fiber with a fiber volume fraction of 47% and material properties in Table 5.3 (CES EduPack 2015). After the mesh was refined on all sides of each hole wall, two cases of loading conditions were tested: 1.0 lbf acting normal to the bottom side of the hole wall (Case 1) (Figure 5.10.a) and 1.0 psi acting normal to all sides of the hole wall (Case 2) (Figure 5.10.b). The purpose of these loading conditions is to compare the stress concentration locations and maximum stresses and strains with each other, hence the use of an arbitrary unit force and pressure as loads.
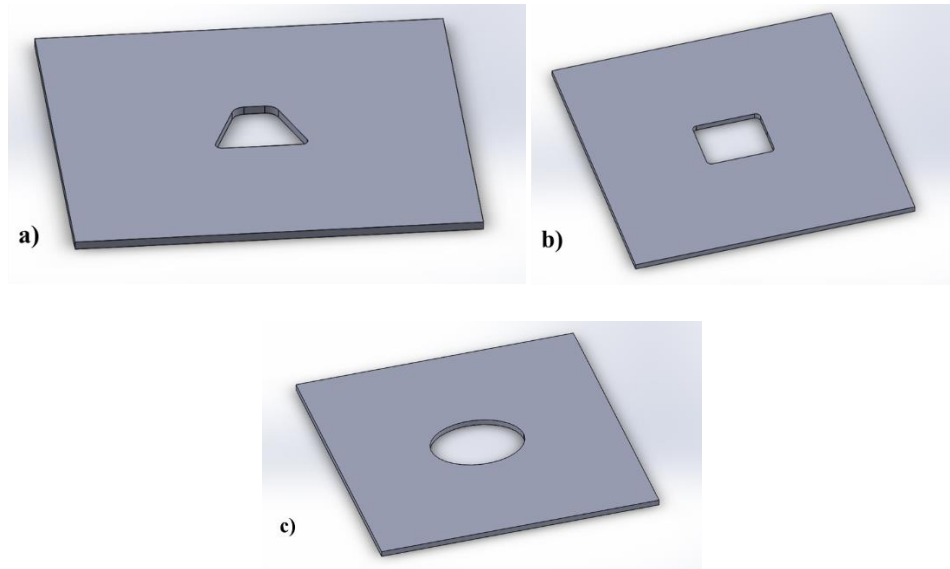
Figure 5.9. Skin models for a) trapezoid, b) rectangle, and c) oval shape holes

Table 5.3. Material properties of composite skin (CES EduPack 2015)

Composite Values	
Density (lb/in^3)	0.0665
Elastic Modulus (psi)	2.76E+06
Poisson's Ratio	0.303
Strain-to-Failure (%)	1.5
Yield Stress (psi)	66300
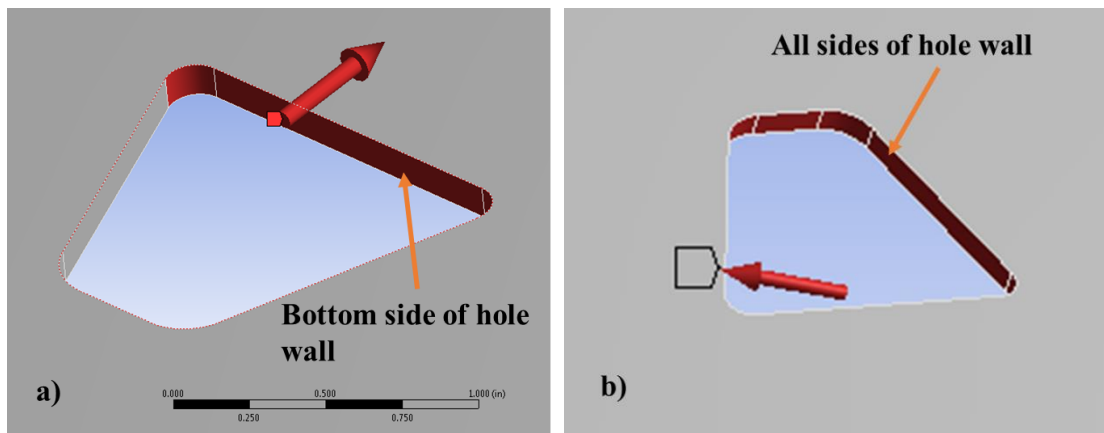
Figure 5.10. Loading conditions on trapezoid shape for a) Case 1 and b) Case 2

In both cases, maximum stresses and strains are concentrated at the corners with the highest curvatures for the trapezoid and oval shapes or equally concentrated at all corners for the rectangle shape (Figures 5.11 and 5.12). Assuming the trapezoid shape as the baseline, as the shape changes to rectangle (44% greater area) and then oval (101% greater area), the stresses and strains spread out to larger areas in the skin for both cases (Figures 5.11 and 5.12). However, maximum stresses and strains increase for a rectangle shaped hole by 15% for Case 1 and by 5% for Case 2 but decrease significantly for an oval shaped hole by 54% for both cases (Table 5.4). This demonstrates that either the trapezoid hole shape or the oval hole shape should be selected, based on whether the hole area or maximum stress and strain values should be minimized. Since the guideline to reduce the amount of composite material removed was set earlier (section 4.2.1), the trapezoidal shape (Figure 5.8.a) is selected. However, this design decision ought to be revaluated if the stress concentrations experienced by the composite are assigned a greater level of importance.
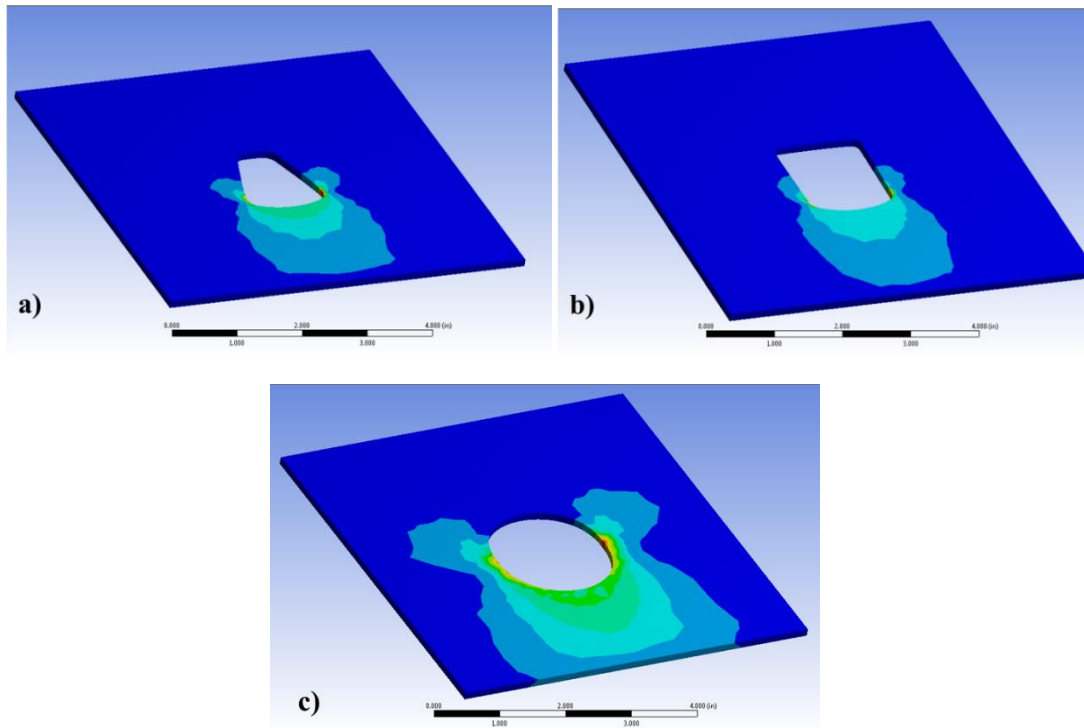
Figure 5.11. Case 1 conditions for a) trapezoid, b) rectangle, and c) oval shapes

Max stress and strain concentrations

Max stress and strain concentrations

Max stress and strain concentrations
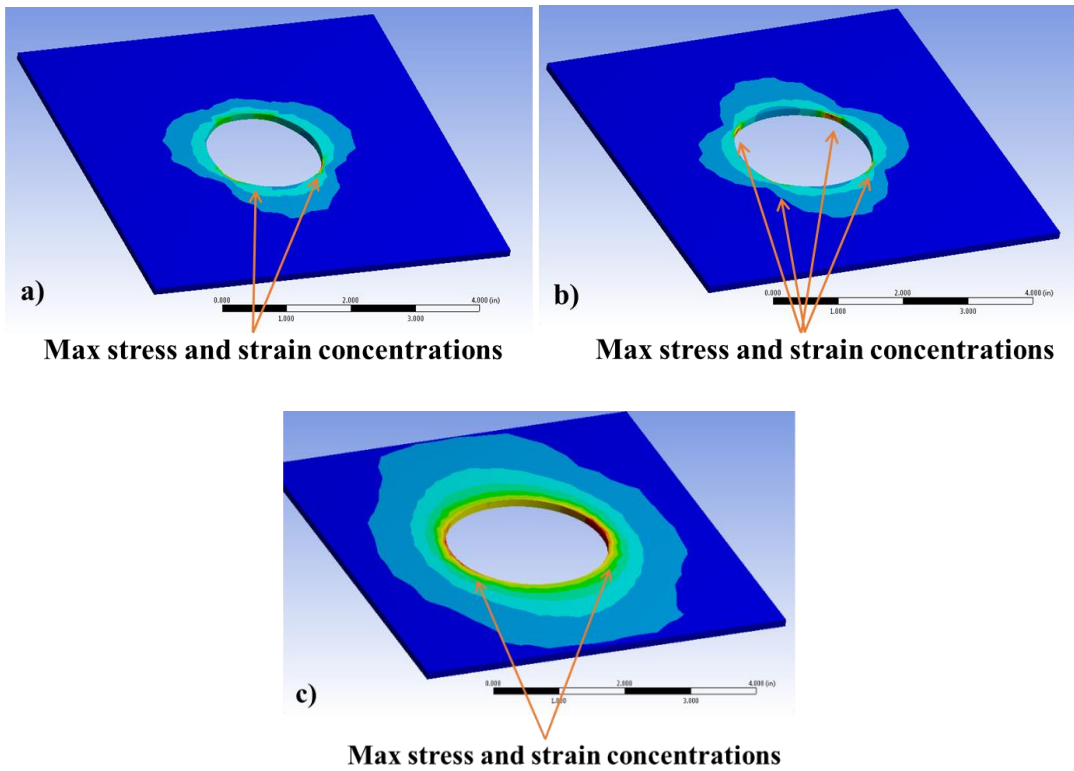
Figure 5.12. Case 2 conditions for a) trapezoid, b) rectangle, and c) oval shapes

Table 5.4. Results from comparing different hole shapes

		Trapezoid	Rectangle	Oval
	Area of hole (in^2)	1.17	6.93	6.47
Case 1: 1 lb force	Maximum Total Deformation (in)	2.78E-06	2.80E-06	1.80E-06
	Maximum Equivalent Elastic Strain (in/in)	4.92E-06	5.66E-06	2.27E-06
	Maximum Equivalent Stress (psi)	13.55	15.564	6.1387
Case 2: 1 psi pressure	Maximum Total Deformation (in)	4.10E-07	4.46E-07	4.15E-07
	Maximum Equivalent Elastic Strain (in/in)	1.50E-06	1.57E-06	6.82E-07
	Maximum Equivalent Stress (psi)	4.121	4.321	1.879

Regarding drilled holes in composites, three critical factors affect the hole size:

1. Bullnose skin/actuator wall thickness

2. Thermal expansion and contraction

3. Sealing the exposed fibers

First, any thickness increase, either due to a doubler literally doubling the skin thickness around the hole for reinforcement or due to increased actuator wall thickness to withstand higher pressures, will necessarily increase the hole size or area. According to initial (and also final) designs, one edge of the actuator should contact the internal side of the bullnose skin at the "point of airfoil tangent" (Figure 5.3) to reduce the distance the jet travels from the nozzle orifice to the control surface. The further the nozzle orifice is from the control surface, the wider the NPE is due to the nozzle orifice angle (Figure 5.13). Therefore, the thicknesses of the skin and actuator wall at the contact point, along with the nozzle orifice angle and curvature of the skin, dictate the hole area.
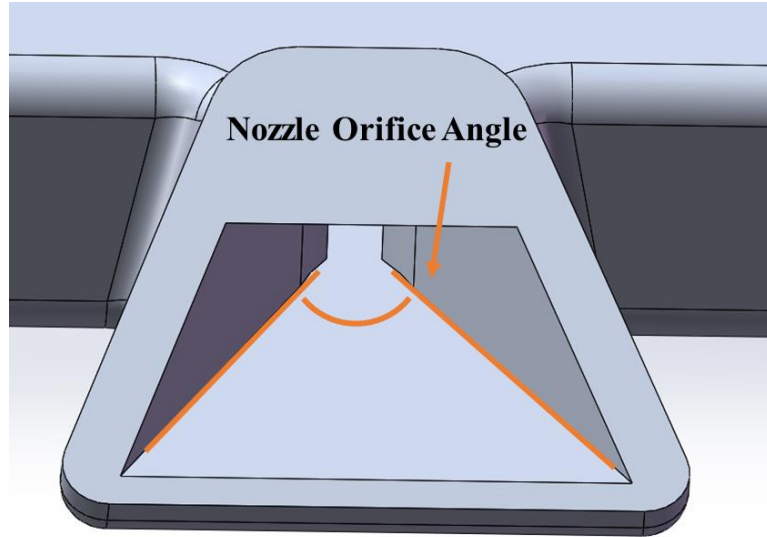
Figure 5.13. Front view of NPE

The effect of increased skin thickness is examined on the NPE (Figure 5.14). Doubling the 0.12 in. skin thickness resulted in roughly a 33% increase in hole area, from 1.17 in^2 to 1.56 in^2. This increase may result in further reinforcements, which would require an optimization study to determine the balance between minimal composite material removed and sufficient reinforcement of the resulting hole. Since the actuator wall thickness range is much lower, its effect on hole size should be less than that incurred by skin reinforcement. Nonetheless, a second optimization study should focus on the balance between wall thickness and withstanding internal loads.
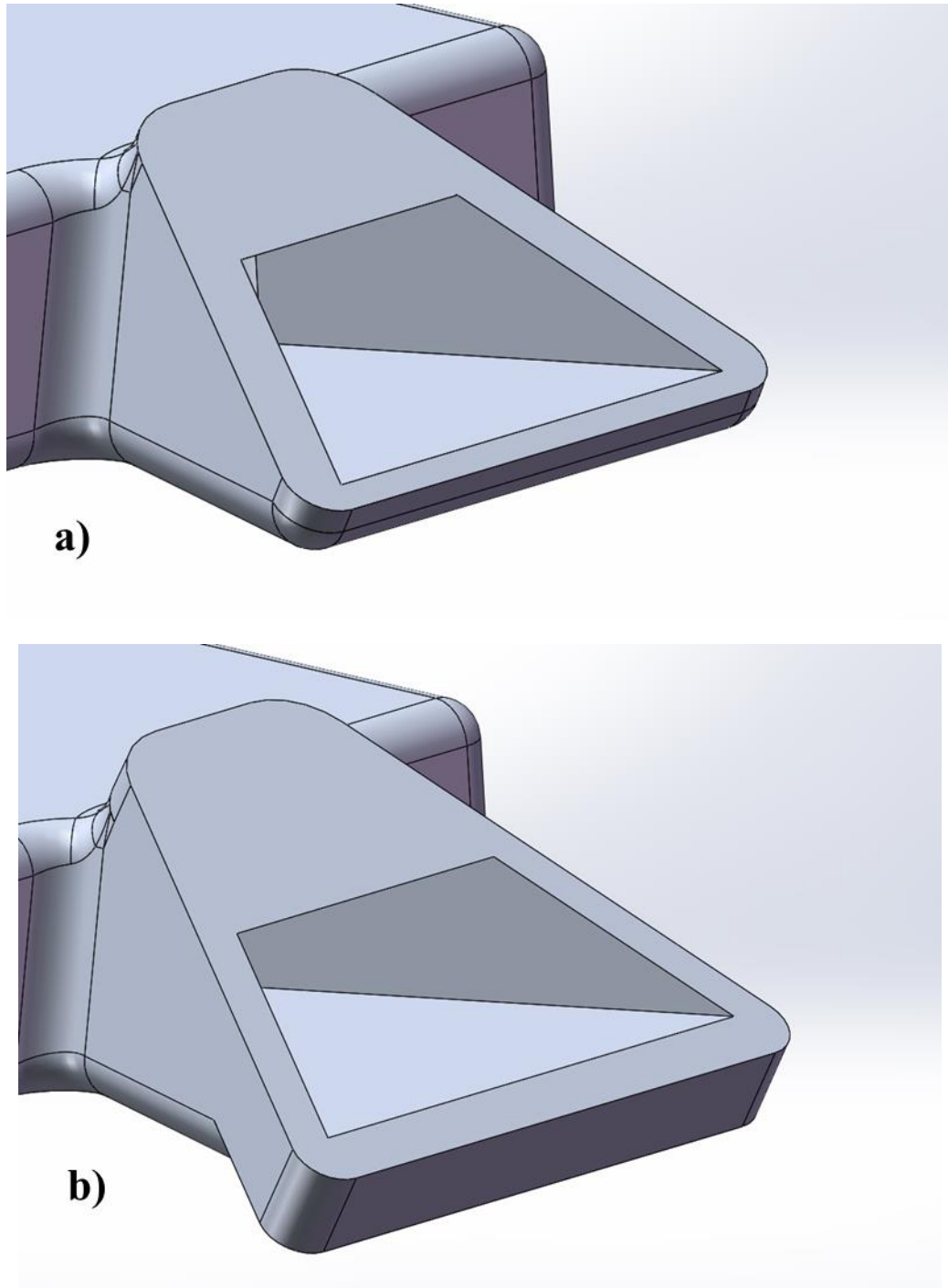
Figure 5.14. NPE for a) 0.12 in. and b) 0.24 in. thick skin

The second critical factor, involving thermal expansion and contraction, involves the thermal expansion coefficient of the materials used at the hole and the temperature range at which the location is rated. One solution to decreasing the effect of thermal

expansion is to use materials with similar coefficients, such as a glass fiber reinforced thermoplastic material for the actuator and NPE. Using the same type of glass fiber as that used in the bullnose skin would resolve most of the issues surrounding thermal expansion and contraction.

Finally, the process of sealing exposed fibers in the skin requires the holes to be created wider than expected, since the sealant applied on the composite will add a certain thickness, reducing the hole size. Therefore, the hole will be wider in all directions according to the average thickness the sealant adds to ensure a proper fit with the NPE.

In the end, each design allows the NPE to slide into its corresponding hole shape in the skin. Thus, with appropriately designed tolerances, the bullnose ought to pop into place over the installed actuators without the need for additional attachments, reducing the assembly time.

5.2.2 Sealant System

With the selected design, a sealant system is desired at this interface to prevent FOD from entering the gap created between the NPE and the corresponding skin hole. Design options include an O-ring, a gasket, or another standard sealant used for control surfaces. Due to incomplete knowledge regarding standard sealants used on commercial aircraft, the sealant will be assumed to be a polysulfide sealant (Assumption 5). An O-ring design incorporates a groove located on the NPE such that the O-ring seals against the hole wall of the composite (Figure 5.15). A gasket design would seal a flat surface, similar to a flange, against the internal side of the skin, around the hole perimeter. To maintain the seal, a constant pressure would have to be applied against the gasket; any loss in pressure would result in a broken seal. Finally, for a standard sealant design, the sealant would be applied on the surface of the NPE to seal the side walls of the hole. All three designs are sketched out in the morphological chart in section 5.2.3.
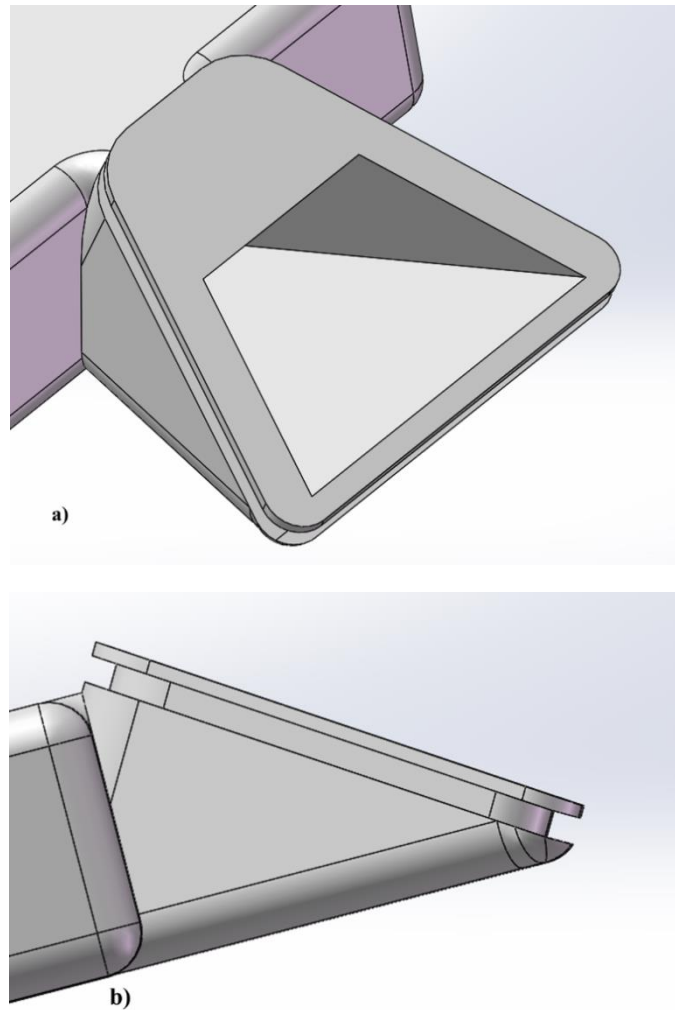
Figure 5.15. O-ring groove on NPE with a) front, isometric view and b) right side view

Due to the additional pressure requirement in utilizing a gasket, only the O-ring and polysulfide options are considered. Designing for the manufacturing method, an O-ring is selected when using SLS due to its ability to create a complex groove for the O-ring to fit into; further design work on the O-ring groove should consider the minimum thickness required to hold the O-ring in place. For initial design purposes, a 1/16 in. diameter cross section is selected for the O-ring to seal against the bullnose skin hole wall.

On the other hand, the polysulfide sealant is chosen for injection molding due to the high costs associated with an O-ring option. To create the O-ring groove, additional side-pulls would be required, increasing mold manufacturing time by an average of 65 hours per side-pull (Boothroyd et al. 2002).

Finally, for both sealant systems, thermal expansion and contraction stemming from flight conditions and air supply temperatures should be considered to maintain a successful seal. Without sufficient knowledge of the thermal expansion coefficients for the skin, actuator material, and sealant system, this portion of the design remains to be solved.

5.2.3 Nozzle Profile Extension/Actuator Detachment Method from Wing Skin

With only one motion required to slide the bullnose over an actuator or an array of actuators, the same motion in the opposite direction is sufficient to separate the actuator from the skin. To reiterate, structural attachment to the skin is not considered due to the lack of structural support provided by the skin. Thus, the only force required for assembly and disassembly should be equivalent to the frictional force that acts between the sealant system and the sides of the hole wall. Table 5.5 summarizes the discrete design options in a morphological chart.

Table 5.5. Morphological Chart for DP 2

Function	Solutions		
NPE-Skin Cut	 With knifedge	 Without knifedge	
NPE-Skin Hole Shape	 Oval	 Square	 Trapezoid
NPE-Skin Sealing System	 Oring	 Gasket	 Standard Sealant
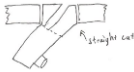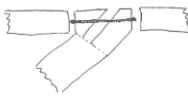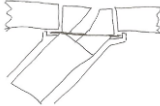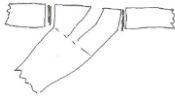
5.3 DP 3. Actuator-Structure Connection

5.3.1 Support Mount Design

From the model in Figure 5.3, shown again in Figure 5.16.a, a sense of the volumetric constraint is achieved. In the space between the actuator and the front spar, the support mount (SM) should support the actuator and withstand the associated loads. Since the SM can be integrated into the actuator to reduce the number of parts, per DFMA part reduction guidelines, the SM-Actuator attachment and detachment method (DP 3.1.2) will be discussed together. To explain the options and decisions associated with the design, the final design with the integrated SM is depicted in Figure 5.16.b.
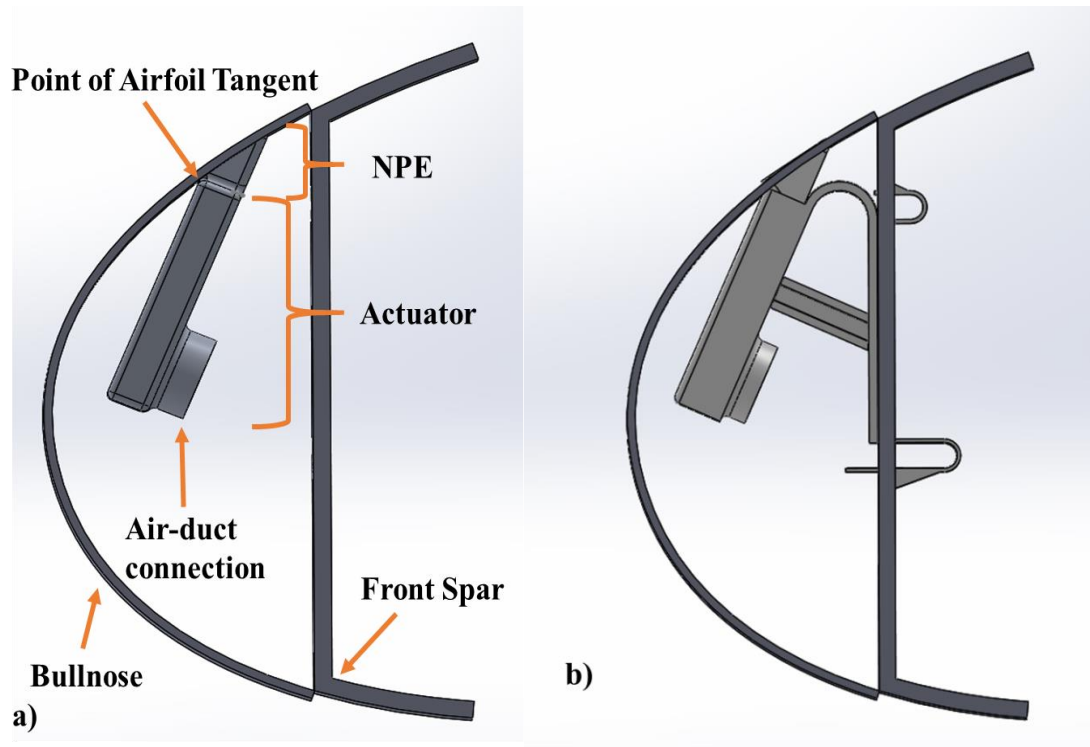
Figure 5.16. Side view of leading edge and actuator a) without SM and b) with SM

An angle bracket is selected as the basis for the SM (Figure 5.16.b) due to its injection moldable design and due to its ability to maintain the angle of the actuator with respect to the spar. The back plate, defined in Figure 5.17.a, could be an arch shape to better transmit loads to the spar with less material. However, a rectangular back plate design is a better option to reduce the number of fasteners, to be discussed later in this section. Additionally, another design option considered was locating the SM closer to the top of the spar versus closer to the bottom of the spar. The location was chosen at the top of the spar (Figure 5.16.b) to minimize the space and amount of material utilized. However, a design closer to the middle or bottom of the spar could move composite hole stress concentrations away from the spar flanges if necessary.
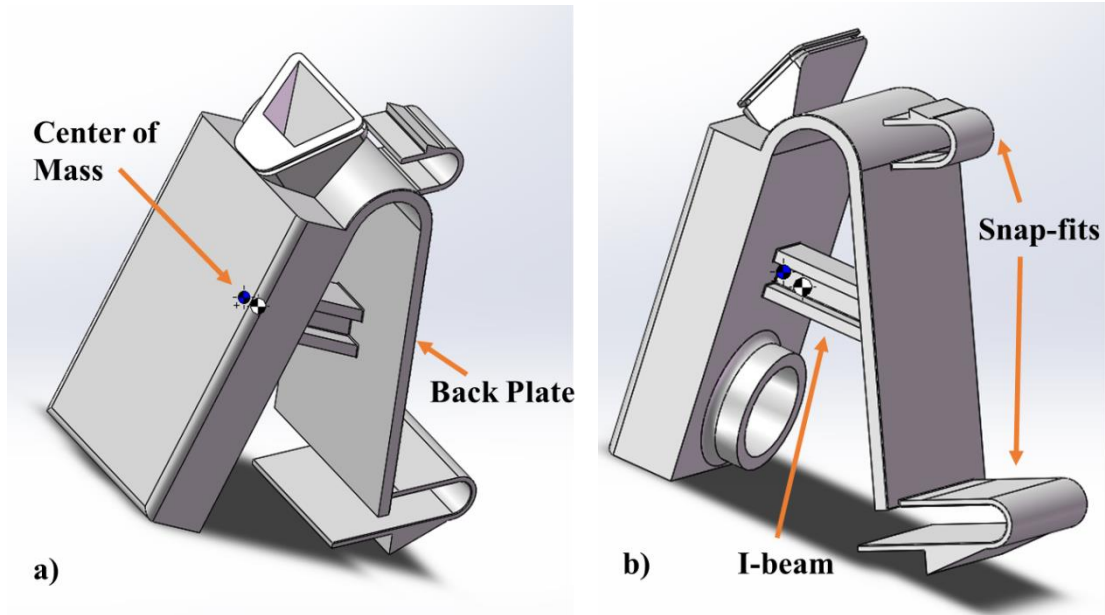
Figure 5.17. Integrated actuator, NPE, and SM design a) front, isometric view and b) back, isometric view

With thermoplastic material being used for the angle bracket design, a beam ought to be added for additional support. This beam should be located directly below the actuator's center of mass to most efficiently transmit the tensile and compressive loads to the spar. Potential beam designs included a thin wall, a rectangular or cylindrical beam, an I-beam, and a simple truss. The I-beam design was chosen due to its efficient use of material to withstand loads in any direction on the y-z plane (as defined in Figure 5.1), since insignificant loads are expected in the x direction and about the y or z axis (Assumption 6). Next, the thickness of the angle bracket and the I-beam are designed to be of similar thickness as the actuator wall thickness so that part distortion will be minimized after injection molding. In the model, this equates to 1/8 in. thick beam flanges and beam web. Finally, the designs assume that each individual actuator is supported by its own SM. In contrast, an array of actuators could be supported by a single SM that extends over the flap span, which might use more material but require less fastener holes as demonstrated in the morphological chart at the end of this section. However, this design option is forgone to reduce the scope of the project.

112

5.3.2 Support Mount Attachment and Detachment Method from Wing Structure

Regarding the SM-Structure attachment method, Constraint 4.2.2.9 requires the device to be removable. Thus, permanent chemical and physical joining methods, as discussed in section 4.3.2, are removed from consideration. Physically separate fasteners, thermal staking, and integrated fasteners are viable options, as DFMA assembly guidelines point out (Figure 4.5). However, the first two options increase part count and/or additional assembly equipment and thus the assembly skill required. Instead, given the SLS and injection molding manufacturing methods, it is more economical to select the third option, snap-fits, as the attachment method.

Of the possible snap-fit designs, a cantilever hook snap-fit is chosen for reasons mentioned in section 4.3.2, which requires either a slot or circular hole in the wall. Moreover, understanding the composite spar as the structure onto which the snap-fit is fastened, a milling operation is assumed to reliably cut a slot or circular hole (Assumption 1) as discussed in section 4.3.1. The trade-off would be that while a slot is a more complex shape to drill, only a minimum of two slots would be required to fasten the SM, whereas three or more smaller holes might be required for simpler circle shaped snap-fits. Without knowing which benefit to assign greater importance to, the decision between slot shaped holes and circular shaped holes is deferred to future designers.

For now, the specific U-shaped snap-fits (Figure 5.17) are chosen over the simple cantilever and L-shaped designs, since one of the advantages of a U-shaped design is that it will undergo less strain to achieve the same function (BASF Corporation 2007). Thus, a U-shaped design should account for the low allowable strain limit of 1% (specified in Table 4.4). However, following design guidelines, this necessitates the use of a slot shaped hole in the composite wall (BASF Corporation 2007). While it may be possible to create a U-shaped snap-fit with a circular design, this idea is not explored due to the complex nature of the issue.

From the U-shaped snap-fits, there are two design options (Figure 5.18); Design 1 (Figure 5.19.a) is chosen since it requires a lower force for disassembly, especially with a release tab. On the other hand, Design 2 (Figure 5.19.b) requires greater force for disassembly and would be more difficult to disassemble. The drawn on arrows represent the point where force ought to be applied to remove the snap-fit. In both cases, assembly and disassembly of the actuator can take place on the front side of the spar, which is advantageous in allowing the structural box to remain intact during the disassembly process.
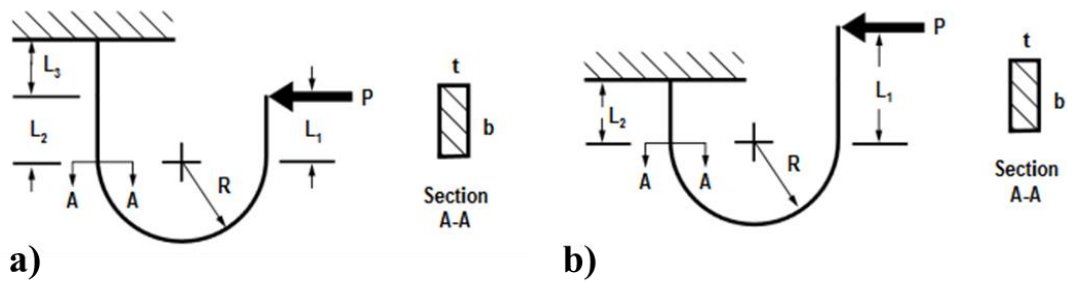
Figure 5.18. U-shaped Designs a) 1 and b) 2 (BASF Corporation 2007)
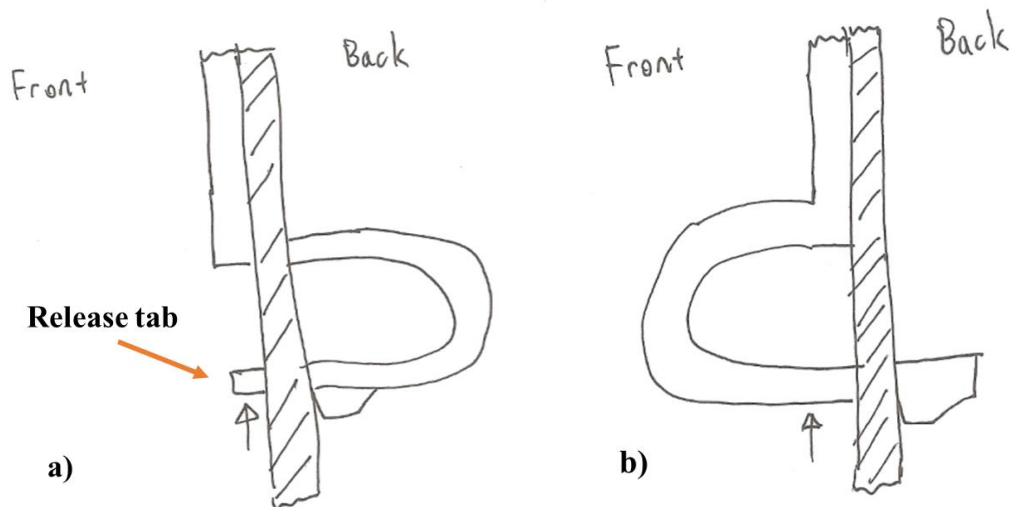
Figure 5.19. Manifestation of a) Design 1 and b) Design 2 attaching onto a spar (shaded in)

114

Taking into account the snap-fit design guidelines mentioned in section 4.3.2, the radii at the snap-fit corners are 0.03 in. to reduce stress concentrations. However, the snap-fits will relax in bending as opposed to relaxing in tension (Figure 4.9.b), since the U-shape cross section is oriented as seen in Figure 5.17 and gravity is assumed to act downward when the flap is stowed. The orientation is designed such that only two side-pulls are required for injection molding; were the snap-fits located on the left and right sides of the back plate to allow for relaxation in tension, a more complex mold design with additional side-pulls would be required. Finally, this design is not expected to undergo hundreds or thousands of full loading cycles, meaning the actuator is not expected to be assembled and disassembled thousands of times in its lifetime. Therefore, fatigue is assumed to be negligible.

Regarding the composite hole guidelines, one step is to reduce the number of holes drilled. Ideally, only one hole should be created in the spar to support the actuator. However, two holes are typically required to sufficiently leverage an object into place. The two holes are positioned at the top and bottom of the SM back plate to provide the maximum support and to prevent stress concentration around the holes from acting on each other. This decision then affects the back plate design, constraining the back plate shape to a rectangular design such that the snap-fits can be integrated at the top and bottom of the back plate, whereas an arch design for the back plate would require an additional hole to be created. Moreover, considering DFMA assembly guidelines, the two holes ought to incorporate an asymmetric design to aid in alignment during assembly. One parameter to vary is the length of the slots, so the bottom snap-fit is chosen to be longer since the I-beam is expected to transmit loads downwards on the back plate. This decision also allows for the same tooling to drill both holes, fulfilling the second composite hole guideline.

The final guideline to consider is to reduce the amount of material removed to create the hole. Without sufficient knowledge of the material or thickness of the spar,

however, this optimization problem remains for future design iterations. In the meantime, to design a first iteration of the U-shaped snap-fits, a ½ in. diameter drill bit was assumed to drill a 1.6 in. long bottom slot and a 0.8 in. long top slot into the spar, with an assumed spar thickness of 0.25 in.

Two equivalent equations describing the U-shape for Design 1 (Figure 5.18.a) are

$$Y_{snap} = \frac{\epsilon_0}{3(L_1 + R_{snap})t_{snap}} \left[4L_1^3 + 2L_3^3 + 3R_{snap}\{L_1(2\pi L_1 + 8R_{snap}) + \pi R_{snap}^2\} \right] \quad [in.]$$

(5.2)

and

$$Y_{snap} = \frac{P_{snap}}{6E_{bend}I_{snap}} \left[4L_1^3 + 2L_3^3 + 3R_{snap}\{L_1(2\pi L_1 + 8R_{snap}) + \pi R_{snap}^2\} \right] \quad [in.] \quad (5.3)$$

where L_1, L_2, L_3, R_{snap}, t_{snap}, and b_{snap} are the respective lengths, radius, thickness, and beam width defined in Figure 5.18.a. Y_{snap} is the maximum deflection required in direction of force, ϵ_0 is the allowable strain of the material, E_{bend} is the flexural modulus, and P_{snap} is the force acting on the point as seen in Figure 5.18.a. Finally, I_{snap} is the area moment of inertia, where

$$I_{snap} = \frac{b_{snap}^3 t_{snap}}{12} \quad [in^4]$$

(5.4)

with t_{snap}, and b_{snap} defined above.

Equating Eq. 5.2 and Eq. 5.3, it is possible to solve for $P_{snap,bottom}$ (Figure 5.20.a) and $P_{snap,top}$ (Figure 5.20.b) as a function of L_1 given the allowable strain from Table 4.4 ($\epsilon_0 = 0.01$), assuming the flexural modulus is equivalent to the elastic modulus ($E_{bend} \equiv E_{elastic} = 900\ Ksi$) (Table 4.4), assuming the composite spar thickness ($L_3 = 0.25\ in.$), and constraining the thickness of the snap-fit ($t_{snap} = \frac{1}{16}\ in$). Additional required variables are the radius and the beam width. Since the radius is the difference between two times the thickness of the snap-fit (1/16 in.) and the composite hole diameter (0.5 in.), $R_{snap} = 0.1875\ in$. Finally, with the slot lengths of 1.6 in. and 0.8 in., two beam widths are used for solving P_{snap} for the respective bottom and top

snap-fits: $b_{snap,bottom} = 1.6\ in.$ and $b_{snap,top} = 0.8\ in.$ At the same time, these values

can be used to solve for the maximum deflection as a function of L_1 from Eq. 5.2, which

are the same for both the bottom and top snap-fits (Figure 5.21)

a)

b)
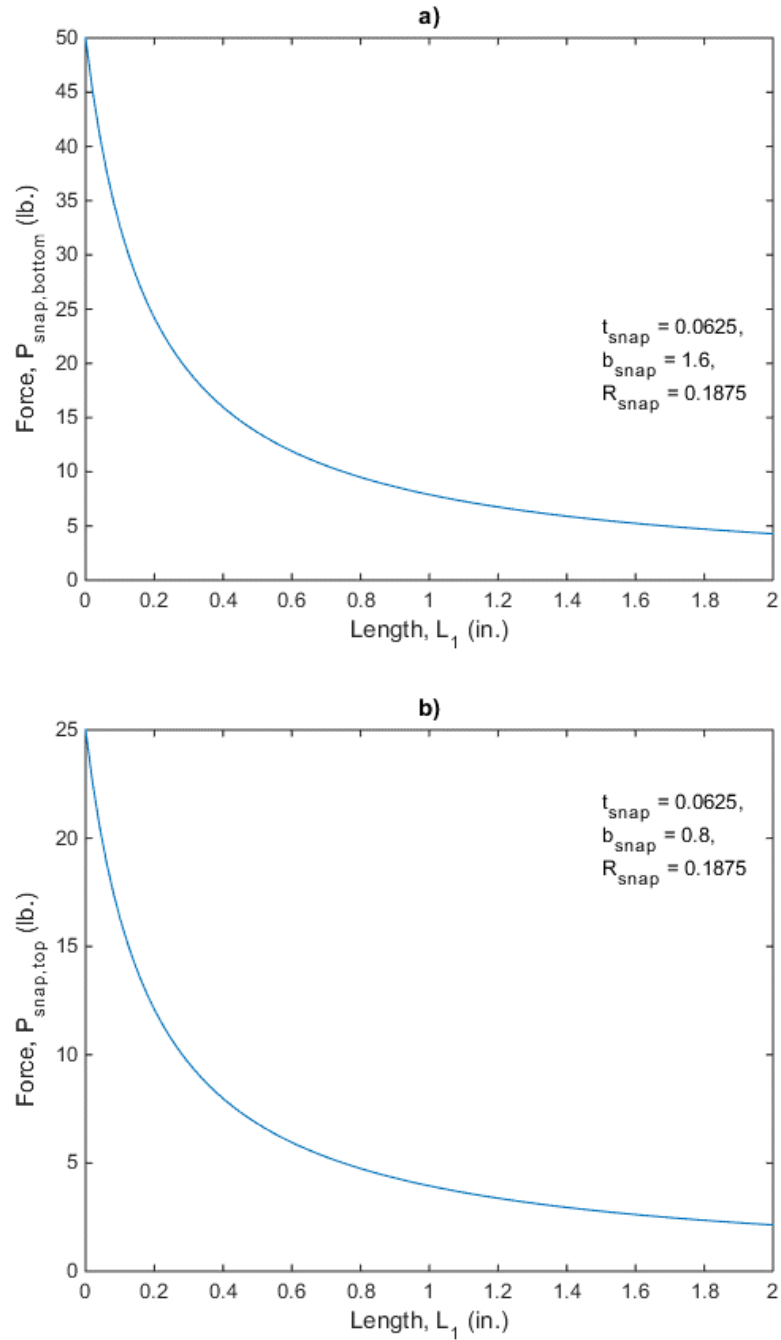
Figure 5.20. Force a) for the bottom snap-fit (P_snap,bottom) and b) for the top snap-fit (P_snap,top) as a function of length (L₁)
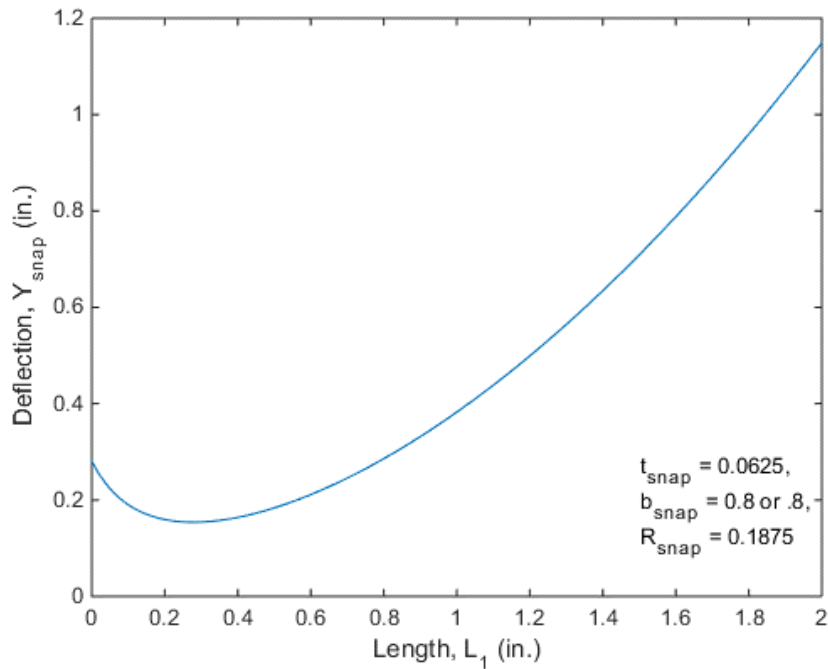
Figure 5.21. Deflection (Y$_{snap}$) as a function of length (L$_1$)

Studies conducted by Mathiowetz et al. (1985) demonstrate that the average "palmer pinch" (pinching with thumb pad to pads of index and middle fingers) force for both hands was ~22 lbs for all adult men and ~16 lbs for all adult women. Since the U-shaped snap-fit is conducive to a palmer pinch motion for assembly/disassembly, the force required, P_{snap}, is constrained at around 10 lbs to allow for manual assembly/disassembly while preventing accidental disassembly. Additionally, the composite hole size constrains the maximum deflection available, which is $2 * R_{snap} = 0.375\ in$. Accounting for the release tab that also lifts up within the hole, the amount of deflection should be slightly lower. However, the overhang depth as defined in Figure 4.9.c can be reduced to decrease the deflection required for assembly/disassembly, which, in turn, decreases P_{snap}. Finally, length L_1 should be minimized to reduce the amount of material required. Therefore, to remain within these self-imposed bounds, 0.75 in. and 0.5 in. were selected as L_1 for the bottom and top snap-fits, respectively, from Figures 5.20

118

and 5.21 and are represented in Figure 5.17. These dimensions result in $P_{snap,bottom} =$
10 lbf and $P_{snap,top} = 6.82$ lbf, which should be the force required to depress the snap-
fit and remove the entire design. The disassembly procedure can be accomplished
manually via a pinching motion or with the aid of a lever to depress the snap-fit.

According to Figure 5.22, assembly force can be calculated with

$$W_{snap} = P_{snap} \frac{\mu + \tan(\alpha)}{1 - \mu \tan(\alpha)} \quad [lbf] \tag{5.5}$$

where P_{snap} is as defined above, μ is the coefficient of friction, α is the angle at the
entrance side, and W_{snap} is the mating force. From discussion with engineers at RTP
Company, it is known that PEEK has similar high strength material properties to PEKK.
Thus, assuming a PEEK material coefficient of friction $\mu = 0.35$ (Assumption 4)
(Dotmar n.d.), designing $\alpha_{bottom} = 20°$ and $\alpha_{top} = 25°$, and given $P_{snap,bottom}$ and
$P_{snap,top}$ from above, $W_{snap,bottom} = 8.18$ lbf and $W_{snap,top} = 6.65$ lbf. Summing up
both forces, 14.8 lbf is theoretically required to slide the entire design into place.
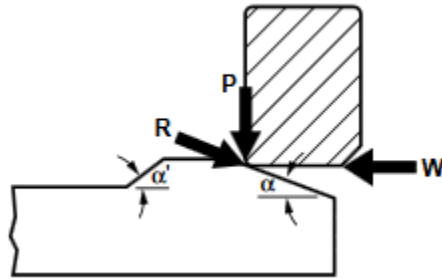
Figure 5.22. Snap-fit forces (BASF Corporation 2007)

To fully test the snap-fits against the expected loading conditions, a force-body
diagram was created (Figure 5.23), simplifying the actuator, NPE, and SM into a single
box. It is possible to assume forces only act in the y-z plane according to Assumption 6,
where forces in the x direction and about the y or z axis are assumed to be negligible.
Instead, only three forces are expected to act on the actuator: g-force (F_g), lift (F_L) acting

on the area exposed to freestream, and a reaction force (R_J) from the jet of expelled air. A maximum of 9 g's acts on the design according to Constraint 4.2.1.5, which, for the purposes of this problem, will act in the downward direction to incorporate the force of Earth's gravity. The lift force is simplified so that the direction it acts on is perpendicular to the front face. Finally, the air-duct connection is assumed to be located at the back to ignore losses associated with the pipe bend and to simply the problem for the reaction force. Vibrational forces were not considered due to a lack of information regarding these forces in the flap.
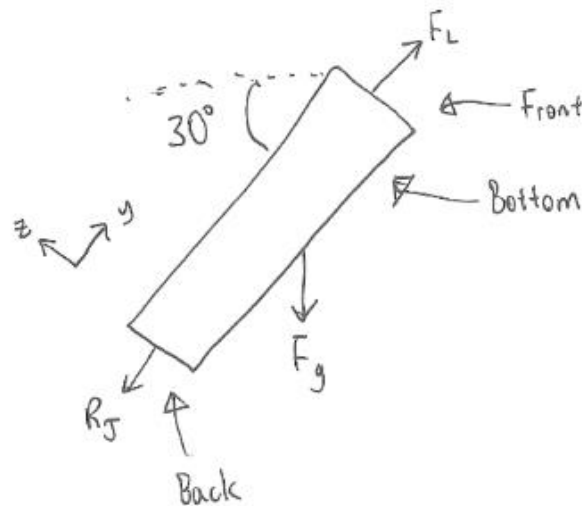
Figure 5.23. Force-body Diagram in y-z plane

For F_g, weight is calculated by multiplying the density of the material when using SLS (1.38 g/cc = 0.0499 lb/in^3)[16] by the volume (6.64576 in^3) to obtain a weight of 0.331 lb. Multiplying the weight by nine returns the resultant force, $F_g = 2.97\ lbf$.

---

[16] Private Communication with Boeing

Next, to solve for F_L, the following equation is used:

$$F_L = \frac{1}{2}\rho_{air}v_{TAS}^2 S_{NPE} C_{Lift} \quad [lbf] \tag{5.6}$$

where ρ_{air} is the density of air, v_{TAS} is the true air speed, S_{NPE} is the surface are of the

NPE exposed to freestream, and C_{Lift} is the coefficient of lift. Assuming Boeing 747

takeoff and sea level conditions, $\rho_{air} = 0.0023769\frac{slug}{ft^3}$ and $v_{TAS} = 180\ mph = 264\frac{ft}{s}$

(Scott 2002). From DeSalvo (2015), with a fowler flap model, $C_{Lift} = 2.22$ for flap

deflection at 42°. Finally, for a trapezoidal shaped NPE design, $S_{NPE} = 0.60766\ in^2 =$

$0.0042199\ ft^2$ (Figure 5.24). Solving for the lift, $F_L = 0.426\ lbf$, which is an order of

magnitude lower than F_g.
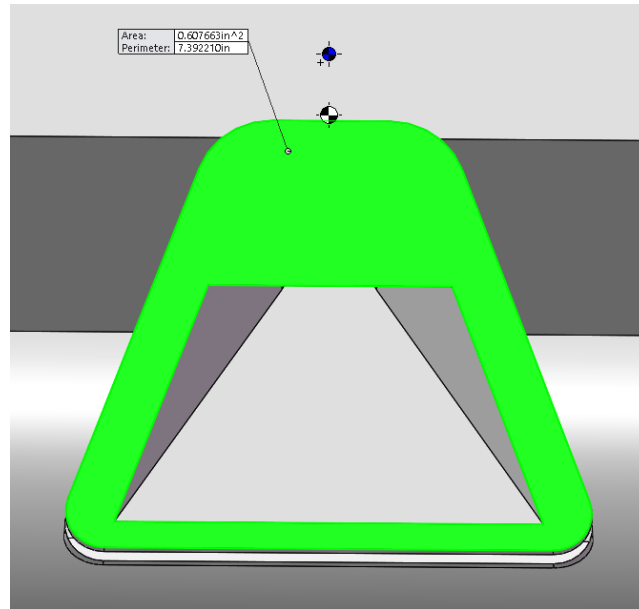
Figure 5.24. Surface area (0.60766 in^2) of Nozzle Profile Extension exposed to freestream, front view

The final force to solve for is the reaction force, which is solved by subtracting

the pressure force from the total force using continuity and Bernoulli equations (Figure

5.25.a). Simplifying the control volume to that shown in Figure 5.25.b, neglecting

frictional losses and weight of air, and assuming a horizontal nozzle and atmospheric pressure,

$$R_J = -\left(\rho_{air}Q^2\left(\frac{1}{A_2} - \frac{1}{A_1}\right) - \frac{\rho_{air}Q^2}{2}\left(\frac{1}{A_2^2} - \frac{1}{A_1^2}\right)A_1\right) \quad [lbf] \qquad (5.7)$$

where ρ_{air} is as described for Eq. 5.5, Q is the volumetric flow rate, and A_1 and A_2 are defined as the areas at the entrance and exit, respectively, in Figure 5.25.b.
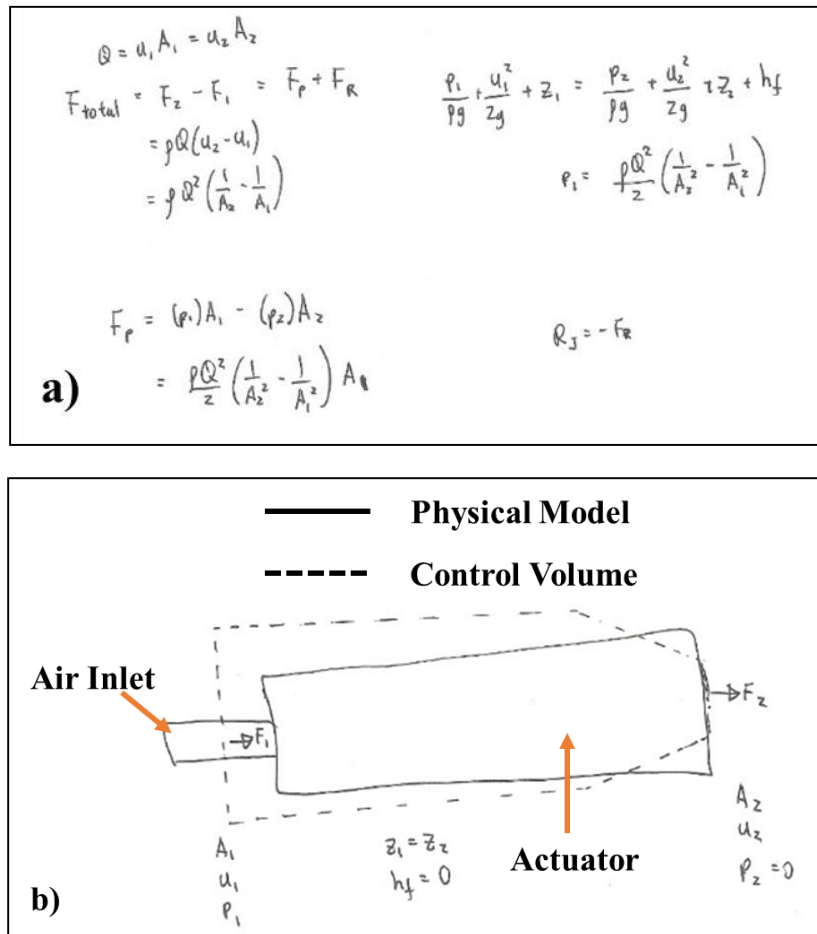
Figure 5.25. Jet reaction force problem a) equations and b) diagram (not drawn to scale)

With $\rho_{air} = 0.00237769\frac{slug}{ft^3}$, $Q = 150\frac{L}{min} = 0.08829\frac{ft^3}{s}$ (from successful experiments in chapter 3), $A_1 = \frac{3}{4}in^2 = 0.0052ft^2$ (from Constraint 4.2.2.6), and $A_2 =$

$0.0424 in^2 = 2.944 * 10^{-4} ft^2$, $R_J = 0.4958\ lbf$, which is an order of magnitude lower than F_g. In reality, the reaction force will likely be much lower with a smaller air-supply area.

Assuming R_J and F_L are negligible due to the lower order of magnitudes, only F_g is simulated on the model (Figure 5.26.a), which is composed of two parts. The first part (Part 1) is the integration solution design of the actuator, NPE, and SM that utilizes material properties from Table 4.4, while the second part (Part 2) represents the spar with simplified rectangular slots to improve convergence of the solution. Assuming that Part 1 fails before the composite spar (Assumption 7), all surfaces of Part 2 are constrained in all directions and modeled as a high strength material to emulate a highly rigid structure. To simulate F_g, 289.57 ft/s^2 (9 g's) was applied on the entire model in the positive and negative y' and z' directions (Figure 5.26.b). These directions were chosen to represent maximum shear, tensile, and compression stresses on the fastener, which are possible given a range of flap deflection angles. The areas of contact have a refined mesh size for more accurate results; a Pure Penalty contact formulation method assuming frictionless contact was used with aggressive stiffness updates for each iteration and with a pinball detection region using an auto-detection value. FEA simulations were accomplished via ANSYS Workbench R15.0.
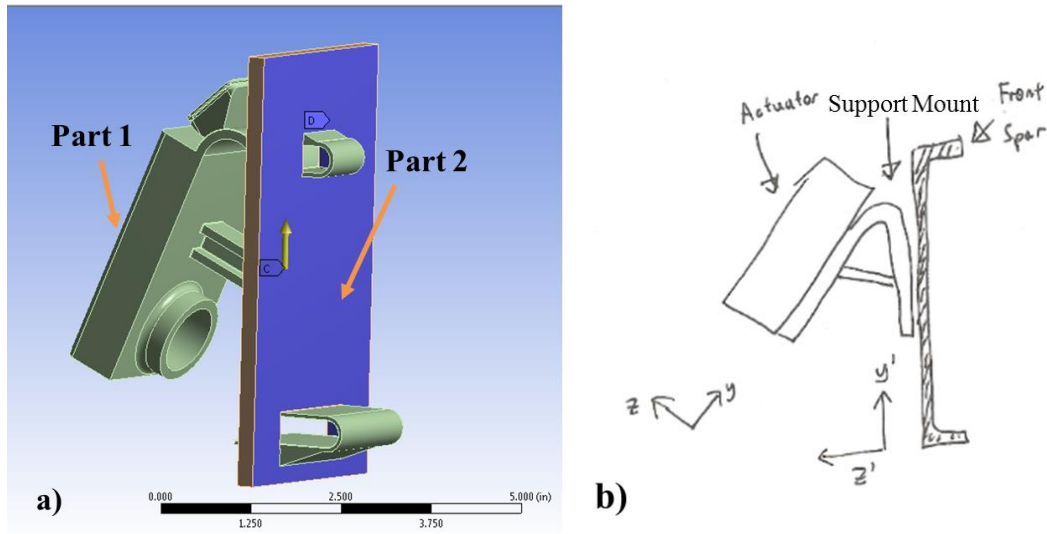
Figure 5.26. a) Isometric, back view and b) side view of simulation model

Results demonstrate that stress and strain concentrations primarily manifest at the interface between the snap-fit beams and the back plate (Figure 5.27), which was expected from section 4.3.2. Additionally, in all four loading condition, the bottom snap-fit experienced slightly higher stresses and strains than the top snap-fit (Figure 5.27.a), as noted from the composite hole discussion in section 5.3.1. Nonetheless, maximum stresses and strains for all four conditions were at least three orders of magnitude below allowable limits (Table 5.6). This demonstrates that the proposed snap-fit fastening mechanism is able to withstand expected loads, thus validating the design as a best design concept (BDC). If any additional, significant forces are determined to act on the design at this location, possible solutions include increasing the I-beam thickness or number of beams for stronger support, increasing the snap-fit thickness or width for more secure fastening, or expanding the back plate in the x direction to dampen potential vibration. Table 5.7 summarizes the design options in a morphological chart.
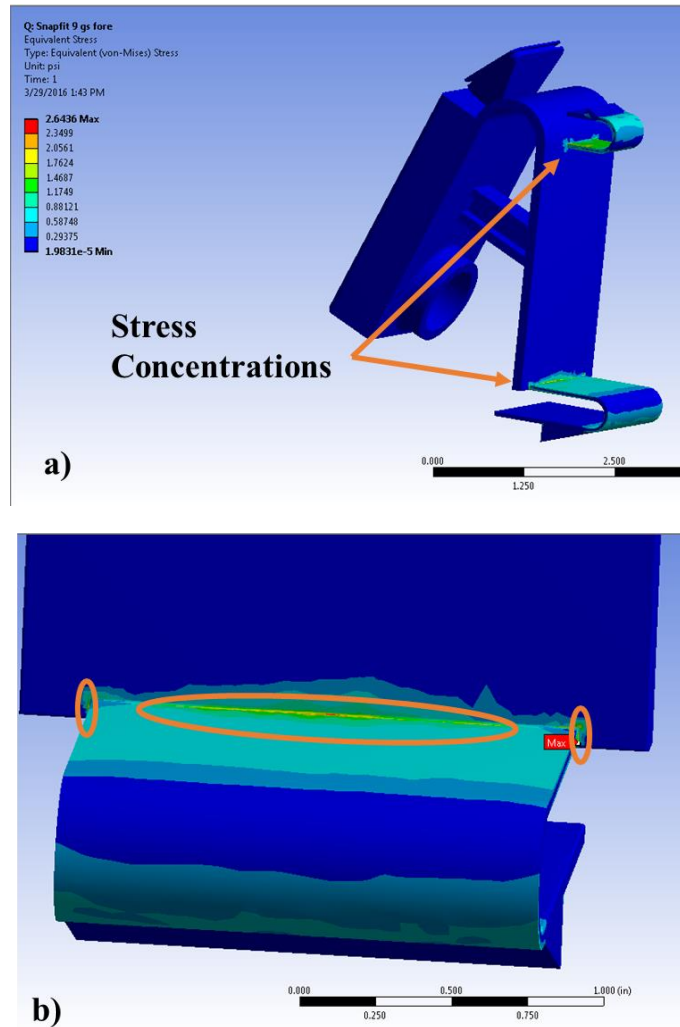
Figure 5.27. Stress and strain concentrations a) isometric, back view and b) bottom snap-fit, back view

Table 5.6. Results for expected loads

	z' (fore)	-z' (aft)	y' (up)	-y' (down)	Allowable Values
Maximum Total Deformation (in)	2.19E-07	2.01E-05	2.10E-05	2.01E-05	-
Maximum Equivalent Elastic Strain	3.24E-06	3.22E-06	3.34E-06	3.14E-06	0.01
Maximum Equivalent von Mises Stress (psi)	2.64	2.62	2.73	2.54	8702

Table 5.7. Morphological chart for DP 3

Function	Solutions			
SM-Actuator Connection	One Piece	Mechanical	Adhesive	Weld
SM Location	Top	Bottom		
Support Mount Beam	Flat Wall	I-Beam	Truss Structure	
Support Mount Back Plate Shape	Rectangle	Arch		
Multiple SM Design	Single	Array		
Support Mount-Structure Connection	Mechanical	Adhesive	Combination	
Support Mount-Structure U-shaped Snap-fit	Design 1	Design 2		

5.4 Best Design Concept Model Creation

The 3D computer-aided design (CAD) model of the BDC was created in SolidWorks 2015. Using the actuator as the reference point for all other features, the actuator thickness was first optimized to withstand the expected internal pressure. Next, the Nozzle Profile Extension (NPE) was created with five main steps (Figure 5.28). The centerline splits the NPE into two mirrored parts, of which only one part will be depicted in the following figures.
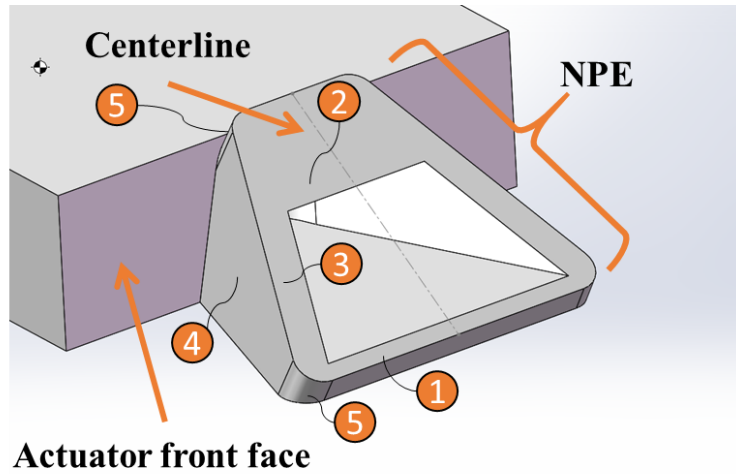
Figure 5.28. Front isometric view of NPE

First, the actuator was positioned in a CAD model of the flap structure (Figure 5.29). Understanding that the optimized actuator thickness manifests as dimension A (nominally 0.1426 in.) in Figure 5.30.a, dimensions C and D (dashed lines in Figure 5.30.b) can be measured with respect to the skin curvature to determine the distances required for the NPE to extend out to freestream.
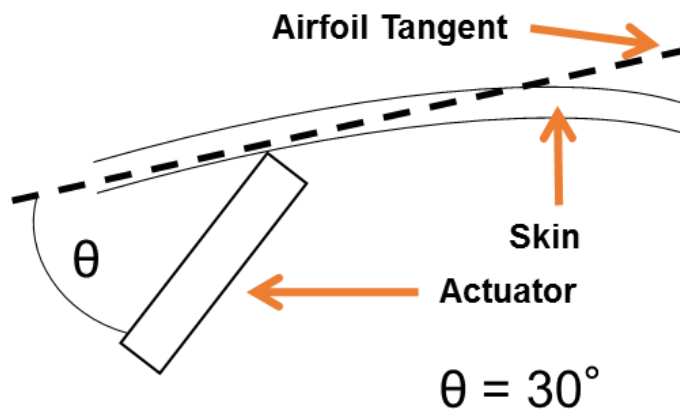
Figure 5.29. Side view of actuator-skin interface
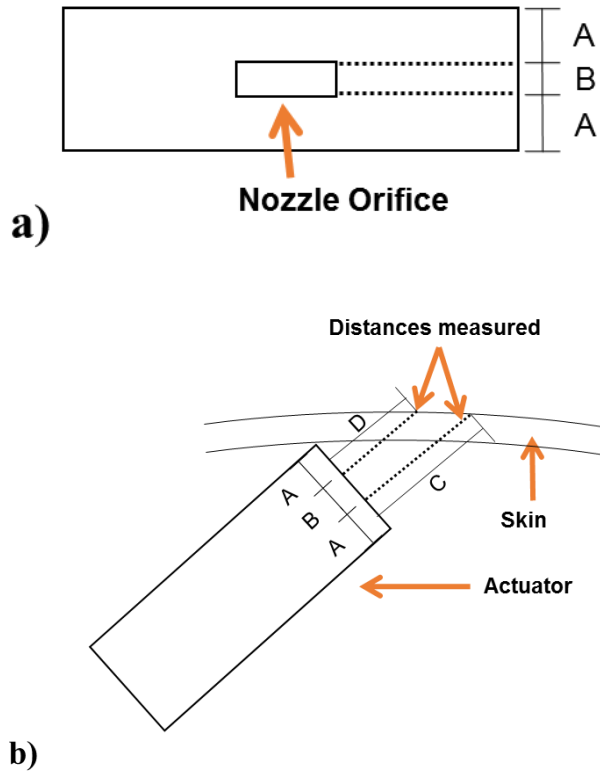
Figure 5.30. a) Front view of actuator and b) side view of actuator-skin interface

The azimuthal angle of the nozzle orifice was extended for dimension C to create feature 1 (Figure 5.31.a) and similarly extended for dimension D to create feature 2 (Figure 5.31.b).
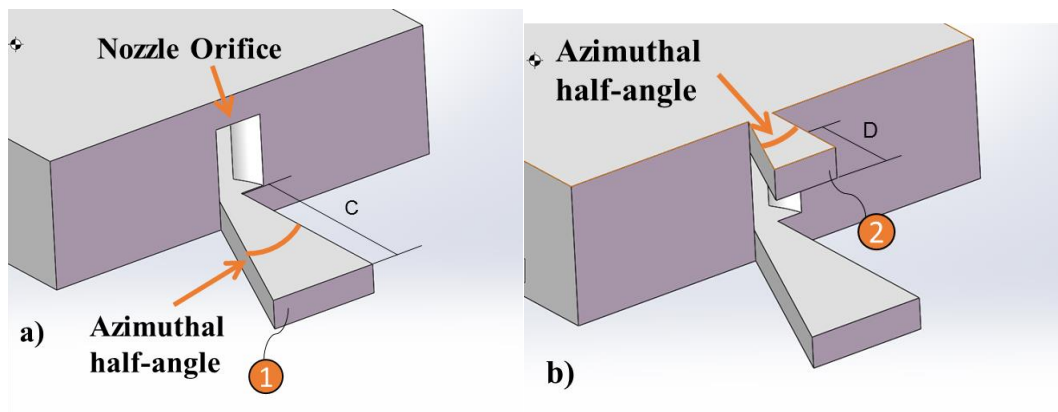
Figure 5.31. Front isometric view of extended a) dimension C and b) dimension D

Next, a side wall (feature 3) was created to bound the flow (Figure 5.32).
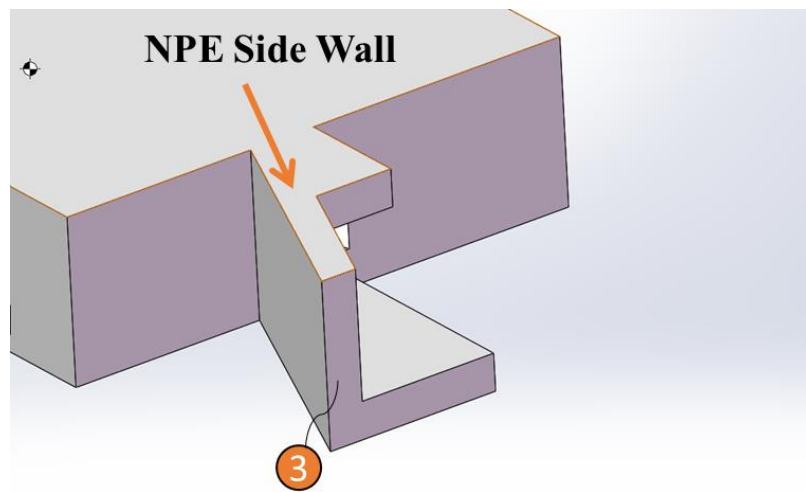
Figure 5.32. Front isometric view of side wall addition

The side profile was then extruded and trimmed in certain places to match that of the shaded feature in Figure 5.33.a; the resulting shape is depicted in Figure 5.33.b. At the same time, the side wall, defined in Figure 5.32, was extruded and trimmed such that the feature (4) could fit into a hole milled normal to the working surface. Throughout the entire process, similar wall thicknesses are used to reduce part distortion during injection molding.
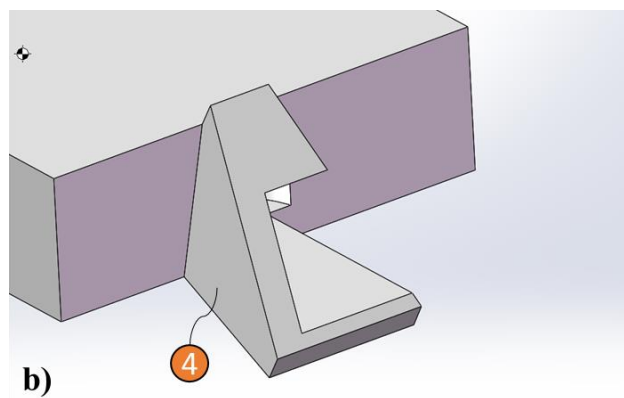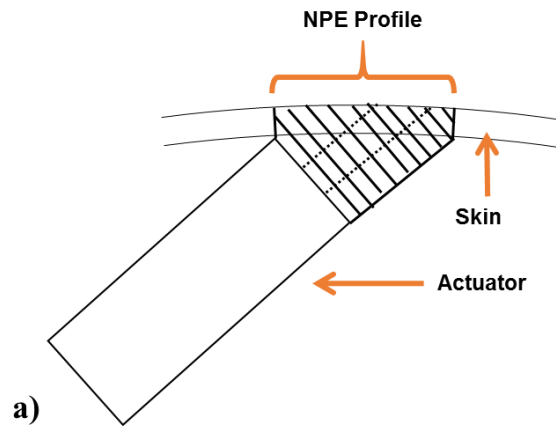
Figure 5.33. NPE a) side view and b) front isometric view

Finally, the NPE was mirrored across the centerline (Figure 5.34.a) and fillets (feature 5) were applied on corners of the NPE design, shown both without and with an O-ring groove (Figures 5.34.b and 5.34.c respectively).
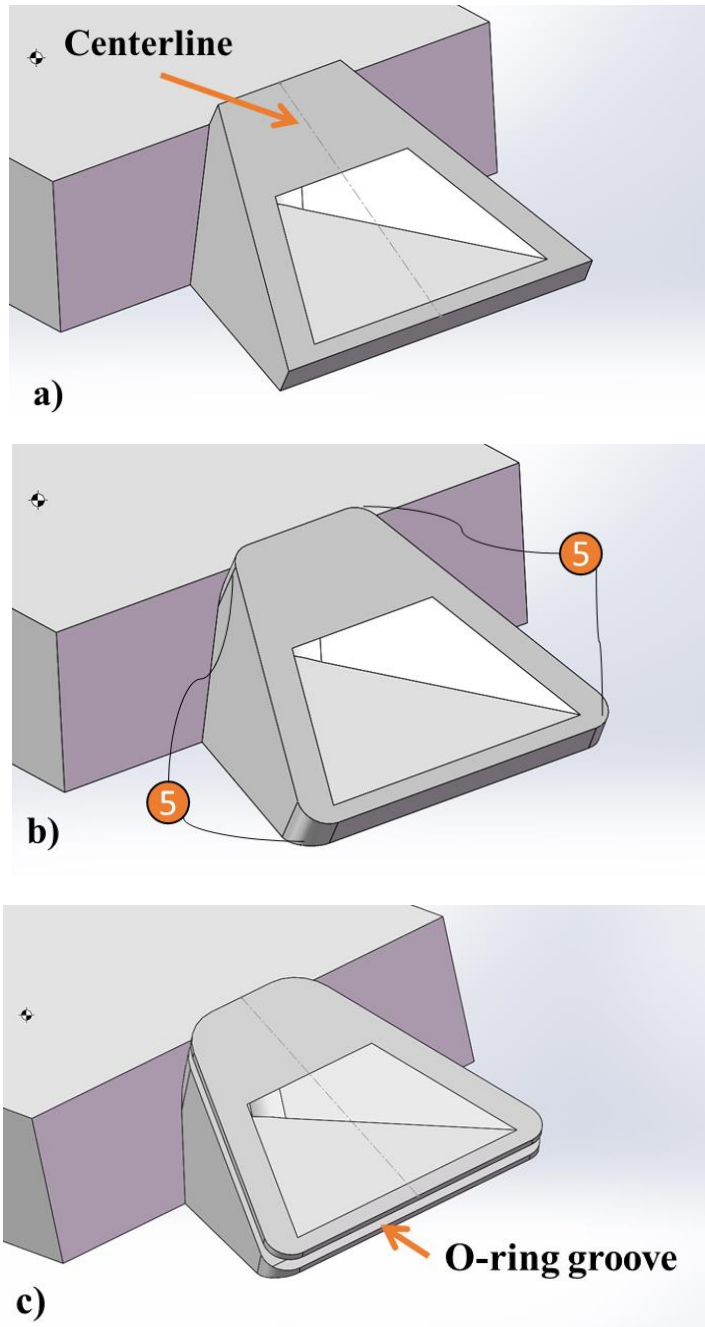
Figure 5.34. Front isometric view of the NPE with a) no fillets, b) fillets and no O-ring groove, and c) fillets and an O-ring groove

With the actuator positioned appropriately (Figure 5.35.a), the corresponding

Support Mount (SM) was created by extruding the bottom face of the actuator into the

angle bracket shape (Figure 5.35.b) with an I-beam located directly underneath the center of mass (Figure 5.35.c).
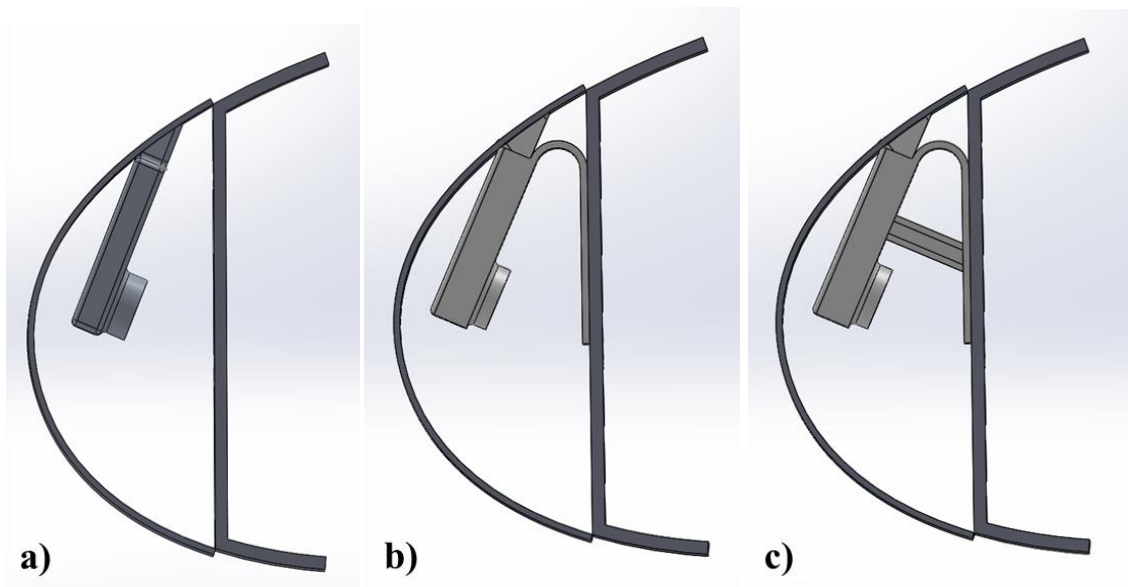
Figure 5.35. Side view progression of SM with a) actuator, b) angle bracket, and c) I-beam support

Lastly, U-shaped snap-fits were designed in at the bottom and top of the back plate to produce the BDC seen in Figure 5.17.

5.5 Final Designs

Returning to Figure 4.2, the next step is to design for manufacturing method using the proposed BDC (Figure 5.17). In doing so, the design can be optimized further to increase its cost effectiveness. Thus, two design concepts can be created: one assuming an SLS manufacturing method (Design 1) and the other assuming an injection molding manufacturing method (Design 2). It is apparent that the benefits of Design 1 include being created in one part and flexibility in adjusting the design to accommodate varying parameters such as thickness of the bullnose skin or spar, whereas Design 2 requires a minimum of two parts and would significantly increase capital costs if a design

adjustment were required. On the other hand, the main benefit of Design 2 is the high production rate of an accurate and precise design at a low cost, whereas Design 1 maintains a higher cost at high production rates. However, a third design (Design 3) can be created that utilizes both SLS and injection molding to take advantage of both Design 1 and Design 2 benefits. Thus, in this section, three final designs will be discussed.

5.5.1 Design 1: SLS Manufacturing

Design 1 is as depicted in Figure 5.17, with SLS being able to sinter the entire design in one piece. Before further design changes take place, the actuator wall thickness should first be optimized to account for the specific material and the orientation in which the powder is sintered. With an altered wall thickness, the NPE and thus hole size in the skin will be affected similarly, as discussed in section 5.1.2.

With hollow sections, un-sintered powder will need to be removed. Thus, nested pull rings, hooks, and chains can be created along with the device to aid in the powder removal process, especially from internal corners. These nested tools should be avoid being placed in areas critical to successful jet oscillation, such as the nozzle; the remaining location for the tools is the air-duct connection feature (Figure 5.36). Additionally, the O-ring groove can be modified to create a negative draft angle that better secures the O-ring (Figure 5.36).
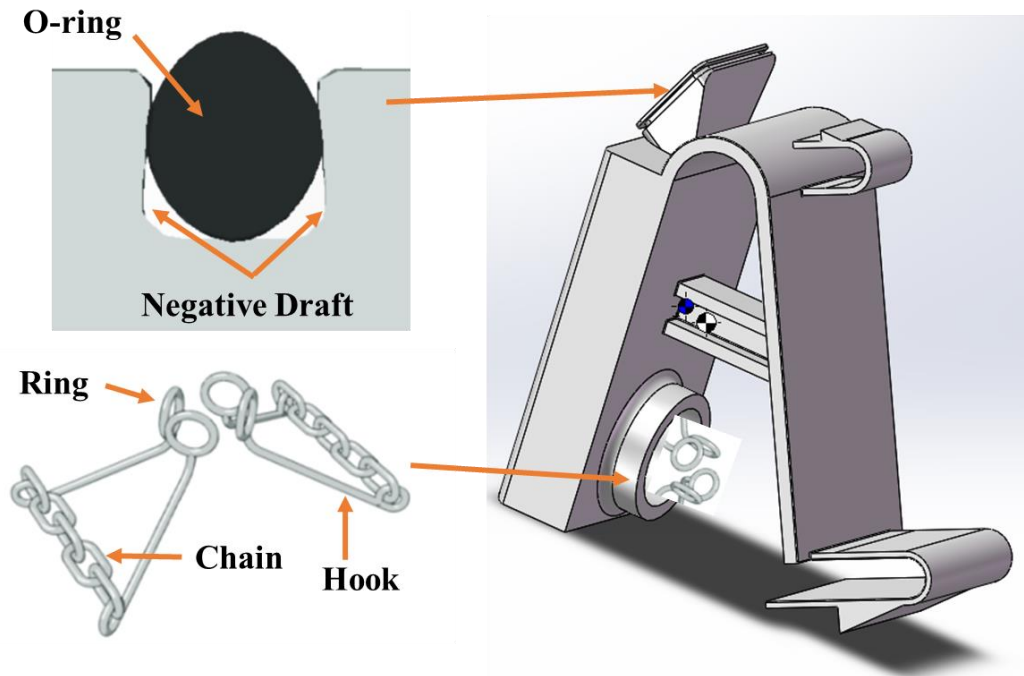
Figure 5.36. Design 1 (insets from 3D Systems Quickparts 2013)

Finally, a feature that could be completely redesigned is the support beam on the SM. Since this internal area of the angle bracket is not constrained by injection molding techniques, any type of support beam design can be manufactured. In particular, a truss or lattice support beam design may be more efficient in terms of weight-to-strength ratio, with lattice strut diameters down to 0.5 mm able to be manufactured (3D Systems Quickparts 2013).

5.5.2 Design 2: Injection Molding Manufacturing

Design 2 has a minimum part count of 2: a top cover to enclose the internal fluidic design, and a bottom part with the engraved fluidic design and integrated NPE and SM (Figure 5.37). Although it is possible to injection mold the design as one part with a living hinge as in Figure 2.15, the low allowable strain value of the material (Table 4.4) eliminates the hinge as an option. As such, a joining method is required to both fasten and seal the two parts. From section 2.3.3, direct and indirect bonding methods have proven

to successfully join fluidic oscillator parts. Next, understanding polyetheretherketone (PEEK) to have similar material properties to PEKK[17] (Assumption 4), localized welding (e.g., ultrasonic welding, microwave welding) is selected from a table of bonding methods that compare advantages and disadvantages (Table A.1) (Tsao and DeVoe 2009). Moreover, ultrasonic welding is a good economic method, typically used to join injection molded parts in about 2 s (Boothroyd et al. 2002). Therefore, ultrasonic welding is selected as the joining method for the two parts.
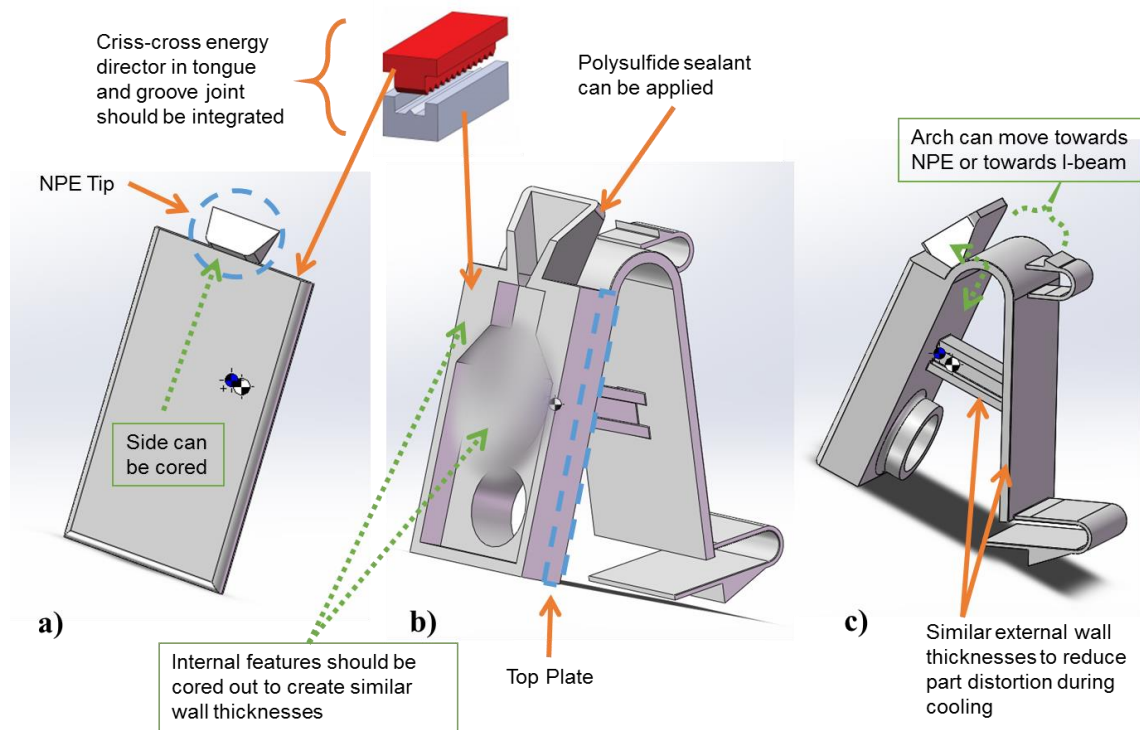
Figure 5.37. Design 2 a) top part, b) bottom part, and c) welded together (inset from Branson Ultrasonics Corporation 2013)

---

[17] Private Communication with RTP Company

Following design guidelines for ultrasonic welding (Branson Ultrasonics Corporation 2013), a tongue and groove joint should be created between the two parts to ensure successful, repeatable alignment. Furthermore, a criss-cross energy director lining the tongue and groove joint will create an air-tight seal (Figures 5.37.a-b). Since the top cover wall thickness is a maximum of 0.1426 in., near-field welding is required ($< ¼$ in. horn contact from weld area), as opposed to far-field welding ($> ¼$ in. horn contact from weld area) (Branson Ultrasonics Corporation 2013). Finally, a specialized mount will be required to stably support Design 2 as it is being ultrasonically welded.

Next, wall thickness should be optimized, for material and mold flow orientation (which orients fibers), especially since injection molding allows for a stronger, isotropic material 30% carbon fiber reinforced PEKK[18]) to be used, with at least three times the elastic modulus and UTS than sintered 23% carbon fiber reinforced PEKK powder[19]. As discussed in section 5.5.1, wall thickness changes will affect other features down the line, including the NPE design, skin hole size, and wall thicknesses, as well as amount of material used and time to cool. In particular, once wall thickness is optimized, it is critical that all other part features maintain a similar wall thickness to minimize part distortion during cooling. While most features in Figure 5.37 are designed to meet this criteria, two areas, outlined in blue dashed lines, are designed slightly thicker. A third area includes internal features of the actuator that are designed to be solid (Figure 5.37.b).

The first outlined area (NPE tip) (Figure 5.37.a) is ~0.26 in. at its thickest point due to the 0.1426 in. thick actuator cover integrated with the NPE that is inserted through a 0.12 in. thick skin, whereas the second outlined area (top plate) (Figure 5.37.b) maintains a ~0.29 in. thickness due to the 0.1426 in. thick bottom actuator wall integrated

---

[18] Private communication with RTP Company
[19] Private communication with Advanced Laser Materials and Boeing

above the 0.1426 in. thick top plate. One potential solution for the NPE tip (Figure

5.37.a) is to core out parts of the side that would otherwise contact the skin hole wall,

with a side-pull. For the top plate, the bottom actuator wall could, instead, take the place

of the top plate, which would force a redesign of the angle bracket arch, either moving it

closer to the NPE or lower towards the I-beam (Figure 5.37.c). Finally, internal features

can be cored out to match the optimized wall thickness (Figure 5.37.b). All three

potential changes are noted by dashed, green lines.

Another guideline that aids in creating consistent wall thicknesses is incorporating

a certain radius at both internal and external corners (Figure 5.38), similar to the first

guideline mentioned for snap-fits in section 4.3.2. All external radii in the model maintain

a small radius according to this guideline. However, internal radii have not been modeled

due to unknown effects on internal air flow and external jet oscillation. Thus, further

experimentation, as recommended in section 3.4, should test for acceptable internal radii.
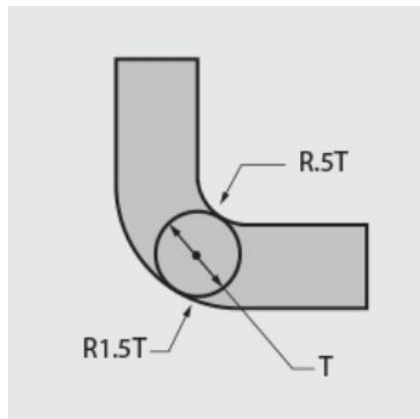
Figure 5.38. Guideline for consistent part thickness at corners

A final design guideline to mention pertains to draft angles of the part.

Appropriate tapers should be designed on the actuator walls, SM design, and snap-fit

fasteners to improve part removal and decrease mold wear. Once the drafts have been

designed in, loads should be simulated again to ensure the final design can withstand the expected internal pressure and the expected g-force.

An important feature to mention that results from Design 2 is the interface between the two parts on the NPE. Some tolerancing issues, such as an overhang, may appear at this location, which is critical due to its exposure to freestream. Therefore, either before or after flap assembly, the portion of the NPE that is exposed to freestream may require more post-processing processes compared to Designs 1 and 3. A potential solution would be to sand the area to smooth out any irregularities associated with the ultrasonically welded parts.

5.5.3 Design 3: SLS and Injection Molding Manufacturing

Since Design 3 includes two different manufacturing methods, there is a minimum part count of two: a sintered fluidic oscillator and an injection molded SM (Figure 5.39). As seen in Figure 5.39.a, the SLS manufactured part consists of the actuator and NPE integrated together with the air-duct connection on the bottom side. Therefore, the injection molded part requires a hole in the top plate of the SM through which to pass the connection feature. Although the lower half of the top plate (below the blue dashed line) could be completely removed, it should still remain in the design to support the bottom half of the actuator, to further prevent chatter, and to act as a guide to help locate the top part for successful assembly.
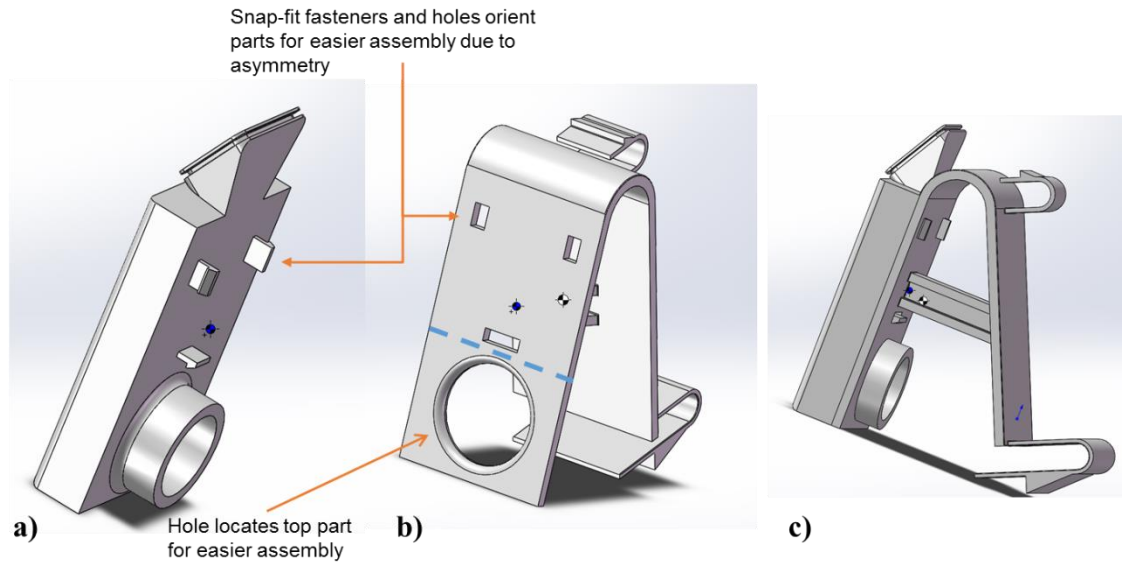
Figure 5.39. Design 3 a) SLS manufactured top part, b) injection molded bottom part, and c) fastened together

To assemble the two parts together, joining methods discussed in section 4.3.2 were considered. Per DFMA part reduction guidelines, snap-fits (Figure 5.39) were chosen as the fastening method due to low part count, reduced manufacturing and assembly procedures, and thus reduced manufacturing and assembly defects. However, other standardized joining procedures should be considered if they are more cost effective at quickly joining two parts of the same material, such as solvent adhesive or ultrasonic welding.

Since the snap-fits are located on the SLS manufactured part, any combination of size or design of snap-fits are possible, as long as they sufficiently support the actuator weight on the bottom part. Thus, a design of three height tapered snap-fits with uniform widths was selected to maximize the strength to weight ratio of the snap-fit and to create an asymmetric interface that orients the top part for successful and consistent fastening. Additionally, this design was selected due to its aesthetic similarities to a surprised face shape (:-O) and so that at least two snap-fits would relax in tension per snap-fit guidelines mentioned in section 4.3.2. Lastly, the snap-fits were selected to protrude from a location

closer to the middle of the actuator as opposed to protruding from the actuator edges to better transmit any vibrational or other loading forces to the SM. On the other hand, moving the snap-fit locations closer to the edges will reduce the maximum strain experienced by the snap-fits.

Next, as discussed for the first two designs, the wall thickness should be optimized, since it affects other design factors down the line, including the snap-fit lengths on the top part and the corresponding snap-fit hole sizes in the bottom part. Finally, due to the two different manufacturing methods of the different parts, tighter tolerances are required on each part to achieve the same overall tolerances that the first two designs maintain.

5.6 Chapter Summary

In section 5.1, the internal width and height were constrained before adding a circular air-duct connection feature on the bottom actuator face, which constrained the internal length, to allow for unobstructed access to the air supply. Next, after running finite element analysis (FEA) simulations, a wall thickness range of $1/16 - 0.1426$ in. was deemed sufficient. In the case of partial nozzle blockage, pressurized or heated air (McLean et al. 1999) should clear the opening. In the case of complete nozzle blockage, a leak-before-break criterion was met, assuming a 0.1426 in. wall thickness and PEEK material.

A recessed (DeSalvo et al. 2011) NPE design was selected such that a straight cut could be created in the bullnose skin while minimizing the distance the jet of air travels from the nozzle orifice to freestream. Additionally, the NPE was integrated into the actuator to reduce part count, allowing the actuator as opposed to the bullnose skin to support the NPE. This simple design should allow for the bullnose skin to slide on and off the NPE without any permanent attachment method. A trapezoid hole shape was selected to minimize the composite material removed, although an oval hole shape could

140

reduce maximum stresses and strains by 54% while spreading out stresses over a larger area with 101% more composite material removed, determined through FEA simulations. Other factors that affect hole size, including bullnose skin/actuator wall thickness, thermal expansion and contraction, and fiber sealing, were discussed. Finally, the sealant system options were reduced to either an O-ring or a standard sealant, depending on the typical sealant method (e.g., polysulfide sealant) used on aerospace structures.

The final SM part was integrated into the actuator to reduce part count and located closer to the top of the front spar to minimize space and material utilized. To maintain an injection moldable design and to maintain the 30 degree angle with respect to the airfoil tangent, an angle bracket was selected as the basis of the SM design; to efficiently transmit expected loads to the spar and to also maintain an injection moldable design, an I-beam was selected as a support beam directly below the actuator's center of mass.

For attachment of the SM to the spar, snap-fits were selected to reduce part count. Specifically, a cantilever hook snap-fit was selected to allow assembly and disassembly from one side of the composite spar. Furthermore, a U-shaped snap-fit design permits the strains experienced to remain under low allowable limits while maintaining higher separation forces than simple cantilever beams. Trade-offs between a slot hole shape and a circular hole shape were discussed.

A top and bottom snap-fit was designed for minimal number of composite holes (2) in the spar, constraining the rectangular back plate SM shape, and so that the tooling for the bullnose skin hole could be used for each of the spar holes as well. Finally, the snap-fits were designed to be located far apart to reduce stress concentration interactions and designed with different beam widths to easily orient the entire device for manual assembly, with reasonable mating force (14.8 lb) and seperation forces (10 lb for bottom snap-fit and 6.8 lb for top snap-fit). FEA simulations applying expected loading conditions on the entire structure validated the proposed snap-fit design as the fastener

for the SM, as well as validated the BDC as the amalgamation of the actuator, NPE, and SM.

Finally, the procedures to create the BDC CAD model are discussed, and the three design concepts of the BDC are presented along with how they ought to be manufactured and assembled. Preliminary trade-offs in flexibility, cost, and production rate are noted, which will be evaluated in further detail in the following chapter.

CHAPTER 6

PROCEDURES AND EVALUATIONS

From the best design concept (BDC), the necessary manufacturing and assembly procedures are extrapolated at the macro- and micro-scales to determine the fully integrated solution. Finally, manufacturing, assembly, material, and weight costs, as described in section 4.1.3, are calculated to evaluate the proposed designs. In the case of an alternate actuator design, corresponding changes to the model and costs are discussed.

6.1 Manufacturing and Assembly Procedures

First, for the macro-scale level of procedures, it is important to acknowledge the three parts of the flap that will interface with the BDC: the bullnose skin, the spar structure, and the air supply. The manufacturing and assembly steps required to integrate the BDC with the three parts are visualized in Figure 6.1. Starting from the top left corner, it is imperative that the holes in the bullnose and spar are accurately and precisely cut so that they line up with each other along the span. Alternatively, the holes can be accurately and precisely built up into the composite pieces as discussed in section 5.2.1, although it is not preferable[20]. This process may be improved by utilizing the same laser system to align holes in both the bullnose and the spar.

---

[20] Private Communication with Boeing
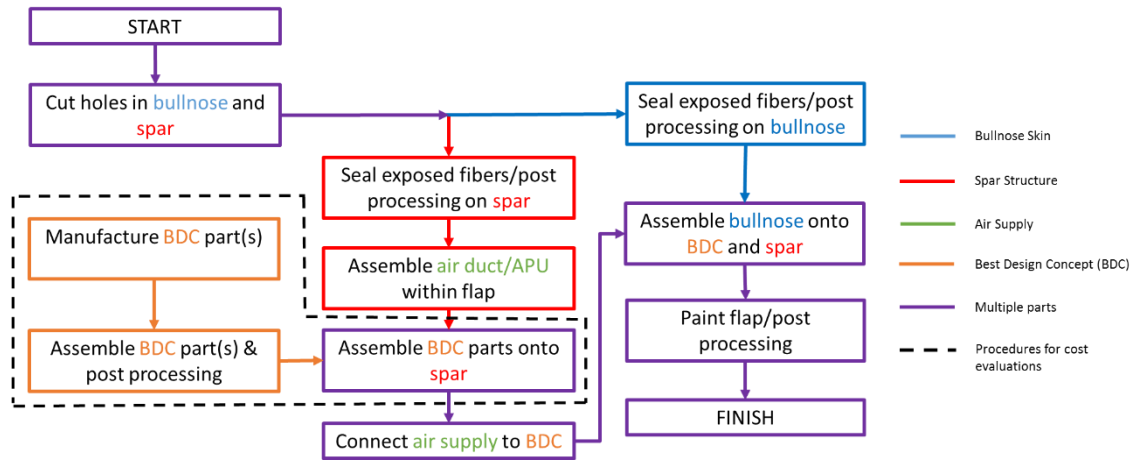
Figure 6.1. Required manufacturing and assembly procedures

Next, post-processing procedures, including de-burring, cleaning, and sealing the fibers, should be applied on both the bullnose and spar. From here, the spar should be assembled onto the main structural box so that the air supply system can be assembled within. Assuming that the access holes in the front spar are large enough to fit pipe/duct fittings through, these fittings should thread through the access holes to interface with the BDC.

As the bullnose and spar procedures occur, the parts for the BDC can be simultaneously manufactured. To improve the fit of the BDC, especially at the interface with the bullnose (i.e., a critical control surface), the hole thickness or even hole size in the bullnose and/or spar can be measured to manufacture the corresponding BDC interface(s), assuming SLS manufacturing. Once manufactured and assembled, post-processing procedures such as removing powder, sanding surfaces, and/or painting the internal surface exposed to freestream should be followed. The final part then should be attached onto the spar.

After the BDC attachment to the spar, the second interface (pipe/duct fitting) and the third interface (bullnose skin) should be assembled, respectively. Finally, post-processing of the entire flap can occur, including potential sanding of any significant protrusion as mentioned in section 5.5.2 and painting of the flap with the BDC nozzle

144

openings covered with a rubber plug, as opposed to masking it up[21]. Once the rubber plug is removed, internal BDC surfaces will still be exposed to the environment. However, the excellent UV resistance property of the material (Constraint 4.2.2.2) is assumed to be sufficient in resisting UV radiation. Additionally, it is possible to paint the internal surface of the BDC prior to assembly onto the spar as mentioned above.

With the outline of the macro-scale procedures, a portion of micro-scale level of procedures, outlined in the dashed black lines (Figure 6.1), can be examined in the context of evaluating Designs 1, 2, and 3 from section 5.5. The expected parts and assembly procedures for each design are summarized in Table 6.1. Thus, as described in section 4.1.3, manufacturing, assembly, material, and weight costs will be calculated for all micro-scale procedures. In the end, temporal costs will be converted to monetary costs to visualize total costs; all designs are assumed to have a wall thickness of 0.1426 in. (Assumption 8) to calculate the upper range of costs.

Table 6.1. Summary of requirements for Designs 1, 2, and 3

	Design 1	Design 2	Design 3
Manufactured Part(s)	SLS part	Top injection molded part Bottom injection molded part	Top SLS part Bottom injection molded part
Additional Component	O-ring	Standard sealant	O-ring
Assembly Steps	1. Slide O-ring on NPE 2. Snap onto spar	1. Ultrasonic weld parts together 2. Apply sealant on NPE 3. Snap onto spar	1. Slide O-ring on NPE 2. Snap parts together 3. Snap onto spar

---

[21] Private Communication with Boeing

6.2 Design Evaluations

6.2.1 Manufacturing Costs

According to the two types of manufacturing methods, SLS and injection molding (IM), cost models, provided by Ruffo et al. (2006a) and Ruffo et al. (2006b) for the former and by Boothroyd et al. (2002) for the latter, will be used to determine overall costs to manufacture the parts. These costs will be either temporal costs or monetary costs. Assuming indirect costs rates, all temporal costs are converted into corresponding monetary costs to fully compare the different designs.

6.2.1.1 SLS Manufacturing Cost

For SLS, the maximum build envelope, V_{bed}, of a ProX SLS 500 machine was assumed (V_{bed} = 15 in. x 13 in. x 18 in.) (3D Systems 2016). From this maximum envelope, a number of parts can be created at once per build, n_p. Given V_{ext}, the bounding box of an individual part (Figure 6.2), $n_p = 9$ is a safe approximation of the number of parts per build for the SLS parts in Designs 1 and 3.
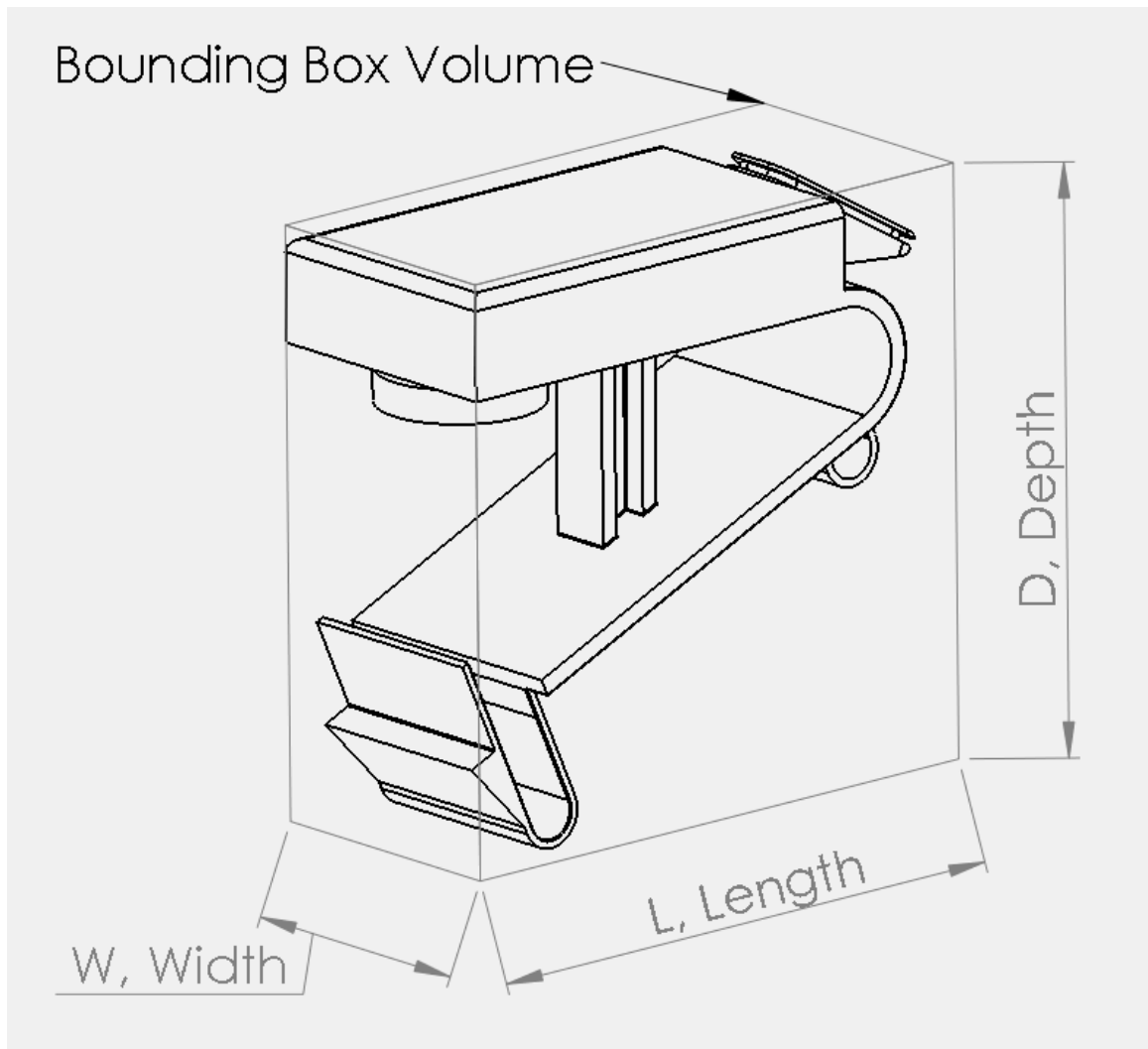
Figure 6.2. Bounding box definition and dimensions

Next, for a given build, Ruffo et al. (2006a) states that the cost of the entire build is the sum of the direct cost of the material and the indirect costs per hour multiplied by the total build time (labeled as process time) (Figure 6.3). However, only the total build time, $(t_{SLS,B})$, will be examined, while material costs will be determined in section 6.2.3.
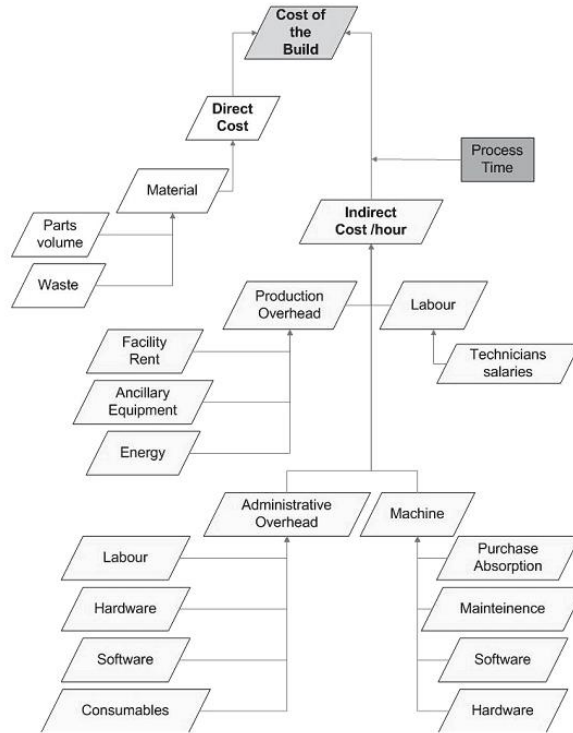
Figure 6.3. SLS cost model (Ruffo et al. 2006a)

Ruffo et al. (2006b) presents an empirical model of total build/cycle time that includes recoating time, scanning time, and pre and post processing time. Recoating time is the time required to add layers of powder; scanning time is the time required to sinter the powder; pre and post processing time is the time required to heat up and cool down the bed before and after the build process, respectively. All three times are summarized in a single expression:

$$t_{SLS,B} = \gamma(0.042 * L^{-0.1809} * L * W) * D + \left(180 - 120 * \frac{V_{ext}}{V_{bed}}\right) * D +$$

$$400 + 3600 \ [s] \tag{6.1}$$

where

$$\gamma = \begin{cases} 0.3422 * Cr^2 + 0.2468 * Cr + 0.45 & if \ Cr < 0.4 \\ 0.417 * e^{0.9283*Cr} & if \ Cr > 0.4 \end{cases} \tag{6.2}$$

and

148

$$Cr = \frac{V_B}{V_{ext}} \qquad\qquad\qquad (6.3)$$

Additionally, V_B is the volume of the individual part, L, W, and D are the respective part dimensions of the bounding box volume (Figure 6.2), and V_{ext} and V_{bed} are as defined above.

Given the model values for the respective SLS parts in Design 1 and Design 3, the time required for one build ($t_{SLS,B}$) and estimated time per part ($t_{SLS,cycle}$) are presented in Table 6.2. $t_{SLS,cycle}$ is an estimated time because, in reality, the SLS machine should create multiple parts during a single run to maximize efficiency; this time is derived for the purposes of comparing with the cycle time of an injection molded part in sections 6.2.1.3 and 6.2.4. Examining the results, the time to create the top part for Design 3 is significantly reduced since the support mount, which is at least twice the height of the actuator, is not created. All values maintain a maximum, overestimation error of 13% (Ruffo et al. 2006b); detailed calculations can be found in Appendix B.

Table 6.2. SLS manufacturing time

	Design 1 (SLS part)	Design 3 (Top SLS part)
$t_{SLS,B}$ (hr/build)	7.542	3.030
$t_{SLS,cycle}$ (hr/part) (with n_p = 9)	0.838	0.337

6.2.1.2 Injection Mold Manufacturing Cost

The first step in estimating the injection molding time is to decide the machine size, which is based on the required clamp force. This force is determined by the projected shot area of the cavities in the mold and the maximum pressure in the mold. The former is obtained from increasing the design's projected part area, A_p (shaded area of Figure 6.4), by the expected runner system percentage increase based on part volume (Table A.2); the latter is obtained from the material supplier (Table 6.3), divided by two

149

due to the pressure loss in the sprue, runner systems, and gates. Both the projected shot area and maximum pressure in the mold are multiplied together to obtain the separating force, which can then determine the required machine size via Table A.3.
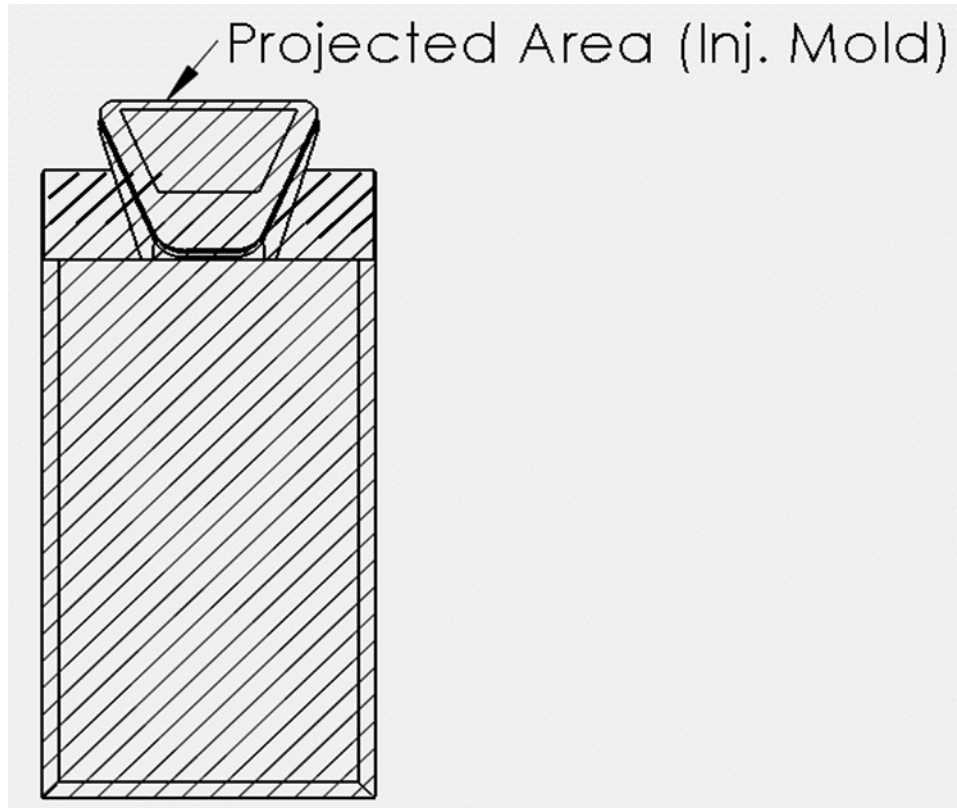
Figure 6.4. Projected part area for Injection Molding

Table 6.3. Process parameters of material

	30% Carbon Fiber reinforced PEKK	Conservative Estimate
Maximum Injection Pressure (psi)	20000	-
Maximum Melt Temperature (F)	720	-
Maximum Mold Temperature (F)	450	-
Ejection Temperature (F)	-	482
Thermal Diffusivity (mm²/s)	-	0.13

Next, the manufacturing cost can be determined from two components: molding

cycle time (a recurring cost) and mold cost (a capital cost). The molding cycle time,

$t_{IM,cycle}$, is the summation of the injection time (i.e., fill time), t_f, cooling time, t_c, and

resetting time, t_r:

$$t_f = \frac{2V_s p_j}{P_j} \ [s] \tag{6.4}$$

where V_s is the required shot size $[m^3]$ that includes the runner system increase from

Table A.2, p_j is the recommended injection pressure $\left[\frac{N}{m^2}\right]$, and P_j is the injection power

$[W]$.

$$t_c = \frac{h_{max}^2}{\pi^2 \alpha_{thermal}} \log_e \frac{4(T_i - T_m)}{\pi(T_x - T_m)} \ [s] \tag{6.5}$$

where h_{max} is the maximum wall thickness $[mm]$, T_x is the recommended polymer

ejection temperature $[°C]$, T_m is the recommended mold temperature $[°C]$, T_i is the

polymer injection temperature $[°C]$, and $\alpha_{thermal}$ is the thermal diffusivity coefficient

$\left[\frac{mm^2}{s}\right]$.

$$t_r = 1 + 1.75 t_d \left[\frac{2D+5}{L_s}\right]^{\frac{1}{2}} \ [s] \tag{6.6}$$

where D is the part depth $[cm]$ as defined in Figure 6.2, and t_d and L_s are the dry cycle

time $[s]$ and maximum clamp stroke $[cm]$, respectively, from the corresponding machine

size (Table A.3). While the injection molded parts are different from the SLS part

depicted in Figure 6.2, the part depth definition is still maintained for that particular

orientation.

Finally, mold cost can be determined from the summation of an initial mold base

cost, C_{base}, and cavity and core manufacturing time, $t_{IM,cc}$. For the mold base cost, the

empirical model is:

$$C_{base} = 1000 + 0.45 A_c h_p^{0.4} \ [USD] \tag{6.7}$$

where A_c is the area of mold base cavity plate [cm], and h_p is the combined thickness of cavity (D from Eq. (6.6)) and core plates in mold base (average of 30 cm total for both plates) [cm]. A_c is determined by imagining the molded part embedded within the mold base plates with an average of 7.5 cm of material as clearance between the cavity and the edges of the cavity plates and additional 7.5 cm plate width or length increase per additional side-pull depending on the orientation of the side-pull.

$t_{IM,cc}$, on the other hand, is composed of multiple factors given as points in Figure 6.6, with the referenced equations:

$$M_e = 2.5 * A_p^{0.5} \ [hr] \tag{6.8}$$

where A_p is the projected part area [cm^2] as defined in Figure 6.4, and M_e is the additional manufacturing hours for the ejector pins/system.

$$M_{po} = 5 + 0.085 * A_p^{1.2} \ [hr] \tag{6.9}$$

where A_p is defined as in Eq. (6.8), and M_{po} is the additional manufacturing hours due to the part size.

$$M_x = 5.83(X_i + X_o)^{1.27} \ [hr] \tag{6.10}$$

where M_x is the additional manufacturing hours due to the geometrical complexity of the part and X_i and X_o are the inner and outer complexity of the part, respectively:

$$X_i = 0.1 * N_{isp} \tag{6.11a}$$

$$X_o = 0.1 * N_{osp} \tag{6.11b}$$

where N_{isp} and N_{osp} are the number of inner and outer surface patches, respectively. These patches can be best described by an example of a "plane conical component with a recessed base" (Boothroyd et al. 2002) similar to a flowerpot. The inner surface is comprised of the following:

1. Main conical surface
2. Flat base

The outer surface is comprised of the following:

1. Main conical surface

2. Flat annular base

3. Cylindrical recess in the base

4. Flat recessed base
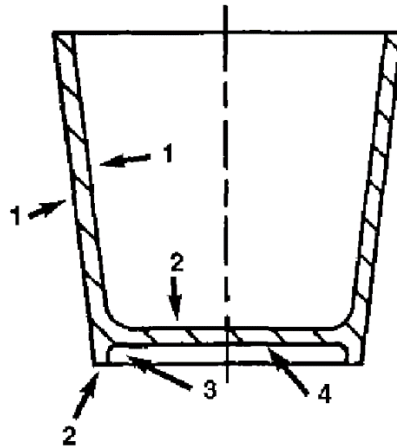
Figure 6.5. Example for N_{isp} and N_{osp} (modified from Boothroyd et al. 2002)

The final factor that affects $t_{IM,cc}$ is M_s:

$$M_s = f_p A_p^{\frac{1}{2}} \quad [hr] \tag{6.12}$$

where f_p is the parting surface factor from Table A.6, A_p is defined as in Eq. (6.8), and M_s is the additional manufacturing hours for a non-flat parting surface.

Regarding some of the factors mentioned in Figure 6.6 for both Designs 2 and 3, two side-pulls were anticipated with the parting surface in the x-y plane (Figure 5.26.b), surface finish appearance was assumed to be "opaque, standard (SPE #3)," and tolerance level was assumed to be "Several approx. ±.05 mm." Remaining assumptions are detailed in Tables B.2-B.5.

153

(i) Projected Area of Part (cm²)

    —Apply Eqs. (6.8) and (6.9), which include points for the size effect on manufacturing cost plus points for an appropriate ejection system,

(ii) Geometric Complexity

    —Identify complexity ratings for inner and outer surfaces from Eq. (6.11a) and Eq. (6.11b).

    —Apply Eq. (6.10) to determine the appropriate point score

(iii) Side-Pulls

    —Identify number of holes or apertures requiring separate side-pulls (side cores) in the molding operation.

    —Allow 65 points for each side-pull.

(iv) Internal Lifters

    —Identify number of internal depressions or undercuts requiring separate internal core lifters.

    —Allow 150 points for each lifter.

(v) Unscrewing Devices

    —Identify number of screw threads that would require an unscrewing device.

    —Allow 250 points for each unscrewing device.

(vi) Surface Finish/Appearance

    —Refer to Table A.4 to identify the appropriate percentage value for the required appearance category.

    —Apply the percentage value to the sum of the points determined for (i) and (ii) to obtain the appropriate point score related to part finish and appearance.

(vii) Tolerance Level

    —Refer to Table A.5 to identify the appropriate percentage value for the required tolerance category.

    —Apply the percentage value to the geometrical complexity points determined for (ii) to obtain the appropriate point score related to part tolerance.

(viii) Texture

    —If portions of the molded part surface require standard texture patterns, such as checkered, leather grain, etc., then add 5% of the point scores from (i) and (ii).

(ix) Parting Plane

    —Determine the category of parting plane from Table A.6 and note the value of the parting plane factor, f_p.

    —Use f_p to obtain the point score from Eq. (6.12).

Figure 6.6. Mold cavity and core point system (modified from Boothroyd et al. 2002)

Given the model values for the respective injection molded parts in Design 2 and Design 3, results are presented in Table 6.4. Detailed calculations can be found in Appendix B.

Table 6.4. Manufacturing costs

	Design 2 (Bottom IM part)	Design 2 (Top IM part)	Design 3 (Bottom IM part)
$t_{IM,cycle}$ (s)	8.01	3.65	6.97
C_{base} (USD)	2514.99	1630.87	2518.50
$t_{IM,cc}$ (hr)	276.48	187.33	255.83

6.2.1.3 Manufacturing Cost Comparison

All manufacturing costs are compiled into a single chart to allow comparison between all three designs (Table 6.5). While capital costs are high for Designs 2 and 3, they eventually become more cost efficient at higher production volumes. To visualize this, indirect cost rates are assumed to covert temporal costs into monetary costs.

Table 6.5. Compiled manufacturing costs

	Cost	Design 1	Design 2	Design 3
Capital Costs	C_{base} (USD)	-	4145.08	2518.50
	$t_{IM,cc}$ (hr)	-	463.81	255.83
Recurring Cost (per part)	Temporal cost (min)	50.28	0.19	20.32

Indirect costs per hour will be assumed to be an average rate of \$18.00 per hour for part manufacturing ($C_{ind,part\ mfg}$) (PayScale 2016) and an average rate of \$44.00 per hour for mold manufacturing ($C_{ind,mold\ mfg}$) (Naitove 2014). The final equation should be, for SLS manufacturing cost, C_{SLS}:

$$C_{SLS} = \frac{t_{SLS,B}}{n_p} C_{ind,part\ mfg} \quad \left[\frac{USD}{part}\right] \tag{6.13}$$

with all values as defined above. Correspondingly, the final equation for injection molded manufacturing costs, C_{IM}, is

$$C_{IM} = \frac{n_{pm}*t_{IM,cycle}*C_{ind,part\ mfg}+C_{base}+t_{IM,cc}*C_{ind,mold\ mfg}}{n_{pm}} \left[\frac{USD}{part}\right] \qquad (6.14)$$

where n_{pm} is the number of parts manufactured, and all other values are as defined above.

Results for these values are displayed in Figure 6.7. Design 1 is the most cost effective when manufacturing <1000 parts per year. However, for larger production volumes, Designs 2 and 3 become more cost effective. Due to the nature of SLS manufacturing, the main benefit is its flexibility in manufacturing different variations of designs, whereas injection molded design costs linearly scale up with the number of different designs required. Thus, as mentioned in section 5.5, Design 3 is able to maintain its cost effectiveness at high production volumes while being flexible enough to manufacture design variations.
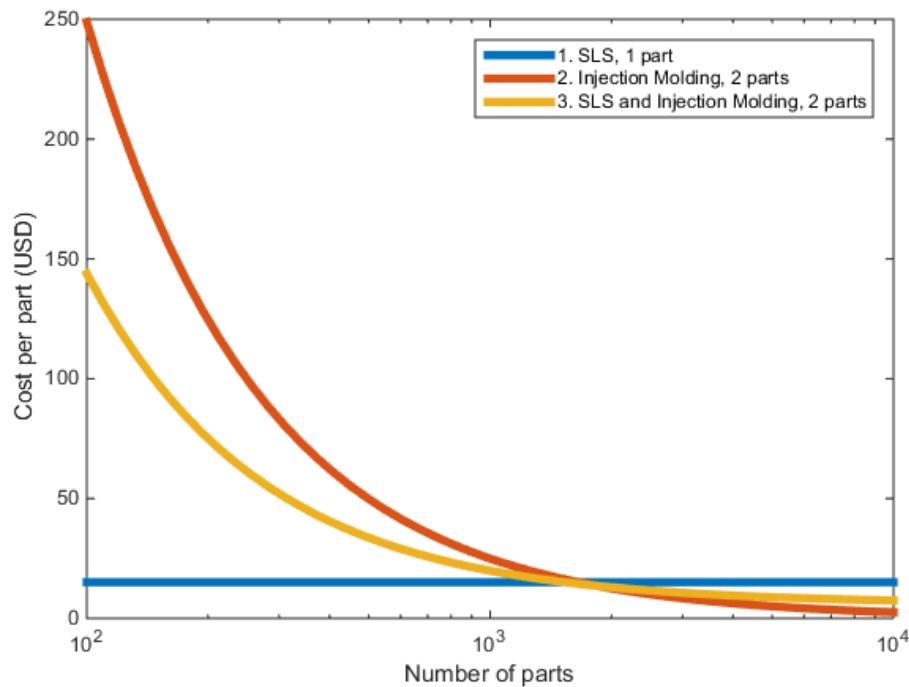
Figure 6.7. Manufacturing Cost Comparison

6.2.2 Assembly Costs

To evaluate the total time to assemble the parts together and onto the spar, the cost model provided by Boothroyd et al. (2002) will be followed. Based on experimental result, a comprehensive model estimates the total assembly time, t_{ma}, taking into account part symmetry, part weight, and part size effects on handling and chamfer design, obstructed access or vision, and holding down effects on insertion.

$$t_{ma} = \sum_1^{n_{pd}}(t_a + n_{items}(t_h + t_i)) \quad [s] \tag{6.14}$$

where n_{pd} is the number of parts and additional components per design in Table 6.1, t_a is the time to aquire a tool (if necessary for a part) $[s]$, n_{items} is the number of items of a particular part, t_h is the average time to handle a part $[s]$ from Table A.7, and t_i is the average time to insert a part $[s]$ from Table A.8. From the total assembly time, assembly time per aircraft is estimated, assuming 64 actuators (Assumption 2), and monetary cost of assembly per aircraft, C_{asm} is calculated (Table 6.6). The cost for C_{asm} is as follows:

$$C_{asm} = t_{ma,64} * C_{ind,asm} \quad \left[\frac{USD}{aircraft}\right] \tag{6.15}$$

where the indirect assembly rate per hour, $C_{ind,asm}$, is assumed to be equivalent to the average indirect part manufacturing rate ($18.00 per hour) and $t_{ma,64}$ is the time to assemble per aircraft. From the results, it is clear that Design 2 has the highest assembly cost, primarily due to an application step of a non-solid sealant, in addition to requiring an ultrasonic weld. Design 3 maintains the second highest assembly cost as a result of assembling two components; Design 1 has the lowest assembly costs because it is manufactured as a single entity.

Table 6.6. Assembly Costs

	Design 1	Design 2	Design 3
Assembly time per BDC (s)	10.94	19.89	14.69
Assembly time per aircraft (min)	11.67	21.22	15.67
Assembly cost per aircraft (USD)	3.50	6.36	4.70

6.2.3 Weight and Material Costs

Density of a material, derived from the specific gravity (Table 6.7), is multiplied with the volume to obtain the weight of a part, accounting for all parts and components in Table 6.1. While the O-ring should be selected by the final designer to ensure it meets all industry requirements and is readily procurable, an ethylene propylene diene monomer (EPDM) O-ring is selected for weight and material cost calculations, since the material has a temperature range of -65°F to 300°F that meets Constraints 4.2.1.6 and 4.2.2.5. The sealant was assumed to have the same weight and monetary cost penalties as the O-ring. From there, material costs for each design are determined through supplier quotes (noted as estimated values in Table 6.7) multiplied by the weights of the respective parts to calculate the total cost of material and additional component. It is important to note that the required shot size, V_s, from Eq. (6.4) is used as the volume for injection molded parts, as it includes the volume of the part and the volume of the runner system.

Table 6.7. Material information

	23% Carbon Fiber reinforced PEKK[22]	30% Carbon Fiber reinforced PEKK[23]	O-ring (The O-ring Store n.d.)
Manufacturing process	SLS	Injection Molding	Purchased
Cost	147.42 (USD/lb)	93.38 (USD/lb)	0.04 (USD/part)
Specific gravity	1.38	1.39	1.17

Assuming the 0.1426 in. wall thickness models (Assumption 8) and 64 actuators/BDCs per aircraft (Assumption 2), corresponding weights and material costs

---

[22] Private Communications with Advanced Laser Materials and Boeing
[23] Private Communication with RTP Company

are listed in Table 6.8. Additionally, in calculating material costs, zero waste was assumed to be produced during manufacturing (i.e., all extra powder is reused during SLS and negligible flash is produced during IM). All three designs weigh the same at about 0.33 lbs per BDC and about 21 lbs per aircraft. Due to the high cost of carbon fiber reinforced PEKK in powder form, the cost is 28% greater for Design 1 than Design 2, whereas Design 3 is only 17% greater than Design 2.

Table 6.8. Weight and Material Costs

	Design 1	Design 2	Design 3
Weight per BDC (lb)	0.33	0.32	0.33
Weight per aircraft (lb)	21.2	20.6	21.2
Material Cost per BDC (USD)	48.84	38.06	44.38
Material Cost per aircraft (USD)	3126.01	2435.87	2840.30

6.2.4 Total cost comparisons

Finally, all capital and recurring costs, including weights, are compiled (Table 6.9). It is evident that Design 1 will be the most economical design in terms of temporal and monetary costs at low production volumes. For higher production volumes, if there is little to no parameter variation (e.g., skin thickness or flap curvature) based on different integration locations, Design 3 will be the best choice. However, if there are a significant number of variations that the design should account for at high production volumes, Design 2 will be the most economical design.

Table 6.9. Compiled costs

	Cost	Design 1	Design 2	Design 3
Capital Costs	C_{base} (USD)	-	4230.86	2518.50
	$t_{IM,cc}$ (hr)	-	469.39	255.83
Recurring Costs (per part)	Manufacturing and assembly time (min)	50.46	0.53	20.56
	Material Cost (USD)	48.84	38.06	44.38
	Weight (lb)	0.33	0.32	0.33

Again, to better visualize this comparison, temporal costs are converted to monetary costs assuming $44.00 per hour average mold manufacturing rates (Naitove 2014) and $18.00 per hour average part manufacturing and assembly rates (PayScale 2016). From Figure 6.8, it is evident that high production is > 1000 parts, where Designs 2 and 3 become more economical than Design 1. Design 1 manufacturing, assembly, and material cost at is about $64 per part for all production volumes, whereas the cost for Design 3 can reach down to about $41 per part. With the 64 actuators per aircraft assumption (Assumption 2), cost per aircraft at all production volumes for Design 1 is about $4090, whereas, at high production volumes for Design 3, the cost per aircraft is about $2600. Design 2 maintains a cost of about $52 per part, which translates to about $3320 per aircraft.
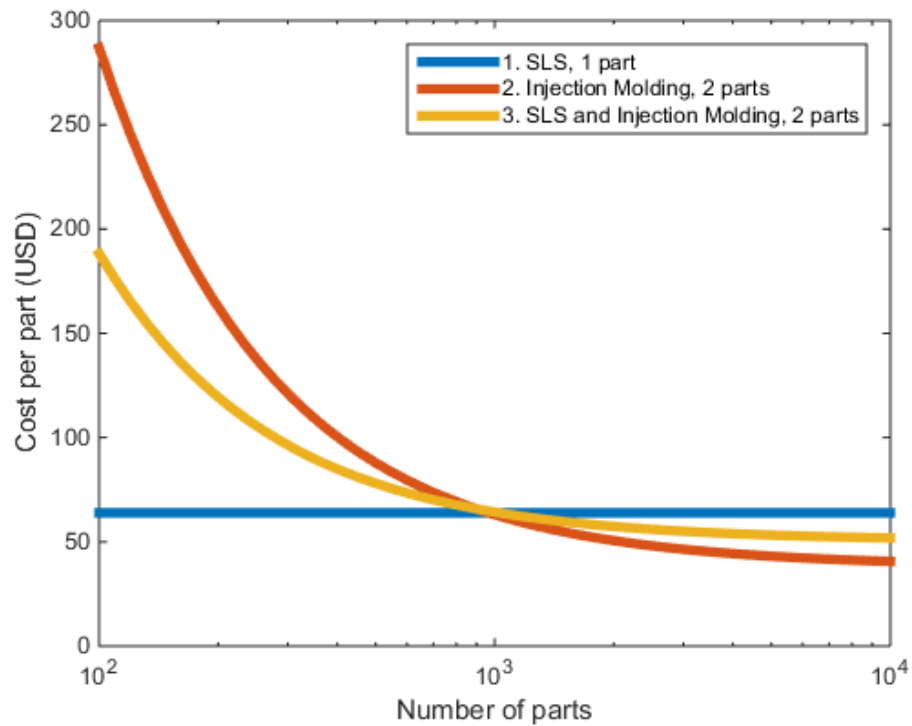
Figure 6.8. Manufacturing, assembly, and material costs

6.2.5 Actuator Modification

In the case of a different internal actuator design, the procedures discussed in section 1 can be applied to the new actuator. With each actuator, the optimized wall thickness may be different; hence, the procedures for creating the NPE and SM are based off of the actuator design.

Of course, utilizing a different actuator design will alter the manufacturing, material, and weight costs; assembly costs are not dependent on the specific actuator design. Costs were calculated in Microsoft Excel 2013 using appropriate equations referenced in section 6.2. Regarding manufacturing costs, altering the design of the actuator will affect the part depth (D) (Eq. 6.1, Eq. 6.6, Figure 6.2, and Tables B.1 and B.2), part width (W) (Eq. 6.1, Figure 6.2, and Tables B.1 and B.4), part (L) (Eq. 6.1, Figure 6.2, and Tables B.1 and B.4), projected part area for injection molding (A_p)

(Figure 6.4 and Table B.2), bounding box volume (V_{ext}) (Eq. 6.3, Figure 6.2, and Table B.1), object volume (V_B) (Tables B.1 and B.2), maximum wall thickness (h_{max}) (Eq. 6.5 and Table B.3), and number of inner and outer surface patches (N_{isp} and N_{osp}) (Eq. 6.11a, Eq. 6.11b, and Table B.5) depending on if the design changes are internal, external, or both. All altered dimensional inputs are highlighted in their respective tables in Appendix B. The variable value adjustments will automatically propagate through the remaining Excel equations, such as how a different A_p will affect the area of mold base cavity plate (A_c) (Eq. 6.7) or how a different D will affect the thickness (h_p) in Eq. 6.7, to result in the final costs specific to the actuator. Material and weight costs can be calculated according to the volume of the new design as discussed in section 6.2.3.

6.3 Chapter Summary

All manufacturing and assembly procedures are described, first, at the macro-scale for integrating the BDC into the flap structure summarized in Figure 6.1 and, second, at the micro-scale for the three different designs of the BDC summarized in Table 6.1. Furthermore, temporal, monetary, and weight costs are evaluated from an analysis of the manufacturing and assembly process and materials utilized of the three different designs. All three designs weigh about the same at 0.33 lbs, which corresponds to about 21 lbs per aircraft, given 64 actuators per aircraft (Meyer et al. 2014). At low production volumes (<1000 parts), Design 1 is the most economical option, at about $64 per part and $4090 per aircraft. At high production volumes (>1000 parts), Design 3 demonstrates the least cost, at about $41 per part and $2600 per aircraft. However, if multiple variations were required due to different integration location parameters (e.g., skin thickness or bullnose curvature), Design 2 would be the most economical design at high production volumes due to its flexibility in adjusting to the different parameters, at

roughly $52 per part and $3320 per aircraft. In the case an alternate actuator design is used, corresponding changes are discussed in section 6.2.5. In the following chapter, concluding remarks will be made for this entire work.

CHAPTER 7

CONCLUSIONS

Full integration of an unsteady active flow control system in the leading edge slat and trailing edge flap, could potentially lead to reductions of up to 2.6% in part count, 3.3% in empty weight, and 1.3% in recurring manufacturing cost of the respective totals of a Boeing 737-700 (McLean et al. 1999). To put this into perspective, the simplification of the flap could result in a drag reduction of up to 3.2%, while, given a $30 M aircraft, savings in recurring manufacturing costs would be about $400 K (McLean et al. 1999). However, these benefits do not account for the penalties associated with the integrated, unsteady active flow control system. While much research has been conducted with regards to the feasibility and aerodynamic benefits of integration, little work has been conducted with regards to the manufacturability and cost of integration. This issue is addressed on two fronts in the form of a primary and a secondary objective.

The primary objective was to design a comprehensive solution to integrating a feedback-free fluidic oscillator into the nonstructural, leading edge of a trailing edge flap structure on a civil transport aircraft. The secondary objective, was to determine what effect(s) different manufacturing techniques would have on the oscillation of the jet flow from the fluidic oscillator. Logically, solving the secondary objective ought to precede solving the primary objective in order to aid the manufacturing method selection for the integration solution in the primary objective. With the results from the secondary objection, a more successful integration solution for the primary objective can be attained.

Following research into the field of fluidic device manufacturing, fused deposition molding (FDM) and selective laser sintering (SLS) were manufacturing methods discovered to not appear in literature regarding fluidic device manufacturing.

Thus, these two methods were selected, in addition to machining and sterolithography (SLA) (fluidic oscillator research standards) and injection molding (fluidic device industry standard) as methods of producing fluidic oscillators to test. FDM and SLS are methods of particular importance due to their ability in creating a thermoplastic fluidic device in one part, as opposed to two parts that then require encapsulation of the two parts.

Each selected method was used to create at least one insert to test in a reusable test module; due to a machining error, three nominal designs were created and tested: one of desired nominal dimensions (Design 2) and two that decreased or increased the nozzle wall thickness (Design 1 and Design 3, respectively). Pressure, oscillation frequency, and the velocity profile were measured characteristics, via an in-line pressure gauge for the first and hot-wire anemometry for the latter two, of the performance of the air flow. Pressure was measured ~100 mm upstream of the air inlet and oscillation frequency was measured at a fixed streamwise (x-axis) location of x = 3 mm at a spanwise (z-axis) location chosen for maximum oscillation, while volumetric flow rate (Q) was controlled in 50 L/min increments from Q = 0 L/min to 300 L/min for both pressure and frequency measurements. For the velocity profile measurements, flow rate and streamwise and spanwise measurement locations were controlled at Q = 50, 150, and 300 L/min, x = 3, 8, 15, and 25 mm, and z in increments of 0.635 mm for a total range of Δz = 50 mm. To characterize the manufacturing methods, surface roughness (R_a) and geometric dimensions (including the aspect ratio, AR) and tolerances were taken for each insert.

The surface roughness, manufactured tolerance (maximum dimensional difference from corresponding nominal dimension), and AR are then compared against the symmetry of the velocity profiles, determined through the jet sweep half-angle difference ($\theta_{jet\ difference}$) and normalized peak difference; the lower the latter two values are, the more symmetric the velocity profiles are. Very little to no correlation is determined from the comparisons of manufactured characteristics to oscillator performance. However,

results indicated that all inserts, including the FDM and SLS inserts, of Design 2 produced desired oscillation characteristics at Q = 150 L/min with desirable oscillation frequencies[24]. These oscillation characteristics manifested in the form of two velocity peaks in the velocity profile, demonstrating sweeping of the jet of air similar to results gained by researchers at Georgia Tech[25] and thus validating the manufactured characteristics of SLS and FDM inserts.

Examining the velocity profile data from inserts of Designs 1 and 3 at Q = 150 L/min the nozzle wall thickness was determined to potentially have an upper and lower limit in ensuring jet oscillation with two velocity peaks. Comparing the velocity profile data of all inserts at Q = 50 L/min and 300 L/min, flow rate may also have upper and lower limits in producing jet oscillation with two velocity peaks.

Next, the primary objective was examined by utilizing axiomatic design (AD) and design for manufacturing and assembly (DFMA) methodologies to design a robust integration solution. From AD, three parts were determined to be necessary for the integration solution: the actuator, a nozzle profile extension (NPE), and a support mount (SM). Additional functional requirements (FRs) of each part and associated design parameters (DPs) are listed in Table 4.3; after examination of all relationships, the independence axiom was determined to have been met. Additionally, from the experimental results comparing manufacturing methods of fluidic oscillators, SLS and injection molding were selected as desired manufacturing processes able to produce cost efficient fluidic oscillators with more desirable flow characteristics, assuming a thermoplastic material constraint.

---

[24] Private Communication with Dr. Michael DeSalvo of Georgia Tech's FMRL
[25] Private Communication with Dr. Bojan Vukasinovic of Georgia Tech's FMRL

Regarding the actuator part, the internal width and height were constrained before adding a circular air-duct connection feature on the bottom actuator face, which constrained the internal length, to allow for unobstructed access to the air supply. Next, after running finite element analysis (FEA) simulations, a wall thickness range of 1/16 – 0.1426 in. was deemed sufficient. In the case of partial nozzle blockage, pressurized or heated air (McLean et al. 1999) should clear the opening. In the case of complete nozzle blockage, a leak-before-break criterion was met, assuming a 0.1426 in. wall thickness and PEEK material.

A recessed (DeSalvo et al. 2011) NPE design was selected such that a straight cut could be created in the bullnose skin while minimizing the distance the jet of air travels from the nozzle orifice to freestream. Additionally, the NPE was integrated into the actuator to reduce part count, allowing the actuator as opposed to the bullnose skin to support the NPE. This simple design should allow for the bullnose skin to slide on and off the NPE without any permanent attachment method. A trapezoid hole shape was selected to minimize the composite material removed, although an oval hole shape could reduce maximum stresses and strains by 54% while spreading out stresses over a larger area with 101% more composite material removed, determined through FEA simulations. Other factors that affect hole size, including bullnose skin/actuator wall thickness, thermal expansion and contraction, and fiber sealing, were discussed. Finally, the sealant system options were reduced to either an O-ring or a standard sealant, depending on the typical sealant method used on aerospace structures.

The final SM part was integrated into the actuator to reduce part count and located closer to the top of the front spar to minimize space and material utilized. To maintain an injection moldable design and to maintain the 30 degree angle with respect to the airfoil tangent, an angle bracket was selected as the basis of the SM design; to efficiently transmit expected loads to the spar and to also maintain an injection moldable design, an I-beam was selected as a support beam directly below the actuator's center of mass.

For attachment of the SM to the spar, snap-fits were selected to reduce part count. Specifically, a cantilever hook snap-fit was selected to allow assembly and disassembly from one side of the composite spar. Furthermore, a U-shaped snap-fit design permits the strains experienced to remain under low allowable limits while maintaining higher separation forces than simple cantilever beams. Trade-offs between a slot hole shape and a circular hole shape were discussed.

A top and bottom snap-fit was designed for minimal number of composite holes (2) in the spar, constraining the rectangular back plate SM shape, and so that the tooling for the bullnose skin hole could be used for each of the spar holes as well. Finally, the snap-fits were designed to be located far apart to reduce stress concentration interactions and designed with different beam widths to easily orient the entire device for manual assembly, with reasonable mating force (14.8 lb) and seperation forces (10 lb for bottom snap-fit and 6.8 lb for top snap-fit). FEA simulations applying expected loading conditions on the entire structure validated the proposed snap-fit design as the fastener for the SM, as well as validated the BDC as the amalgamation of the actuator, NPE, and SM.

Three designs were created from the BDC, to be manufactured via SLS (Design 1), injection molding (Design 2), and both SLS and injection molding (Design 3). Next, the macro-scale level of required manufacturing and assembly procedures were explained, along with the micro-scale level of procedures for manufacturing and assembling the three BDC designs. Finally, estimates of the manufacturing, assembly, material, and weight costs were conducted of the three BDC designs. All three designs weigh about the same at 0.33 lbs, which corresponds to about 21 lbs per aircraft, given 64 actuators per aircraft (Meyer et al. 2014). At low production volumes (<1000 parts), Design 1 is the most economical option, at about $64 per part and $4090 per aircraft. At high production volumes (>1000 parts), Design 3 demonstrates the least cost, at about $41 per part and $2600 per aircraft. However, if multiple variations were required due to

different integration location parameters (e.g., skin thickness or bullnose curvature),

Design 2 would be the most economical design at high production volumes due to its

flexibility in adjusting to the different parameters, at roughly $52 per part and $3320 per

aircraft.

In conclusion, the performance of fluidic oscillators manufactured with different

methods, including FDM and SLS, were compared against manufactured characteristics

to demonstrate slight correlations. Furthermore, all manufacturing methods produced

desired oscillation frequencies with two velocity peaks, given a nominal dimensions and

$Q = 150$ L/min, demonstrating that characteristics resulting from different manufacturing

methods do not significantly, negatively affect air flow oscillation. Changing the nozzle

wall thickness or flow rate can result in undesired oscillation with one velocity peak. A

full scale, best design concept for the integration solution is proposed after checking

against design specifications, utilizing experimental results, applying rigorous design

methodologies, and simulating expected loading conditions. Moreover, cost analyses of

manufacturing, assembly, material, and weight costs per part and per aircraft, are

conducted for three BDC designs to estimate the total costs of the integration solution.

Therefore, the research conducted in this thesis provides a basis for the design of

manufacturing and assembly techniques to integrate active flow control technology into

civil transport aircraft.

7.1 Future Recommendations

Regarding the fluidic oscillator experiments, due to a small sample size of tested

inserts, further experimentation of nominally different designs should be conducted to

examine the effect various dimensions and characteristics have on performance. Thus,

acceptable surface finished, critical dimensions, and tolerance levels for those critical

dimensions can be more accurately determined, which can aid in the selection of fluidic

oscillator manufacturing method. Additionally, the amount of and importance of velocity

peak symmetry should be examined to properly quantify air flow performance. Finally, to eliminate the noted gasket issue, a different test module ought to be used for future experimentation.

For the BDC, decisions including the bullnose skin hole shape and sealant system remain to be finalized according to customer requirements. Moreover, the air-duct connection location and the snap-fit design should be reexamined to ensure proper air supply and composite spar constraints, respectively, are met. Further design changes ought to be implemented based on the manufacturing methods, summarized in Figures 5.27, 5.28, and 5.30. Finally, at the macro-scale, cutting and/or composite build-up operations ought to be examined that can properly create the necessary holes in the bullnose and spar. From these design changes, a full-scale model can be rapid prototyped for integration into a flap structure to fully examine the effect of environmental and loading conditions, in addition to air flow characteristics over the integrated area.

APPENDIX A

REFERENCED TABLES

This appendix provides the referenced tables and charts from other sources that aide in material selection and evaluating injection molding manufacturing and assembly costs.

Table A.1. Overview of bonding methods for thermoplastic microfluidic devices (Tsao and DeVoe 2009)

Bonding method	Bonding strength	Bonding quality	Process complexity	Bonding time	Cost[a]	Advantage	Limitation	Suitable material
Adhesive printing bonding	High	Fair	Medium–high	Short–medium	Low–medium	Low temperature, high bond strength, low channel clogging, controllable adhesive thickness	Scarification channel (contact printing) or printing mask (screen printing) required	PMMA, COC
Adhesive interstitial bonding	High	Fair	Low	Short	Low	Simple, fast, low temperature, high bond strength, low channel clogging, low cost	Adhesive loading reservoirs or flush adhesive out of channel needed	PMMA
PDMS-interface bonding	Medium	Low	Medium	Long	Medium	Low temperature, compatible with PDMS microfluidics	PDMS layer may squeeze into channel	PMMA
Lamination film bonding	Medium	Fair	Low	Short	Low	Simple, fast, low cost, low temperature, no adhesive clogging	Lamination film may embedded inside channel	PMMA, PC, PS, PET
Thermal fusion bonding	Medium	Fair	Low	Long	Low–medium	Simple, homogeneous channel, compatible with various material	Channel deformation from un-optimized process condition	PMMA, PC, PS, nylon, COC, PSU
Solvent bonding	High	Fair	Low	Low	Low	Simple, fast, low temperature, high bond strength, low cost	Soften polymer surface may collapse channel from un-optimized process	PMMA, PC, COC
Solvent bonding with sacrificial material	High	Good	High	Medium	Low	High bond strength, low cost, low channel collapse and clogging	Sacrificial material need applied into channel before bonding and removed after bonding	PMMA
Localized welding	Medium	Fair	Medium–high	Medium	Medium	Low temperature, localized bonding	Energy director (ultrasonic welding) or metal layer (microwave welding) are required	PMMA, PEEK
Surface treatment bonding	Medium–High	Good	Medium	Medium	Medium–high	Low temperature bonding, low channel deformation	Surface chemistry changed after treatment	PMMA, PC, COC PS, PET

Table A.2. Runner volumes and respective runner system increase (Boothroyd et al. 2002)

Part volume (cm³)	Shot size (cm³)	Runner %
16	22	37
32	41	28
64	76	19
128	146	14
256	282	10
512	548	7
1024	1075	5

Table A.3. Machine sizes of different clamp forces (Boothroyd et al. 2002)

Clamping force (kN)	Shot size (cc)	Operating cost ($/h)	Dry cycle times (s)	Maximum clamp stroke (cm)	Driving power (kW)
300	34	28	1.7	20	5.5
500	85	30	1.9	23	7.5
800	201	33	3.3	32	18.5
1100	286	36	3.9	37	22.0
1600	286	41	3.6	42	22.0
5000	2290	74	6.1	70	63.0
8500	3636	108	8.6	85	90.0

Table A.4. Percentage increases for appearance (Boothroyd et al. 2002)

Appearance	Percentage increase
Not critical	10
Opaque, standard (SPE #3)	15
Transparent, standard internal flaws or waviness permissible	20
Opaque, high gloss	25
Transparent, high quality	30
Transparent, optical quality	40

Table A.5. Percentage increases for tolerance (Boothroyd et al. 2002)

Tolerance level	Description of tolerances	Percentage increase
0	All greater than ±0.5 mm	0
1	Most approx. ±0.35 mm	2
2	Several approx. ±0.25 mm	5
3	Most approx. ±0.25 mm	10
4	Several approx. ±0.05 mm	20
5	Most approx. ±0.05 mm	30

Table A.6. Parting surface classification (Boothroyd et al. 2002)

Parting surface type	Factor (f_p)
Flat parting plane	0
Canted parting surface or one containing a single step	1.25
Two to four simple steps or a simple curved surface	2
Greater than four simple steps	2.5
Complex curved surface	3
Complex curved surface with steps	4

Table A.7. Handling time tables (Boothroyd et al. 2002)

a) for parts that can be grasped and manipulated with one hand without the aid of grasping tools

sym (deg) = (alpha+ beta)		no handling difficulties			part nests or tangles		
		thickness > 2mm		< 2mm	thickness > 2mm		< 2mm
		size > 15mm	6mm < size < 15mm	size > 6mm	size > 15mm	6mm < size < 15mm	size > 6mm
		0	1	2	3	4	5
sym < 360	0	1.13	1.43	1.69	1.84	2.17	2.45
360 <= sym < 540	1	1.5	1.8	2.06	2.25	2.57	3.0
540 <= sym < 720	2	1.8	2.1	2.36	2.57	2.9	3.18
sym = 720	3	1.95	2.25	2.51	2.73	3.06	3.34

b) for parts that can be lifted with one hand but require two hands because they severely nest or tangle, are flexible or require forming etc.

		alpha <= 180		alpha = 360
		size > 15mm	6mm < size <15mm	size > 6mm
		0	1	2
	4	4.1	4.5	5.6

c) definition of Alpha and Beta

α	0	180	180	90	360	360
β	0	0	90	180	0	360

174

Table A.8. Insertion time tables (Boothroyd et al. 2002)

a) part inserted but not secured immediately or secured by snap fit

		secured by separate operation or part				secured on insertion by snap fit	
		no holding down required		holding down required			
		easy to align	not easy to align	easy to align	not easy to align	easy to align	not easy to align
		0	1	2	3	4	5
no access or vision difficulties	0	1.5	3.0	2.6	5.2	1.8	3.3
obstructed access or restricted vision	1	3.7	5.2	4.8	7.4	4.0	5.5
obstructed access and restricted vision	2	5.9	7.4	7.0	9.6	7.7	7.7

b) part inserted and secured immediately by screw fastening with power tool
(times are for 5 revs or less and do not include a tool acquisition time of 2.9s)

		easy to align	not easy to align
		0	1
no access or vision difficulties	3	3.6	5.3
restricted vision only	4	6.3	8.0
obstructed access only	5	9.0	10.7

c) all parts inserted

	screw tighten with power tool	manipulation, reorientation or adjustment	addition of non solids
	0	1	2
6	5.2	4.5	7

APPENDIX B

MANUFACTURING AND ASSEMBLY COST EVALUATIONS

This appendix provides the detailed cost evaluations of the three BDC designs.

Table B.1. SLS procedure and material costs

Assumptions		Design 1: Thick SLS	Design 3: Thick SLS
Assume Oring		One part	Top part
100% unused powder can be reused			
Build Envelope of 13"x15"x18" can comfortably fit 9 parts	Number of parts/build	9	9
	V_bed, Bounding Box (in^3)	3510	3510
Figure 6.2	D, Part Depth (in)	4.243	1.13945
	D, Part Depth (mm)	107.7722	28.94203
Figure 6.2	W, Part Width (in)	2.08	2.08
	W, Part Width (mm)	52.832	52.832
Figure 6.2	L, Part Length (in)	4.58	4.58
	L, Part Length (mm)	116.332	116.332
Bounding box area	(A = L*W), Projected Area (in^2)	9.5264	9.5264
Bounding box area	(A = L*W), Projected Area (mm^2)	6146.052224	6146.052224
	V_ext, Bounding Box Volume/build (in^3)	363.7846368	97.69370832
Figure 6.2	V_B, Total Object Volume/part (in^3)	6.64576	3.57645
	V_B, Total Object Volume/build (in^3)	59.81184	32.18805
Eq. (6.3)	(Cr = V_B/V_ext), Compact Ratio	0.164415519	0.329479253
Eq. (6.2)	g if Cr>.4	0.485759259	0.566196852
Eq. (6.2)	g if Cr<.4	0.499828259	0.56846354
	(t_xy_box = .042*L^-.1809*A)*D), Scan Time for Bounding Box (s)	11767.04192	3160.017892
	(t_xy = g*t_xy_box), Scan Time (s)	5715.949559	1796.354959
	(P_ext = V_ext/V_bed), External Packing Ratio	0.103642347	0.027832965
	(t_z = (180-120*Pr_ext)*z+400), Recoating Time (s)	18458.62435	5512.900298
Typical Value 60 min	(t_HC), Heat up and Cool down time (min)	60	60
Eq. (6.1)	(t = t_xy+t_z+t_HC), Total Time (min)	462.9095652	181.820921
Indirect Assembly costs $18 /h	Average Manufacturing Technician Wage (USD/h)	18	18
	Wage * Time	138.8728696	54.54627629
	Time (hr)	7.71515942	3.030348683
		15.43031884	6.060697365
PEKK, 23% Carbon Fiber SLS	Material Cost (USD/lb)	147.4176956	147.4176956
	Total Mass/Part (lb)	0.33133	0.17831
	Material Cost/Build (USD/build)	439.5951456	236.5744437
	Material cost/part	48.84390507	26.2860493
Eq. (6.13)	(C_SLS = V_pi/V_b*(Wage*Total Time+Material Cost/Build)), Cost/part (USD/part)	64.27422391	32.34674666

Table B.2. Injection molding procedure and material costs

Assumptions		Design 2: Thick Injection Molded		Design 3: Thick Inj. Mold
Assume Standard Sealant		Bottom Part	Top Part	Bottom Support
Figure 6.4	Total Projected Area (in^2)	9.0048	6.693472	9.5264
	Total Projected Shot Area (in^2)	10.715712	9.17005664	12.193792
Figure 6.2	D, Part Depth (in)	4.243	0.143	3.714866
	D, Part Depth (cm)	10.77722	0.36322	9.43575964
	Machine Selection			
	Material Cost (USD/Part)	30.63405125	7.426471454	18.09366275
	V_B, Total Object Volume (in^3)	5.48976	1.156	3.01448
	V_B, Total Object Volume (cc)	89.9612461	18.9434876	49.39858521
Table A.2	Runner %	1.19	1.37	1.28
	Required Shot Size (in^3)	6.5328144	1.58372	3.8585344
PEKK, 30% Carbon Fiber, Inj. Mold	Density (lb/in^3)	0.05021694	0.05021694	0.05021694
PEKK, 30% Carbon Fiber, Inj. Mold	Material (USD/lb)	93.38	93.38	93.38
PEKK, 30% Carbon Fiber, Inj. Mold	Maximum Injection Pressure (psi)	20000	20000	20000
PEKK, 30% Carbon Fiber, Inj. Mold	Maximum Injection Pressure (MPa)	138	138	138
	Maximum Separating Force (lb)	214314.24	183401.1328	243875.84
	Maximum Separating Force (N)	476658.4443	407904.2935	542406.6945
Table A.3	Appropriate Machine based on Max Separating Force (N)	800 kN machine	500 kN machine	800 kN machine
Table A.3	Max Machine Shot Size (cc)	201	85	201
Table A.3	Operating Cost (USD/h)	33	30	33
Table A.3	Dry Cycle Times (s)	3.3	1.9	3.3
Table A.3	Maximum clamp stroke (cm)	32	23	32
Table A.3	Driving power (kW)	18.5	7.5	18.5
	Check Shot size is within Max Shot Size	Yes	Yes	Yes
	Check Depth is within 1/2 Max Clamp Stroke	Yes	Yes	Yes

Table B.3. Injection molding procedure and material costs (cont.)

Assumptions		Design 2: Thick Injection Molded		Design 3: Thick Inj. Mold	
Assume Standard Sealant		Bottom Part	Top Part	Bottom Support	
	Molding Cycle Cost/Part (USD/Part)	0.040042113	0.018258939	0.034844302	
	Molding Cycle Time (s)	8.008422551	3.651787838	6.968860347	
	Required Shot Size (in^3)	6.5328144	1.58372	3.8585344	
	V_s, Required Shot Size (m^3)	0.000107054	2.59526E-05	6.32302E-05	
	P_j, Injection Power (W)	18500	7500	18500	
	p_j, Maximum Injection Pressure (Pa)	138000000	138000000	138000000	
Eq. (6.4)	($t_f = 2*V*p/P$), Injection Time/ Fill time (s)	1.597128198	0.955054871	0.943326064	
	h_{max}, Max Wall Thickness	0.286	0.143	0.143	
Assumed 250 deg C	T_x, Recommended Part Ejection Temperature (deg C)	250	250	250	
PEKK, 30% Carbon Fiber, Inj. Mold	T_m, Recommended mold Temperature (deg C)	232	232	232	
PEKK, 30% Carbon Fiber, Inj. Mold	T_i, Polymer injection temperature (deg C)	382	382	382	
Polycarbonate, 30% glass (Boothroyd et al. 2002)	alpha, Thermal Diffusivity Coefficient (mm^2/s)	0.13	0.13	0.13	
Eq. 6.5	($t_c = h^2/pi^2/a*log_e(4*(T_i-T_m)/pi/(T_x-T_m))$), Cooling Time (s)	0.150569681	0.03764242	0.03764242	
	t_d, Dry Cycle Time (s)	3.3	1.9	3.3	
	D, Part Depth (cm)	10.77722	0.36322	9.43575964	
	L_s, Maximum Clamp Stroke (cm)	32	23	32	
Eq. (6.6)	($t_r = 1+1.75*t_d*[(2*D+5)/L_s]^.5$), Mold Reset Time (s)	6.260724672	2.659090547	5.987891863	
Assumed $18/hour	Average Manufacturing Indirect costs per hour (USD/h)	18	18	18	

Table B.4. Injection molding procedure and material costs (cont.)

Assumptions		Design 2: Thick Injection Molded				Design 3: Thick Inj. Mold	
Assume Standard Sealant		Bottom Part		Top Part		Bottom Support	
Part of Eq. (6.14)	**Mold Cost (USD)**	14679.47642		9873.220322		13775.23104	
	Mold Base Cost (USD)	2514.208055		1630.867819		2518.497805	
	L, Part Length (cm)	10.99624615		8.173759077		11.6332	
	W, Part Width (cm)	5.2832		5.2832		5.2832	
	Clearance (cm)	7.5		7.5		7.5	
Assume 1 cavity	A_c, Area of Mold Base Cavity Plate (cm^2)	917.2307523	Assume 2 sidepulls either side	470.0379901	Assume 0 sidepulls	939.7045222	Assume 2 sidepulls either side
	h_p = D+2*Clearance, Combined thickness of cavity and core plates in model base (cm)	25.77722		15.36322		24.43575964	
Eq. (6.7)	(C_base = 1000+.45*A_c*h_p^.4), Mold Base Cost (USD)	2514.208055		1630.867819		2518.497805	

Table B.5. Injection molding procedure and material costs (cont.)

Assumptions		Design 2: Thick Injection Molded				Design 3: Thick Inj. Mold	
Assume Standard Sealant		Bottom Part		Top Part		Bottom Support	
Part of Eq. (6.14)	**Cavity and Core Manufacturing Cost (USD)**	12165.26836		8242.352503		11256.73324	
	Cavity and Core Manufacturing Time (h)	276.4833718		187.3261933		255.8348463	
	A_p, Project Part Area (cm^2)	58.09536768		43.18360396		61.46052224	
	(N_e = A_p^.5), Required Ejector Pins	7.622031729		6.571423282		7.839676157	
Eq. (6.8)	(M_e = 2.5*A_p^.5), Manufacturing Time for Ejection Part (h)	19.05507932		16.42855821		19.59919039	
Excluding ultrasonic welding features, Figure 6.5	N_isp, Number of Inner Surface Patches	40		0		31	
Figure 6.5	N_osp, Number of Outer Surface Patches	25		11		17	
Eq. (6.11a)	(X_i = .1*N_isp), Inner Complexity of Part	4		0		3.1	
Eq. (6.11b)	(X_o = .1*N_osp), Outer Complexity of Part	2.5		1.1		1.7	
Eq. (6.10)	(M_x = 5.83*(X_i+X_o)^1.27), Manufacturing Time for Mold based on geometrical complexity (h)	62.8157454		6.580172289		42.74102433	
Eq. (6.9)	(M_po = 5+.085*A_p^1.2), Manufacturing Time for Mold based on part size (h)	16.12727269		12.79473916		16.90513765	
	Side Pulls	2		2		2	
	(T_SP = 65*SP) Cost of Side Pulls (h)	130		130		130	
Table A.4; Opaque, standard (APE #3)	Appearance Percentage Increase	0.15		0.15		0.15	
	Manufacturing Time for Mold based on Appearance (h)	12.28062371		3.451309574		9.351032208	
Table A.5; Level 4 (Several approx. +/- .002")	Tolerance Level Percentage Increase	0.3		0.3		0.3	
	Manufacturing Time for Mold based on Tolerance (h)	5.716523797		4.928567462		5.879757117	
Table A.6	f_p, Parting Plane Factor	4	Complex curved surface with steps	2	2 to 4 simple steps or a simple curved surface	4	Complex curved surface with steps
Eq. (6.12)	(M_s = f_p*A_p^.5), Additional mold manufacturing hours for nonflat parting surface (h)	30.48812692		13.14284656		31.35870463	
Assumed $40 per hour (Boothroyd et al. 2002)	Average Indirect Rate for Mold Manufacturing (USD/h)	44		44		44	

Table B.6. Assembly costs

	Design 1		Design 2			Design 3		
Number of parts	2 parts		3 parts			3 parts		
	Actuator	Oring	Actuator Top	Actuator Bottom	Sealant	Actuator	Support Mount	Oring
Number of Items (RP)	1	1	1	1	1	1	1	1
Tool Acquire Time (TA)		2.9			2.9			2.9
Handling code	30	2	30	30	2	30	30	2
Handling time (TH)	1.95	1.69	1.95	1.95	1.69	1.95	1.95	1.69
Insertion code	4	2	2	4	62	4	4	2
Insertion time (TI)	1.8	2.6	2.6	1.8	7	1.8	1.8	2.6
Total Time (TA+RP*(TH+TI)	3.75	7.19	4.55	3.75	11.59	3.75	3.75	7.19
Total Time per actuator	10.94		19.89			14.69		
Total Time per aircraft (s) (64)	700.16	11.6693333	1272.96	21.216		940.16	15.66933333	
Average Assembly rate (USD/hr)	18		18			18		
Cost per aircraft (USD)	3.5008		6.3648			4.7008		
Cost per part (USD)	0.0547		0.09945			0.07345		

APPENDIX C

CONSTRAINTS AND ASSUMPTIONS

This appendix provides constraints and assumptions referred to throughout this work.

Table C.1. Constraints

4.2.1.1.	Bullnose is ~0.12 in. thick fiberglass composite and does not provide structural support[26].
4.2.1.2.	Front, carbon fiber composite spar location is ~5-6% chord and provides structural support[26].
4.2.1.3.	Front spar shall support the AFC device[26].
4.2.1.4.	Front spar has access holes with which to pass items/objects through[26].
4.2.1.5.	The wing tip can experience anywhere from -1 to 9 g's[26].
4.2.1.6.	Inboard ailerons withstand temperatures from -65 °F to 180°F (Mallick 1993)
4.2.2.1.	Fluidic oscillator is 6 times[27] the size of the oscillator[26] used by DeSalvo et al. (2011).
4.2.2.2.	Material of the device shall be carbon fiber reinforced polyetherketoneketone (PEKK) due to specific properties that include high strength, high glass transition temperature, T_g, excellent fire, safety, and toxicity (FST) properties, excellent ultraviolet (UV) resistance, and compatibility with composite structures[26].
4.2.2.3.	Device shall have a maximum angle of 30° with respect to the airfoil tangent[28].
4.2.2.4.	Air supply pressure is 30 ± 5 psi[26].
4.2.2.5.	Air supply temperature is 50 ± 30 °F for all flight conditions[26].
4.2.2.6.	Air supply ducts shall have ¾ in.^{2} cross-sectional area, any shape, for each actuator[26].
4.2.2.7.	Plenum and horseshoe section shall be as flat as possible on a radius larger than 1000 in.[26].
4.2.2.8.	Pitch of the device is every ~6 in.[26].
4.2.2.9.	Device shall be removable in the case of maintenance, repair, and replacement[26].

---

[26] Private communication with Boeing

[27] Private communication with Prof. Ari Glezer of Fluid Mechanics Research Laboratory (FMRL) at Georgia Institute of Technology (Georgia Tech)

[28] Private communication with Dr. Michael DeSalvo of Georgia Tech's FMRL

Table C.2. Assumptions

1	Milling operation similar to orbital drilling is feasible
2	64 actuators per civil transport aircraft (Meyer et al. 2014)
3	Isotropic, linear elastic behavior using z direction, SLS manufactured properties
4	K_{IC}/μ/material properties of CF/PEKK equated with respective values of PEEK
5	Standard sealant is a polysulfide sealant
6	Insignificant loads in the x direction and about the y or z axis.
7	Actuator integration design fails before composite spar
8	0.1426 in. wall thickness models

REFERENCES

3D Systems Quickparts. (2013). Rapid Manufacturing: SLS Design Guide – Plastics. [PDF]. Retrieved from http://www.3dsystems.com/sites/www.3dsystems.com/files/legacy/company/dataf iles/SLS_Guide.pdf.

3D Systems. (2016). Selective Laser Sintering Printers. [PDF] Retrieved from http://www.3dsystems.com/sites/www.3dsystems.com/files/sls_brochure_0116_u sen_web.pdf.

Aiken T.N., & Cook A.M. (1973). Results of Full-Scale Wind Tunnel Tests on the H.126 Jet Flap Aircraft. NASA TN D-7252

Alcorta J. (2014). After the TRL (Technology Readiness Level), the MRL (Manufacturing Readiness Level). Retrieved from http://rescoll.fr/blog/trl-technology-readiness-level-mrl-manufacturing-readiness-level/.

Amitay M., Washburn A. E., Anders S. G., & Parekh, D. E. (2004). Active Flow Control on the Stingray Uninhabited Air Vehicle: Transient Behaviour. AIAA Journal, 42(11), 2205-2215. doi:10.2514/1.5697

ATDynamics. (2011). Fuel-Efficient Active Flow Control for Tractor Trailers. [PDF] Retrieved from http://www.arb.ca.gov/research/apr/past/icat08-1.pdf

Bak D. (2003). Rapid prototyping or rapid production? 3D printing processes move industry towards the latter. Assembly Automation, 23(4), 340-345. doi:10.1108/01445150310501190

Barton, J. A., Love, D. M., & Taylor, G. D. (2001). Design determines 70% of cost? A review of implications for design evaluation. Journal of Engineering Design, 12(1), 47-58. doi:10.1080/09544820010031553

BASF Corporation. (2007). Snap-Fit Design Manual. [PDF] Retrieved from http://web.mit.edu/2.75/resources/random/Snap-Fit%20Design%20Manual.pdf.

Bauer M., Lohse J., Haucke F., & Nitsche W. (2014). High-Lift Performance Investigation of a Two-Element Configuration with a Two-Stage Actuator System. AIAA Journal, 52(6), 1307-1313. doi:10.2514/1.j052639

Bauer P. (1981). Method for Mass Production Assembly of Fluidic Devices. U.S. Patent 4,304,749

Becker H., & Gärtner C. (2008). Polymer microfabrication technologies for microfluidic systems. Anal Bioanal Chem, 390, 89-111

Blank S. (2013). It's Time to Play Moneyball: The Investment Readiness Level. Retrieved from http://steveblank.com/2013/11/25/its-time-to-play-moneyball-the-investment-readiness-level/

Boeing. (2016). Boeing to Reduce 747 Production Rate, Recognize Fourth-Quarter Charge. Retrieved from http://boeing.mediaroom.com/2016-01-21-Boeing-to-Reduce-747-Production-Rate-Recognize-Fourth-Quarter-Charge.

Boothroyd G., Dewhurst P., Knight W. (2002). Product Design for Manufacture and Assembly (2nd ed.). Boca Raton, FL: CRC Press Taylor and Francis Group

Branson Ultrasonics Corporation. (2013). Ultrasonic Plastic Joining: Part Design for Ultrasonic Welding. [PDF]. Retrieved from http://www.emersonindustrial.com/en-US/documentcenter/BransonUltrasonics/Plastic%20Joining/Ultrasonics/Technical%20Info/PW-3_Part_Design_for_Ultrasonic_Welding_%28single_pgs%29_hr.pdf.

Brinksmeier E., Fangmann S., & Meyer I. (2008). Orbital drilling kinematics. Prod. Eng. Res. Devel. Production Engineering, 2(3), 277-283. doi:10.1007/s11740-008-0111-7

Budynas R.G., Nisbett J.K., & Shigley J.E. (2011). Shigley's Mechanical Engineering Design (9th ed.). Boston: McGraw-Hill.

Catche S., Piquet R., Lachaud F., Castanie B., & Benaben A. (2014). Analysis of hole wall defects of drilled carbon fiber reinforced polymer laminates. Journal of Composite Materials, 49(10), 1223-1240. doi:10.1177/0021998314532668

Cattafesta L, Sheplak M. (2011). Actuators for active flow control. Annu Rev Fluid Mech, 43, 247–272. doi:10.1146/annurev-fluid-122109-160634

CES EduPack. (2015). [Computer Software].

Chambers J.R. (2005). Innovation in Flight. NASA Langley Research Center, NASA SP-2005-4539.

Cochran D.S., Eversheim W., Kubin G., Sesterhenn M.L. (2000). The Application of Axiomatic Design and Lean Management Principles in the Scope of Production System Segmentation. The International Jour. of Production Research. 38: 6, 1377-1396

Collis S.S., Joslin R.D., Seifert A., Theofilis V. (2004). Issues in active flow control: theory, control, simulation, and experiment. Progress in Aerospace Sciences, 40, 237–289. doi:10.1016/j.paerosci.2004.06.001

Crowther W. J., & Gomes L. T. (2008). An evaluation of the mass and power scaling of synthetic jet actuator flow control technology for civil transport aircraft applications. Proceedings of the Institution of Mechanical Engineers, Part I: Journal of Systems and Control Engineering, 222(5), 357-372. doi:10.1243/09596518jsce519

D. B. Tang, G.J. Zhang, S. Dai. (2008). Integration of Axiomatic Design and Design Structure Matrix for Product Design. Advanced Materials Research, Vols. 44-46, pp. 421-428, Jun. 2008

Davim J., & Reis P. (2003). Study of delamination in drilling carbon fiber reinforced plastics (CFRP) using design experiments. Composite Structures, 59(4), 481-487. doi:10.1016/s0263-8223(02)00257-x.

DeSalvo M. (2015). Airfoil aerodynamic performance enhancement by manipulation of trapped vorticity concentrations using active flow control. (Unpublished doctoral dissertation). Georgia Institute of Technology, Atlanta, GA.

DeSalvo M. E., Whalen E. A., & Glezer A. (2014). Enhancement of High-Lift System Flap Performance using Active Flow Control. 52nd Aerospace Sciences Meeting. doi:10.2514/6.2014-0198

DeSalvo M., Glezer A., & Whalen E. (2011). High-lift Enhancement Using Active Flow Control. 29th AIAA Applied Aerodynamics Conference. doi:10.2514/6.2011-3355

Dotmar. (n.d.). Co-efficient of Friction of Plastic. Retrieved from http://www.dotmar.com.au/co-efficient-of-friction.html.

Eguti, C. C., & Trabasso, L. G. (2014). Design of a robotic orbital driller for assembling aircraft structures. Mechatronics, 24(5), 533-545. doi:10.1016/j.mechatronics.2014.06.007

Few D.D. (1987). A Perspective on 15 Years of Proof-of-Concept Aircraft Development and Flight Research at Arnes-Moffett by the Rotorcraft and Powered-Lift Flight Projects Division, 1970- 1985. NASA RP 1187.

Gad-el Hak M., Pollard A., Bonnet J. (1998). Flow Control: Fundamentals and Practices. Berlin, Germany: Springer-Verlag Berlin Heidelberg

Gensler R., Beguelin P., Plummer, C.J., Kausch H.H., & Munstedt H. (1996). Tensile behaviour and fracture toughness of poly(ether ether ketone)/poly(ether imide) blends. Polymer Bulletin, 37(1), 111-118. doi:10.1007/bf00313826

Gologan C. (2010). A Method for the Comparison of Transport Aircraft with Blown Flaps. (Doctoral dissertation). Retrieved from http://d-nb.info/100822880X/34.

Gregory J.W. and Tomac M.N. (2013). A Review of Fluidic Oscillator Development and Application for Flow Control. 43rd Fluid Dynamics Conference.

Hocheng H., & Tsao C. (2005). The path towards delamination-free drilling of composite materials. Journal of Materials Processing Technology, 167(2-3), 251-264. doi:10.1016/j.jmatprotec.2005.06.039

Horton B.M. and Bowles R.E. (1965). Fluid Oscillator. U.S. Patent No. 3,185,166.

Humphrey E.F., & Tarumoto D.H. (ed.). (1965). Fluidics, Fluid Amplifier Associates, Inc., Boston, Mass.

Hunting. (1963). Hunting H.126 Jet-Flap Research Aircraft. Aircraft Engineering and Aerospace Technology, 35(6), 166 – 167. http://dx.doi.org/10.1108/eb033738

Jabbal M., Liddle S. C. & Crowther W. J. (2010). Active Flow Control Systems Architectures for Civil Transport Aircraft. Journal of Aircraft, 47(6), 1966-1981. doi:10.2514/1.c000237

Jabbal M., & Tomasso V. (2014). Sensitivity Analysis of Active Flow Control Systems: Operating Parameters and Configuration Design. Journal of Aircraft, 51(1), 330-335. doi:10.2514/1.c032110

Joneja A. (2010). Design For Manufacturing/Assembly (DFM, DFA, DFMA) [PDF]. Retrieved from http://www.ielm.ust.hk/dfaculty/ajay/courses/ielm317/lecs/dfm/dfm.pdf

Kadosch, M. (1964). Attachment of a Jet to a Curved Wall. Proceedings of the Fluid Amplification Symposium, IV, 5-20.

Kondor S., Parekh D., Washburn A., & Glezer A. (2005). Investigations of Synthetic Jet Aerodynamic Control Modulation on a Full-Scale UAV. 43rd AIAA Aerospace Sciences Meeting and Exhibit. doi:10.2514/6.2005-1051

Krishnaraj V., Prabukarthi A., Ramanathan A., Elanghovan N., Kumar M. S., Zitoune R., & Davim J. (2012). Optimization of machining parameters at high speed drilling of carbon fiber reinforced plastic (CFRP) laminates. Composites Part B: Engineering, 43(4), 1791-1799. doi:10.1016/j.compositesb.2012.01.007

Kuchan A. (2012). The integration of active flow control devices into composite wing flaps. (Master's thesis). Retrieved from http://hdl.handle.net/1853/44758

Le Pape A., Lienard C., Bailly J. (2013). Active Flow Control for Helicopters. Aerospace Lab Journal, 6.

Liddle S., & Crowther W. (2008). Systems and certification issues for active flow control systems for separation control on civil transport aircraft. 46th AIAA Aerospace Sciences Meeting and Exhibit. doi:10.2514/6.2008-158

Lin J.C., Andino M.Y., Alexander M.G., Whalen E.A., Spoor M.A., Tran J.T., & Wygnanski I.J. (2016). An Overview of Active Flow Control Enhanced Vertical

Tail Technology Development. 54th AIAA Aerospace Sciences Meeting. doi:10.2514/6.2016-0056

Mallick P.K. (1993). Fiber-Reinforced Composites: Materials, Manufacturing, and Design (2nd ed.). New York, NY: Marcel Dekker, Inc.

Mason, W.H. (2012). Powered High Lift Systems Class Presentation [PDF]. Retrieved from http://www.dept.aoe.vt.edu/~mason/Mason_f/HiLiftPresPt2.pdf

Mathiowetz V., Kashman N., Volland G., Weber K., Dowe M., and Rogers S. (1985). Grip and pinch strength: normative data for adults. Arch Phys Med Rehabil, 66, 69-72.

Mazumdar S.K. (2002). Composites Manufacturing: Materials, Product, and Process. Boca Raton, Florida: CRC Press LLC. pp 336-343.

McLean J. D., Crouch J.D., Stoner R.C., Sakurai S., Seidel G.E., Feifel W.M., and Rush H.M. (1999). Study of the Application of Separation Control by Unsteady Excitation to Civil Transport Aircraft. NASA/CR-1999-209338

MD Helicopters. (2014). Technical Description: MD 600N Helicopter. [PDF] Retrieved from http://www.mdhelicopters.com/v2/pdfs/products/MD600N_Tech_Desc.pdf

Melton L.P. (2014). Active Flow Separation Control on a NACA 0015 Wing using Fluidic Actuators, 7th AIAA Flow Control Conference, AIAA Aviation, AIAA 2014-2364. http://dx.doi.org/10.2514/6.2014-2364

Messler R.W. (2006). Integral mechanical attachment a resurgence of the oldest method of joining. Amsterdam: Elsevier/Butterworth-Heinemann.

Meyer M., Machunze W., & Bauer M. (2014). Towards the Industrial Application of Active Flow Control in Civil Aircraft - An Active Highlift Flap. 32nd AIAA Applied Aerodynamics Conference. doi:10.2514/6.2014-2401

Naitove M.H. (2014). Machine-Hour Rates Increased. Retrieved from http://www.ptonline.com/articles/machine-hour-rates-increased

PayScale. (2016). Manufacturing Technician Salary: United States. Retrieved from
http://www.payscale.com/research/US/Job=Manufacturing_Technician/Hourly_R
ate.

Protolabs. (2008). Injection-Molded Part Radiusing and Draft Guidelines. Retrieved from
https://www.protolabs.com/injection-molding/fundamentals-of-molding/draft.

Raghu S. (2001). Feedback-free Fluidic Oscillator and Method. U.S. Patent No.
6,253,782 B1.

Raghu S. (2013). Fluidic oscillators for flow control. Exp Fluids, 54:1455.
doi:10.1007/s00348-012-1455-5

Raman G., & Raghu S. (2004). Cavity Resonance Suppression Using Miniature Fluidic
Oscillators. AIAA Journal, 42(12), 2608-2612. doi:10.2514/1.521

Ruffo M., Tuck C., and Hague R.J.M. (2006a). Cost estimation for rapid manufacturing -
laser sintering production for low to medium volumes. Proceedings of the
Institution of Mechanical Engineers, Part B: Journal of Engineering Manufacture,
220(9), 1417-1427. doi:10.1243/09544054jem517

Ruffo M., Tuck C., and Hague R.J.M. (2006b). An empirical laser sintering time
estimator for Duraform PA. International Journal of Production Research, 44(23),
5131-5146. doi:10.1080/00207540600622522

Sadek A., Meshreki M., & Attia M. (2012). Characterization and optimization of orbital
drilling of woven carbon fiber reinforced epoxy laminates. CIRP Annals -
Manufacturing Technology, 61(1), 123-126. doi:10.1016/j.cirp.2012.03.089

Schultz R.L., Michael R.K., Dagenais P.C., Fripp M.L., & Tucker J.C. (2008). Apparatus
and method for creating pulsating fluid flow, and method of manufacture for the
apparatus. U.S. Patent 7,404,416 B2

Scott J. (2002). Airliner takeoff speeds. Retrived from
http://www.aerospaceweb.org/question/performance/q0088.shtml.

Seifert A., Friedland O., Dolgopyat D., Shig L. (2015). High-Efficiency Active Flow
Controlled Wind Turbines. [PDF]. Retrieved from

http://www.worldwindconf.net/wp-content/uploads/2015/11/Seifert-High-Efficiency-Wind-Turbines-2015-v7.pdf

Singh S., Goel T., Singh R., Kumar S., Singh R.K. (2014). A Comprehensive Study of Modern Flow Control Methods and Their Applications. International Conference of Advance Research and Innovation

Sobelman J. (n.d.). Lockheed F-104 Starfighter. Retrieved from http://www.airplanedriver.net/study/f104.htm

Solies U.P. (1992). Flight measurements of downwash on the Ball-Bartoe Jetwing powered lift aircraft. Journal of Aircraft, 29(5), 927-931. doi:10.2514/3.46264

Spyropoulos C.E. (1964). A Sonic Oscillator. Proceedings of the Fluid Amplification Symposium, III, 27-51.

Stephens E. (2012). NOTAR: More than what it appears to be. Retrieved from http://www.aviationtoday.com/rw/products/rotor-blades/NOTAR-More-than-What-it-Appears-to-Be_77176.html#.VrfnV1kujZs.

Suh N.P. (2001). Axiomatic Design: Advances and Applications. New York: Oxford University Press.

The O-ring Store. n.d. -003 E70 FDA EPDM O-Ring 70D. Retrieved from http://www.theoringstore.com/index.php?main_page=product_info&cPath=367_150_155&products_id=6722.

Tomac M.N., & Gregory J. (2012). Frequency Studies and Scaling Effects of Jet Interaction in a Feedback-Free Fluidic Oscillator. 50th AIAA Aerospace Sciences Meeting including the New Horizons Forum and Aerospace Exposition, Aerospace Sciences Meetings. http://dx.doi.org/10.2514/6.2012-1248

Tomac M.N., & Gregory J.W. (2013). Jet Interactions in a Feedback-Free Fluidic Oscillator in Low Flow Rate Region. 43rd AIAA Fluid Dynamics Conference.

Trimble S. (2015). ANALYSIS: Renton factory evolves to meet 737 production rate. Retrieved from https://www.flightglobal.com/news/articles/analysis-renton-factory-evolves-to-meet-737-product-412908/.

Tsao, C., & Devoe, D. L. (2008). Bonding of thermoplastic polymer microfluidics. Microfluidics and Nanofluidics Microfluid Nanofluid, 6(1), 1-16. doi:10.1007/s10404-008-0361-x

Viets H. (1975). Flip-flop jet nozzle. AIAA Journal, 13, 10, 1375-1379.

Wang L., Luo Z., Xia Z., Liu B, and Deng X. (2012). Review of actuators for high speed active flow control. Science China Technological Sciences, 55, 8, 2225-2240. doi:10.1007/s11431-012-4861-2

Warren, R.W. (1962a). Fluid Oscillator. U.S. Patent No. 3,016,066.

Warren, R.W. (1962b). Wall Effect and Binary Devices. Proceedings of the Fluid Amplification Symposium, 1, 11.

Weathers T.M. (1972). NASA Contributions to Fluidic Systems: A Survey. NASA SP-5112. [PDF] Retrieved from http://ntrs.nasa.gov/archive/nasa/casi.ntrs.nasa.gov/19730002533.pdf.

Wright T. (2003). Giant Amphibian. Retrieved from http://www.airspacemag.com/military-aviation/giant-amphibian-25398933/?all